

# Electromagnetic design and field emission studies for the inner electrode system of the KATRIN main spectrometer

Michael Zacher

Diplomarbeit

Institut für Kernphysik  
Mathematisch-Naturwissenschaftliche Fakultät  
Westfälische Wilhelms-Universität Münster

Januar 2009

revised edition  
June 18, 2009





Referent: Prof. Dr. C. Weinheimer

Korreferent: Prof. Dr. J. Wessels



There is a theory which states that if ever anyone discovers exactly what the universe is for and why it is here, it will instantly disappear and be replaced by something even more bizarre and inexplicable.

There is another which states that this has happened already.

— Douglas Adams, *The restaurant at the end of the universe*



# Contents

<b>1</b>	<b>Introduction</b>	<b>1</b>
<b>2</b>	<b>Neutrinos</b>	<b>3</b>
2.1	The beginning of neutrino physics . . . . .	3
2.2	Evidence for massive neutrinos . . . . .	4
2.3	Absolute neutrino mass from kinematics of beta decay . . . . .	7
<b>3</b>	<b>Discharge mechanisms and Penning traps</b>	<b>11</b>
3.1	Townsend discharge . . . . .	11
3.2	Field emission and vacuum breakdown . . . . .	12
3.3	Penning traps and Penning discharges . . . . .	13
<b>4</b>	<b>MAC-E filter</b>	<b>15</b>
4.1	Principle of a MAC-E filter . . . . .	15
4.2	Adiabatic energy transformation and energy resolution . . . . .	16
4.3	Transmission properties . . . . .	18
4.4	Electric and magnetic field inhomogeneities . . . . .	20
4.5	Background sources . . . . .	21
4.5.1	Electrons emitted from the vessel hull . . . . .	21
4.5.2	Penning Traps . . . . .	22
4.5.3	Bumps in the longitudinal energy along the spectrometer . . . . .	22
4.5.4	Field emission . . . . .	22
4.6	Background suppression with an inner wire electrode . . . . .	23
<b>5</b>	<b>The KATRIN experiment</b>	<b>25</b>
5.1	KATRIN components . . . . .	25
5.1.1	Windowless gaseous tritium source (WGTS) . . . . .	26
5.1.2	Transport section . . . . .	26
5.1.3	Pre-spectrometer . . . . .	26
5.1.4	Main spectrometer . . . . .	27
5.1.5	Detector . . . . .	27
5.2	The inner wire electrode of the main spectrometer . . . . .	27
5.2.1	Modular setup of the electrode system . . . . .	28
5.2.2	Wire electrode modules . . . . .	29
5.2.3	Cylinder module caps . . . . .	31
<b>6</b>	<b>Design of the inner electrode system of the main spectrometer</b>	<b>35</b>
6.1	Simulation tools . . . . .	35
6.1.1	Magnetic field calculations . . . . .	35

6.1.2	Electric field calculations . . . . .	37
6.1.3	Calculations including magnetic and electric components . . . . .	40
6.1.4	Geometry creation . . . . .	40
6.1.5	Overview . . . . .	41
6.2	Optimisation of the electrode design . . . . .	42
6.2.1	Shielding electrode design and mechanical realisation . . . . .	44
6.2.2	Ground electrode . . . . .	45
6.2.3	Relative placement of ring 02 and the shielding electrode . . . . .	49
6.2.4	Absolute placement of the shielding electrode . . . . .	53
6.2.5	Penning trap at module ring 02 . . . . .	57
6.2.6	Module ring 02 and 03 comb potential . . . . .	62
6.3	Conclusion and proposed setup . . . . .	65
<b>7</b>	<b>Field emission at the KATRIN main spectrometer wire electrode</b>	<b>69</b>
7.1	Motivation . . . . .	69
7.2	Setup . . . . .	71
7.3	Energy calibration . . . . .	77
7.3.1	Calculation of the pulse generator peak energy . . . . .	78
7.3.2	Measurement of the offset of the main amplifier . . . . .	78
7.3.3	Calibration with 24kV electrons . . . . .	79
7.4	Measurements . . . . .	80
7.4.1	First measurement period (wire 1) . . . . .	80
7.4.2	Second measurement period (wire 2) . . . . .	81
7.4.3	Third measurement period (wire routed past tooth) . . . . .	84
7.5	Analysis and results . . . . .	85
7.5.1	Discussion of the background properties . . . . .	85
7.5.2	Derivation of upper limits . . . . .	87
7.5.3	Implications for the KATRIN main spectrometer . . . . .	89
<b>8</b>	<b>Summary and outlook</b>	<b>91</b>
<b>A</b>	<b>Technical drawings and device type numbers</b>	<b>93</b>
<b>B</b>	<b>Proposed geometry file</b>	<b>97</b>

# 1 Introduction

Neutrinos are one of the most interesting matters of modern particle physics. In the last decades significant progress has been made on the experimental as well as on the theoretical side in this area of research. The discovery of neutrino oscillation has proven that neutrinos are not massless particles. The absolute neutrino mass scale is important for particle- and astrophysics as well as for cosmology.

The Karlsruhe TRITium Neutrino mass experiment (KATRIN) aims to determine the neutrino mass by a precision measurement of the tritium  $\beta$  spectrum, improving the sensitivity by an order of magnitude with respect to its predecessor experiments. To achieve the desired resolution, the biggest MAC-E filter built up to now is used as main spectrometer to analyse the  $\beta$  electrons. The main spectrometer features an inner electrode system for background suppression as well as to allow a better adjustment of the electromagnetic properties of the spectrometer. This diploma thesis will discuss several topics related to the inner electrode system.

One topic is the electromagnetic design of the inner electrode system of the main spectrometer. The demands for a low background rate and good transmission properties call for a precise and careful design of the inner electrode system. In the course of this thesis, simulations on the design of the electrode system for the steep cone and flange regions of the main spectrometer have been conducted

The major part of the the inner wire electrode consists of two layers of wires supported by a frame structure. For background suppression, the inner layer of these wires is put on a more negative electric potential than the frame structure. At the mounting position of the wires high electric field strengths lead to the possibility of field emission. As field emission at this critical position would give rise to an increased background rate, an experiment was conducted to investigate under which conditions field emission occurs at this position.

This thesis will be structured as follows:

- In chapter 2 a short introduction to neutrino physics will be given as well as a brief overview of approaches to gain information about the neutrino mass. The emphasis will be on the possibility to obtain information on the absolute neutrino mass from the kinematics of  $\beta$  decay.
- Chapter 3 will explain discharge mechanisms (e.g. field emission) and Penning traps. These mechanisms can account for background effects in the KATRIN main spectrometer.
- The concept of the MAC-E filter will be explained in chapter 4, as it is an essential part of the KATRIN experiment and its predecessors. The energy resolution

and transmission function will be derived and possible background sources and measures to suppress them are discussed.

- Chapter 5 describes the KATRIN experiment itself. As the main parts of this thesis cover topics related to the inner electrode system of the main spectrometer, it will be discussed in more detail here.
- In chapter 6 the electromagnetic design of the inner electrode system of the main spectrometer is discussed. The electrode system of the steep cone and flange regions has a big impact on the transmission and background properties of the spectrometer. Hence, a careful design of these parts is essential to comply with the requirements of the experiment while still being mechanically feasible.
- At the wire mounting positions of the inner wire electrode, high electric field strengths occur. The presence of field emission at these positions would lead to an increased background rate. Hence, an experimental was conducted to investigate under which conditions field emission can occur at these critical points.

## 2 Neutrinos

Since the prediction of their existence by W. Pauli in 1930, neutrinos have found their way into many fields of research. Modern astrophysics and particle physics strive to reveal more details about this elusive particle, which is present in huge numbers everywhere in the universe but nevertheless is neither easy to observe nor is it understood completely. One of the open questions is the neutrino mass. Since the answer to this question is relevant for particle- and astrophysics as well as for cosmology, huge efforts were and are still made to solve this problem.

This chapter will start with a short glimpse on the history of neutrino physics. The second section introduces neutrino oscillations as evidence for massive neutrinos. In the last section the possibility to measure the absolute neutrino mass by precision measurements of the  $\beta$  decay spectrum will be discussed.

### 2.1 The beginning of neutrino physics

It was a long and interesting way from the theoretical prediction of the neutrino to the current search for the absolute neutrino mass. The history of neutrino physics begins many decades before the actual experimental evidence of their existence.

In the late 19th century Henry Becquerel discovered the phenomenon of radioactivity. This field of research was brought forward by many scientist like Marie Curie or Ernest Rutherford, leading to a deeper understanding of the nature of matter.

In 1914 James Chadwick was the first to measure the energy spectrum of electrons resulting from a  $\beta$ -decay. Up to that time only the line-spectra of  $\alpha$ - and  $\gamma$ -decays were known. In contrast to that, a continuous spectrum was found for the  $\beta$ -decay [Cha14]. Assuming a two-body decay, this leads to a violation of the conservation laws of energy and angular momentum.

A solution to this problem was suggested 1930 by W. Pauli in his famous open letter, which he himself described as a “desperate way out” [Pau30]. He postulated a neutral particle inside the nucleus with about the same mass as an electron and the spin  $1/2$ . With this assumption the  $\beta$  decay is a three-body process, resulting in the observed continuous spectrum. In his letter he referred to this particle as “neutron”. After the discovery of the neutral nucleon by Chadwick two years later it became obvious that this could not be the particle Pauli had postulated, as the mass of this neutron was too high. In 1934 E. Fermi presented his theory of the  $\beta$ -decay [Fer34] and introduced the name neutrino for the particle described by Pauli.

An experimental search for neutrinos who only interact weakly was only possible with a strong neutrino source because of the very small cross sections involved. Such strong sources can be found in nuclear reactors<sup>1</sup>.

---

<sup>1</sup>Operated by a team of scientists headed by E. Fermi, the first artificial nuclear reactor called *Chicago*

In 1956 Frederick Reines and Clyde L. Cowan found experimental evidence [Rei59] for the neutrino using the high neutrino flux produced by the Savannah River Reactor (USA). The complex *neutrino experiment* consisted of water with cadmium chloride added, surrounded by scintillation detectors. An incident neutrino can interact with a proton from the water, creating a neutron and a positron by the inverse  $\beta$ -decay

$$p + \bar{\nu}_e \rightarrow n + e^+. \quad (2.1)$$

Cadmium is a highly effective neutron absorber. The resulting daughter nucleus decays to its ground state by emitting a  $\gamma$  photon after a characteristic delay time of a few  $\mu\text{s}$ . The experiment made use of the coincident measurement of a 511 keV photon resulting from the positron annihilation and the detection of the delayed  $\gamma$ -photon emitted by the cadmium. With this method evidence for the inverse  $\beta$ -decay and thus the existence of the neutrino could be found.

Several experiments have since then confirmed and further refined the result from Cowan and Reines. Perhaps most interesting and surprising was the evidence that neutrinos are not massless particles, as will be explained in the next section.

## 2.2 Evidence for massive neutrinos

In the 1960s, the *standard model of particle physics* was established with neutrinos as a well integrated component. Up to now the standard model has proven its strength and is a very successful theory.

Neutrinos are described as massless particles by the standard model. The first inconsistency of this description was brought up around 1970 and is known as the *solar neutrino problem*.

The *Homestake experiment* was a very laborious experiment built to measure the neutrino flux from the sun. In the sun neutrinos are produced by the net fusion reaction [Zub04]

$$2e^- + 4p \rightarrow {}^4_2\text{He} + 2\nu_e + 26.73 \text{ MeV}. \quad (2.2)$$

The excess energy of 26.73 MeV is divided into the kinetic energy of the neutrino and the thermal energy carried away by radiation. After a first unsuccessful measurement period with no detected neutrinos, they could indeed detect neutrinos and calculate the neutrino flux from the sun in the early 1970s. But the results Raymond Davis, Jr. and John N. Bahcall obtained did not agree with the calculated neutrino flux of the solar models, which predicted a neutrino flux roughly three times as big as the measured flux. These results were confirmed in the 1990s (*GALLEX*, *SAGE*). In 2002, Raymond Davis, Jr. received the Nobel prize for his work [Nobel02].

A possible way to explain this lack of neutrinos is *neutrino oscillation* which assumes that neutrinos are not massless.

The standard model describes three neutrino *flavours*  $\nu_e$ ,  $\nu_\mu$  and  $\nu_\tau$ . According to the neutrino oscillation theory, the neutrino mass eigenstates  $\nu_i$  with  $i = 1, 2, 3$  are not identical to these flavour eigenstates  $\nu_\alpha$  with  $\alpha = e, \mu, \tau$  but are connected to them by

---

*Pile-1* achieved the critical point in December 1946.

a  $3 \times 3$  unitary matrix  $U$  called *Pontecorvo-Maki-Nakagawa-Sakata (PMNS) matrix*<sup>2</sup> :

$$|\nu_\alpha\rangle = \sum_i U_{\alpha i} |\nu_i\rangle \quad (2.3)$$

$$|\nu_i\rangle = \sum_\alpha U_{\alpha i}^* |\nu_\alpha\rangle, \quad (2.4)$$

It can be written using the mixing angles  $\Theta_{ij}$  [Les06]:

$$U = \begin{pmatrix} c_{12}c_{13} & c_{12}c_{13} & s_{13}e^{-i\delta} \\ -s_{12}c_{23} - c_{12}s_{23}s_{13}e^{i\delta} & c_{12}c_{23} - s_{12}s_{23}s_{13}e^{i\delta} & s_{23}c_{13} \\ s_{12}s_{23} - c_{12}c_{23}s_{13}e^{i\delta} & -c_{12}s_{23} - s_{12}c_{23}s_{13}e^{i\delta} & c_{23}c_{13} \end{pmatrix} \quad (2.5)$$

with the abbreviation  $s_{ij} = \sin \Theta_{ij}$   $c_{ij} = \cos \Theta_{ij}$ . The possibility that neutrino oscillations violate CP symmetry is taken into account by the factor  $e^{i\delta}$ .

Using the Schrödinger equation and  $\hbar = c = 1$  one obtains the time development of a mass eigenstate

$$|\nu_i(t)\rangle = e^{-iE_i t} |\nu_i\rangle, \quad (2.6)$$

with

$$E_i = \sqrt{p_i^2 + m_i^2} \approx p + \frac{m_i^2}{2p} \approx E + \frac{m_i^2}{2E} \quad \text{for } p \gg m_i. \quad (2.7)$$

Here  $E$  denotes the neutrino energy (compare [Sch97]).

After a time  $t$  (corresponding to a distance  $L \approx ct$ , as neutrinos are highly relativistic particles) a former pure flavour eigenstate  $|\nu_\alpha\rangle$  can be written as

$$|\nu(t)\rangle = \sum_i U_{\alpha i} e^{-iE_i t} |\nu_i\rangle = \sum_{i,\beta} U_{\alpha,i} U_{\beta,i}^* e^{-iE_i t} |\nu_\beta\rangle. \quad (2.8)$$

Thus, after creating a weak eigenstate  $|\nu_\alpha\rangle$ , the mass components of this eigenstate propagate with different phase velocities. This leads to an oscillating probability for observing a neutrino with a flavour  $\beta$  along its path.

To illustrate the effect of neutrino oscillation, a simplified situation with only 2 neutrino flavours  $\alpha$  and  $\beta$  will be assumed now. In this model, the oscillation matrix is reduced to one angle  $\theta$  and one mass difference  $\Delta m^2 = |m_1^2 - m_2^2|$  exists. The simplified transition probability then reads

$$P(\nu_\alpha \rightarrow \nu_\beta) = \langle \nu_\beta | \nu(t) \rangle = \sin^2(2\theta) \cdot \left( \frac{\Delta m^2 L}{4E} \right). \quad (2.9)$$

Analogous, for the three flavour case the transition probability for such a process is dependent on the squared mass differences  $\Delta m_{ij}^2$ , the angles  $\Theta_{ij}$  and on the ratio  $L/E$ . This is illustrated in figure 2.1 for a  $\bar{\nu}_e \rightarrow \bar{\nu}_e$  process.

First hints for such oscillation processes have been measured using atmospheric neutrinos in the *Super-Kamiokande* experiment [Fuk98] and have been confirmed for reactor and accelerator neutrinos (e.g. *K2K* [Ahn06], *KAMland* [Kam05]) as well as for solar neutrinos (e.g. *SNO* [Aha05]).

---

<sup>2</sup>The PMNS matrix can be viewed as the analogon to the *CKM-matrix* for the quarks.

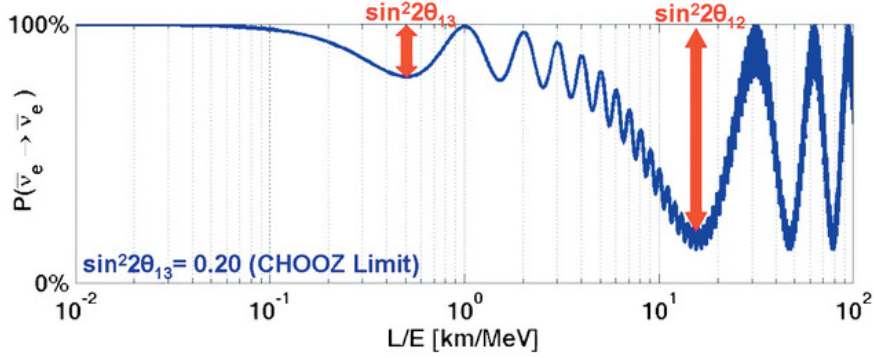


**Figure 2.1:** The transition probability for a  $\bar{\nu}_e \rightarrow \bar{\nu}_e$  process depending on  $L/E$ . While for small values of  $L/E$  the transition into another flavour is unlikely ( $P \approx 1$ ), the transition probability shows strong oscillations for higher values, hence allowing the transition into another flavour with a high probability in some cases. Figure taken from [KAT06].

From measurements of the oscillation rates information on the angles  $\Theta_{ij}$  and the squared mass differences  $\Delta m_{ij}^2$  can be obtained, but no information on the absolute scale or the hierarchy of the neutrino mass eigenstates.

The neutrino oscillation proves that neutrinos are in fact massive particles and therefore an extension of the standard model is needed. Up to now there, are several ways to include the neutrino mass in the standard model (e.g. the *seesaw-mechanism* or *Supersymmetry*).

Oscillation experiments cannot give information on the absolute neutrino mass scale. However, this absolute mass is an important parameter for astrophysics as well as for particle physics. This calls for experimental efforts to measure the absolute neutrino mass. There are several methods which allow to access the absolute mass scale, e.g.:

- Cosmological models and observations like *WMAP* give predictions on the neutrino mass, but these are model dependent.
- If neutrinos are Majorana particles, a neutrinoless double  $\beta$  decay is possible. The PMNS matrix given by eq. 2.5 then has to be expanded by multiplying with an additional diagonal matrix introducing two additional phase parameters  $\phi_2$  and  $\phi_3$  which are not observable in neutrino oscillations. The decay rate proportional of a neutrinoless double  $\beta$  decay is proportional to the so-called effective neutrino mass  $m_{ee}(\nu)$  which is then given by [Les06]

$$m_{ee}(\nu) = \left| \sum_i U_{ei}^2 m_i \right| \quad (2.10)$$

$$= \left| (c_{12}^2 c_{13}^2 m_1 + s_{12}^2 c_{13}^2 m_2 e^{i\phi_2} + s_{13}^2 m_3 e^{i\phi_3}) \right|. \quad (2.11)$$

Due to the additional phase factors destructive interference is possible, thus  $m_{ee}$  could suggest a too low neutrino mass. In addition, the uncertainty of the for the decay important nuclear matrix element is still about a factor of order two, further complicating this approach.

- The kinematics of  $\beta$  decay can provide information on the absolute neutrino mass. This method is model independent and has up to now given the lowest direct limit on the electron neutrino mass.

The next chapter will give more details on the determination of the absolute neutrino mass from the kinematics of  $\beta$  decay.

## 2.3 Absolute neutrino mass from kinematics of beta decay

The determination of the neutrino mass from the kinematics of  $\beta$  decay is based on a precision analysis of the  $\beta$  spectrum resulting from the weak interaction, e.g. the  $\beta^-$  - decay:

$$X(Z,A) \rightarrow Y(Z+1,A) + e^- + \bar{\nu}_e \quad (2.12)$$

$$n \rightarrow p + e^- + \bar{\nu}_e \quad (2.13)$$

The mass of the electron and the neutrino is small compared to the mass of the daughter nucleus, hence the recoil energy of the nucleus can be neglected. Using Fermi's Golden Rule one obtains the form of the energy spectrum [Alt03]

$$\frac{d\dot{N}}{dE} = R(E) \sqrt{(E_0 - E)^2 - m_{\bar{\nu}_e}^2 c^4} \Theta(E_0 - E - m_{\bar{\nu}_e} c^2). \quad (2.14)$$

with

$$R(E) = \frac{G_F^2}{2\pi^3 \hbar^7} \cos^2 \theta_C |M|^2 F(Z+1, E) p (E + m_e c^2) (E_0 - E). \quad (2.15)$$

including the following terms:

$G_F$	the Fermi coupling constant
$\theta_C$	the Cabibbo angle
$M(E)$	the nuclear matrix element for the transition
$F(Z, E)$	the Fermi function that takes into account the Coulomb interaction between the emitted electron and the daughter nucleus
$p$	the electron momentum
$E$	the kinetic energy of the electron
$E_0$	the endpoint energy of the $\beta$ -spectrum
$m_e c^2$	the rest energy of the electron
$m_{\bar{\nu}_e} c^2$	the rest energy of the electron anti-neutrino

Figure 2.2 shows the  $\beta$  spectrum for tritium with the assumption of different neutrino masses. The highest sensitivity to the neutrino mass is achieved in the endpoint region of the spectrum, but even here the impact is small. To emphasise the endpoint region relative to the lower energy part of the spectrum, a  $\beta$  emitter with a low endpoint energy has to be chosen. Such elements are e.g.  $^{187}\text{Rh}$  with an endpoint energy of about 2.47 keV or tritium with about 18.6 keV.

Although rhenium has a lower endpoint energy, there are facts that support tritium as a  $\beta$  source for experiments also:

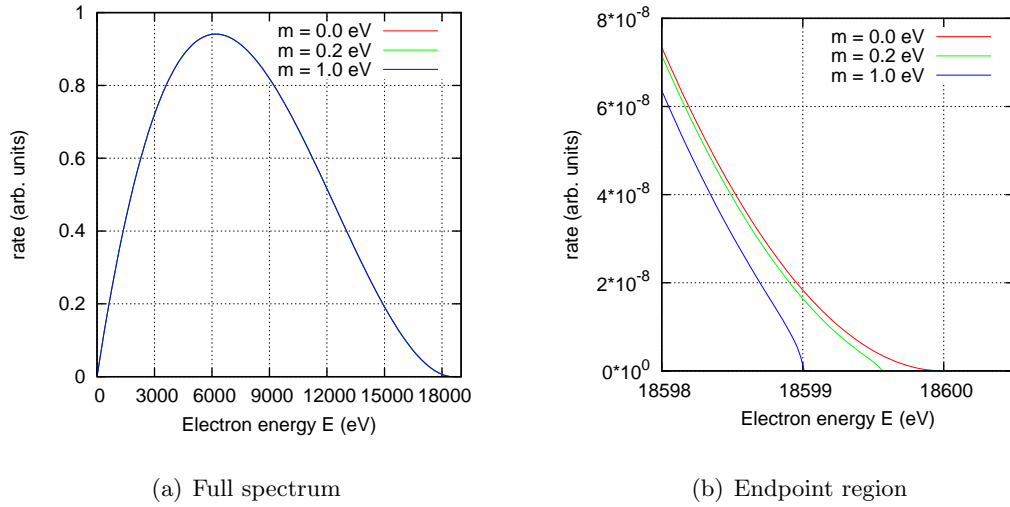


**Figure 2.2:** A tritium  $\beta$  spectrum for different neutrino masses  $m$ . The rate is given in arbitrary units. Tritium has an endpoint energy  $E_0$  of about 18.6 keV. The impact of the neutrino mass is best visible in the region of the last few eV. The influence of the Fermi function  $F(Z, E)$  has been neglected.

- The tritium  $\beta$  decay has a rather short half-life of 12.3 years. This makes it possible to construct a strong source with a low column density. In contrast, the rhenium decay has a much longer half-life of  $4.3 \cdot 10^{10}$  years.
- While the tritium decay is super-allowed, the  $\beta$  decay of  $^{187}\text{Rh}$  is uniquely forbidden. Only for super-allowed decays the nuclear matrix element  $M$  is not dependent on the energy of the  $\beta$  electron.
- The  $T_2$  molecule has a simple electronic structure. Thus, the atomic corrections for tritium and its daughter nucleus  $^3\text{He}^+$  can be calculated quantitatively with good accuracy.
- As the nuclear charge  $Z$  is low, the inelastic scattering of out-going  $\beta$ -electrons within the source is small.

Because of their low endpoint energies, both tritium and rhenium are used in experiments.

Rhenium is used in cryo-bolometer measurements, where the rhenium is source and detector at the same time. Currently these experiments yield an upper limit of  $m_{\bar{\nu}_e} < 15 \text{ eV}/c^2$  at 90% C.L. (Milano neutrino mass experiment MIBETA, [Sis04]). Its successor experiment MARE-1 aims to improve this limit to a few eV in a first phase. As the bolometric approach offers good scaling possibilities, the second phase MARE-2 is expected to reach the sub-eV scale [MAR06].

Tritium is used differently. From a solid or gaseous tritium source the  $\beta$  electrons are guided magnetically into a high resolution spectrometer. The currently best limits have been set by the Mainz experiment with  $m_{\bar{\nu}_e} < 2.3 \text{ eV}/c^2$  [KRA05] and from the Troitsk

---

experiment<sup>3</sup> with a stated upper limit of  $m_{\bar{\nu}_e} < 2.05 \text{ eV}/c^2$  [Lob03], both with 95% C.L..

The KATRIN experiment is also based on the precision analysis of the tritium spectrum and aims to improve the sensitivity on the neutrino mass by one order of magnitude, thus reaching the sub-eV scale. In the case that no evidence for a non-zero neutrino mass is found, KATRIN will set a new upper limit of  $m(\bar{\nu}_e) < 0.2 \text{ eV}/c^2$  with 90% confidence level [KAT04]. The experiment is currently under construction at the Forschungszentrum Karlsruhe in Germany. First measurements are projected to start in 2010.

---

<sup>3</sup>At the Troitsk experiment the integrated spectrum shows a small step in the endpoint region. This effect has been taken into account by introducing a phenomenological step function in the analysis. Up to now the origin of this anomaly it is not completely clear, though an apparatus effect is assumed.



## 3 Discharge mechanisms and Penning traps

This chapter will cover discharge mechanisms which are important for the KATRIN experiment. They contribute to the total background in the main spectrometer and hence have to be understood in order to avoid or suppress these background sources. Strongly connected to this topic is the Penning trap, a particle trap which can be hosted in regions with high magnetic fields and certain conditions of the electric field.

The Townsend discharge mechanism will be covered in the first section. It takes place only at bad vacuum conditions and is therefore not relevant for ultra high vacuum setups like the KATRIN main spectrometer. Nevertheless it will be covered here because the avalanche mechanism is fundamental for the other types of discharge mechanisms. In section 3.2 field emission and the so called vacuum breakdown process will be discussed. These effects are important in regions with high electric field strength, as e.g. given at the geometry studied in chapter 7. The third discharge mechanism is the Penning discharge which will be discussed in section 3.3. This discharge effect is strongly connected to the Penning trap, a particle trap created by certain electric and magnetic field configurations. These traps will play a major role for the electromagnetic design of the inner electrode system for the KATRIN main spectrometer as discussed in chapter 6.

### 3.1 Townsend discharge

For a setup with relatively poor vacuum conditions and a strong electric field exceeding a critical value, a small initial number of electrons  $N^{(0)}$  get accelerated, causing an avalanche mechanism possibly establishing a constant current. This mechanism is named after J. S. Townsend who described this process (see e.g. [Tow10]).

For a simplified description, the case of a parallel pair of plates shall be described here. An initial number  $N^{(0)}$  of electrons is emitted from the cathode plate (e.g. by radiation or radioactivity). These electrons are accelerated by the applied electric field. The mean free path length  $\lambda$  between collisions with gas atoms is depending on the pressure of the gas. If the energy an electron gains by the acceleration along the mean free path length is high enough it can ionise atoms of the gas, thus creating additional charge carriers which also can be accelerated.

The resulting number of electrons  $N_d^{(0)}$  at a distance  $d$  from the cathode surface is given by

$$N_d^{(0)} = N^{(0)} e^{\alpha d} \quad (3.1)$$

where  $\alpha$  is the so called first Townsend coefficient. It gives the average number of electron-ion pairs created by one initial electron. The form of this coefficient is depending on the energy  $E$  an electron gains from the electric field  $\varepsilon$  over the mean free path

length relative to the ionisation Energy  $E_{\text{ion}}$ :

$$\alpha = \begin{cases} c_1 \cdot p e^{-\frac{c_2 p}{\varepsilon}} & \text{for } E < E_{\text{ion}} \\ \frac{1}{\lambda} & \text{for } E \geq E_{\text{ion}}, \end{cases} \quad (3.2)$$

For  $E \geq E_{\text{ion}}$ , every collision is an ionizing one. In this case  $\alpha$  is only dependant on the mean free path length  $\lambda = \frac{1}{n\sigma}$ , with  $n$  denoting the unit volume density of particles with a cross-section  $\sigma$ . In an ideal gas  $n$  is proportional to the pressure  $p$ , thus  $\alpha \propto p$ . If  $E < E_{\text{ion}}$ , elastic collisions can take place. Then  $\alpha$  depends on the electric field  $\varepsilon$ , the pressure  $p$  and two parameters  $c_1$  and  $c_2$  which depend on the gas type and the shape of the electric field.

The positive ions created in the collisions are accelerated towards the cathode. Assuming they have to pass a distance  $d$  to the cathode surface again, the number of ions reaching the electrode equals  $N^{(0)}(e^{\alpha d} - 1)$ . The number of electrons  $N^{(1)}$  liberated in the collisions by these ions is given by

$$N^{(1)} = \gamma N^{(0)}(e^{\alpha d} - 1), \quad (3.3)$$

where the second Townsend coefficient  $\gamma$  denotes the number of electrons liberated per ion impact on the cathode surface. These secondary electrons are now accelerated again, possibly creating more ions and so on. This discharge is self-sustained if the number of secondary electrons exceeds the number of initial electrons:

$$N^{(1)} \geq N^{(0)} \quad \Rightarrow \quad \gamma(e^{\alpha d} - 1) \geq 1. \quad (3.4)$$

In the KATRIN main spectrometer a pressure of  $p < 10^{-11}$  mbar will be achieved. The first Townsend coefficient  $\alpha$  is small and therefore  $\gamma(e^{\alpha d} - 1) \ll 1$ . Hence, self-sustained discharges will not be possible and the Townsend discharge will not occur in this setup.

## 3.2 Field emission and vacuum breakdown

High electric field strength can cause electron emission by the tunnel effect. This quantum mechanical effect allows electrons to overcome the potential barrier of the metal surface.

The current density  $J$  in field emission processes can be described using an adapted form of the Fowler-Nordheim formula [Fow28]

$$J(E_{\text{eff}}) = \zeta \cdot \frac{E_{\text{eff}}^2}{\phi} \cdot \exp\left(-\frac{\xi \phi^{3/2}}{E_{\text{eff}}}\right). \quad (3.5)$$

Here,  $\phi$  is the work function of the metal,  $\zeta$  and  $\xi$  are constants.  $E_{\text{eff}}$  denotes the effective field strength at the electrode surface. This effective field strength  $E_{\text{eff}} = sE_{\text{sm}}$  takes into account deviations from the field strength  $E_{\text{sm}}$  on a perfectly smooth surface induced by microtips and other irregularities on the electrode surface described by the shaping factor  $s$ .

High field emission currents can cause a vacuum breakdown, the loss of the electric isolation provided by the vacuum.

Assuming typical metal work functions, for a perfectly smooth metal surface ( $s = 1$ ) field strength typically up to about 1 GV/m should be possible without a vacuum breakdown due to field emission current [Fow28]. Surface irregularities with  $s \gg 1$  can lead to field emission at voltages which are significant smaller. This especially holds true for wire electrodes with small diameters as they are used in the KATRIN spectrometers. Here the field strength is already higher due to the high curvature of the surface.

Therefore, a careful preparation of the electrode surfaces, e.g. by electropolishing, is advisable<sup>1</sup>. An experimental study of a possible field emission at the KATRIN wire electrode is described in chapter 7.

### 3.3 Penning traps and Penning discharges

The trapping and discharge mechanisms will be explained for electrons in this section, as they are of most interest for the KATRIN spectrometers. To transfer the considerations to positively charged particles the terms anode and cathode have to be exchanged.

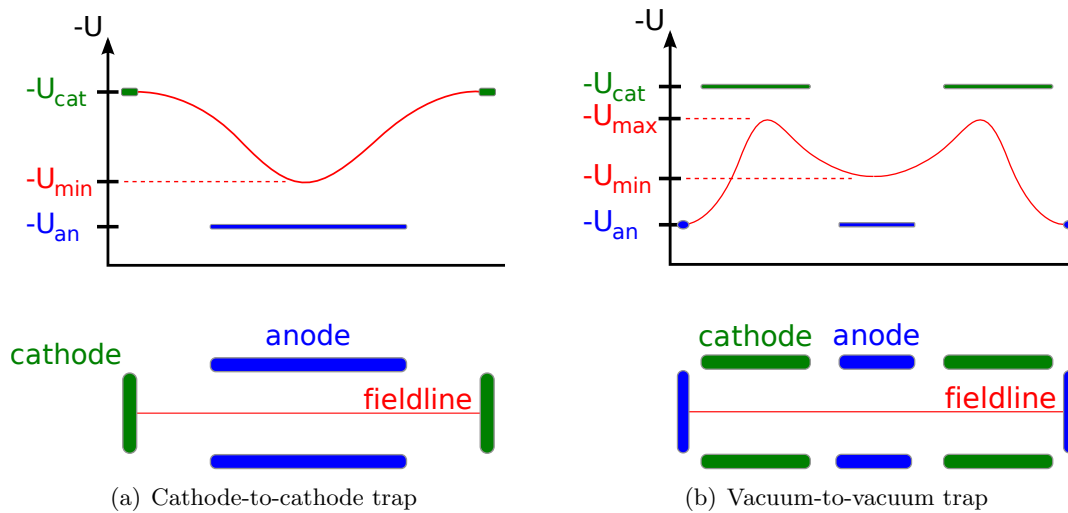


**Figure 3.1:** Schematic view of Penning traps. At the bottom the electrode geometries and a magnetic field line (red) are shown. At the top the electric potential along this field line is plotted. It is convenient to plot  $-U$ , as then traps for electrons show up as valley in the potential.

Penning traps can develop in regions with high electric and magnetic fields. The electrons are guided along the magnetic field lines in a cyclotron motion. A trap can develop if the electric potential along such a magnetic field line shows a potential valley. Particles are trapped if they enter this potential valley and then loose kinetic energy (e.g. by collisions) so they cannot escape the trap any more.

Two simple geometries illustrating possible types of Penning traps are shown in figure 3.1:

<sup>1</sup>The solid electrode surfaces used in the KATRIN main spectrometer are electropolished. The wires of the wire electrode are not electropolished but have been chosen with regard to their surface quality among other parameters (see [Geb07] for details).

- **Cathode-to-cathode traps:** This trap type is shown in 3.1(a). The electric potential along the magnetic field line increases when passing the more positive anode potential. The depth of the resulting trap is  $\Delta U_{\text{trap}} = |U_{\text{cat}} - U_{\text{min}}|$ . This kind of trap can be fed directly with particles emitted from the cathode surface. They are stored in the trap when they lose enough kinetic energy, e.g. by collisions.
- **Vacuum-to-vacuum trap:** An example of this trap type is given in figure 3.1(b). The borders of the potential well are not located at an electrode but in the vacuum. The depth is given by  $\Delta U_{\text{trap}} = |U_{\text{max}} - U_{\text{min}}|$ . Particles only can be trapped if they have enough energy to cross the potential hills resulting from the cathode potential and then lose as much energy (e.g. by collisions) that they cannot leave the potential valley again.

Combinations of these trap types like a cathode-to-vacuum trap are possible, especially in geometries with multiple electrodes and different electrode potentials. The trap depth is then given by the more shallow side of the trap.

The electrons are forced on cyclotron tracks around the magnetic field lines, so the pathlength of these electrons is increased compared to the pathlength without magnetic fields. Therefore, the probability of collisions with the residual gas is higher<sup>2</sup>, causing the creation of secondary particles by ionisation. The increase in pathlength is not proportional to the magnetic field.

The created electrons are confined inside the trap while the positive charged ions are accelerated to the cathode where they can create additional electrons by secondary emission. These can reach the trap region and can also be stored there. This avalanche mechanism is analogue to the Townsend discharge mechanism. If the number of secondary particles exceeds the number of primary trapped particles the discharge is self-sustained, possibly leading to potential and vacuum breakdowns.

As only the electrons are confined in the trap, a negatively charged plasma develops in the trapping region. This can give rise to space charge effects which can also lead to discharges.

If the trap depth is smaller than the ionisation energy, the avalanche mechanism based on this ionisation cannot work. This effectively switches off the trap. As in an ultra high vacuum setup the most prominent residual gas molecule is  $H_2$  with an ionisation energy of  $E_{\text{ion}} = 15.4 \text{ eV}$ , Penning traps in such environments (like the KATRIN main spectrometer) should have a trap depth lower than this energy.

---

<sup>2</sup>This can be compared to the effect of a pressure increase in the Townsend discharge mechanism, as both effects increase the collision probability.

## 4 MAC-E filter

In this chapter a spectrometer based on **M**agnetic **A**diabatic **C**ollimation with **E**lectrostatic filtering (MAC-E filter) will be discussed with special regard to the KATRIN experiment.

A MAC-E filter is a well suited instrument to analyse the tritium  $\beta$  spectrum in order to gain information about the neutrino mass. As described in section 2.3, the neutrino mass has the biggest impact on the spectrum in the endpoint region. In this energy region, the countrate is very small: Approximately only  $10^{-13}$  of all decays result in electrons with an energy  $E$  between  $E_0 - 1 \text{ eV} \leq E \leq E_0$ . Hence, a source with a high luminosity together with a spectrometer with a large angular acceptance and high resolution is needed. As will be discussed below, the MAC-E filter fulfils these requirements. MAC-E type spectrometers were employed successfully in the Mainz and Troisk neutrino mass experiments and will also be used in the KATRIN experiment. In the first chapter the basic principle of a MAC-E filter will be explained, followed by two sections deriving the energy resolution and transmission properties for this kind of spectrometer. Section 4.4 will describe the consequences of inhomogeneities of the electric potential and the magnetic field along the analysing plane. Background sources and measures to suppress and avoid them will be discussed in the last two sections 4.5 and 4.6.

### 4.1 Principle of a MAC-E filter

A schematic view of a MAC-E filter is shown in figure 4.1. The spectrometer consists of two major components:

- A magnetic guiding field is created by superconducting solenoids at the entrance and exit region of the spectrometer. The magnetic field strength has its maximum value  $B_{\text{max}}$  there and drops to a minimum field strength  $B_{\text{ana}}$  at the analysing plane in the spectrometer centre.
- An electric retarding potential  $U_0$  is applied to the spectrometer. It has its maximum in the analysing plane.

Electrons are guided through the spectrometer in cyclotron motions along the magnetic field lines. This cyclotron motion is adiabatic, this means the magnetic flux enclosed by the cyclotron motion is conserved. As a result, the transversal energy of an electron is transformed into longitudinal energy along its way to the analysing plane. The electric potential acts as electrostatic filter. As the magnetic field lines are perpendicular to the analysing plane, only electrons with enough longitudinal energy can pass the retarding potential  $U_0$ . Thus, a MAC-E filter acts as an integrating high pass filter. To measure a spectrum the selected energy range is scanned with the retarding potential.

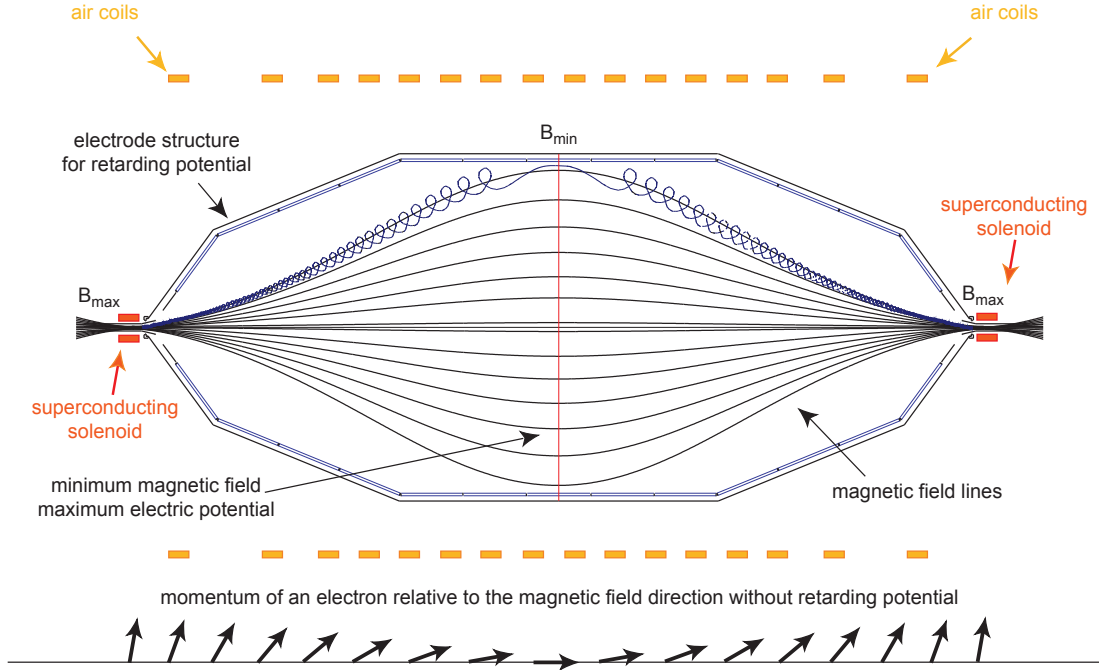


**Figure 4.1:** Schematic overview of the KATRIN MAC-E filter. Shown are the spectrometer hull with the inner wire electrode system (see section 5.2 for details), the solenoids generating the magnetic field and the air coil system compensating the earth magnetic field. In blue the exaggerated cyclotron motion of an electron at the edge of the fluxtube along a magnetic field line (black) is shown. At the bottom of the figure the change of the direction of momentum of the electron is shown along its path through the spectrometer. The red perpendicular line indicates the analysing plane in the middle of the spectrometer. At this position, the electric field has its maximum while the magnetic field reaches its minimum value (in an ideal spectrometer). Figure taken from [Hug08].

## 4.2 Adiabatic energy transformation and energy resolution

To discuss the kinematics and the resulting energy resolution, an electron will be examined starting in the centre of the solenoid with the maximum magnetic field  $B_{\max}$ . As the maximum Lorentz-factor of tritium  $\beta$  decay electrons is

$$\gamma_{\max} = \frac{1}{\sqrt{1 - \frac{v^2}{c^2}}} = 1.04 \approx 1, \quad (4.1)$$

a non-relativistic approximation will be used in this chapter.

The kinetic energy  $E_{\text{kin}}$  of electrons with an angle  $\Theta$  between the velocity vector and the guiding magnetic field line can be written as the sum of the longitudinal and tangential components:

$$E_{\text{kin}} = E_{\parallel} + E_{\perp} \quad (4.2)$$

with

$$E_{\perp} = E_{\text{kin}} \sin^2 \Theta \quad (4.3)$$

$$E_{\parallel} = E_{\text{kin}} \cos^2 \Theta. \quad (4.4)$$

The transversal energy  $E_{\perp}$  corresponds to the energy of the cyclotron motion.

The cyclotron radius  $r_{\text{cycl}}$  of the cyclotron motion can be calculated considering the balance of the forces. The centripetal force  $F_c$  must equal the Lorentz force  $F_L$  induced by the magnetic field  $B$ , hence

$$F_L = eBv_{\perp} = \frac{m_e v_{\perp}^2}{r_{\text{cycl}}} = F_c \quad (4.5)$$

with  $v_{\perp}$  denoting the electron speed perpendicular to the magnetic field. The energy of an electron in this direction is

$$E_{\perp} = \frac{1}{2} m_e v_{\perp}^2 \quad (4.6)$$

By inserting eq. 4.6 into eq. 4.5 one obtains the cyclotron radius

$$r_{\text{cycl}} = \frac{\sqrt{2m_e E_{\perp}}}{eB}. \quad (4.7)$$

It depends on the magnetic field strength  $B$  and the transversal kinetic energy of the electrons.

Due to the cyclotron motion the electrons have a magnetic moment  $\mu$  which can be written as:

$$\mu = |\vec{\mu}| = \frac{E_{\perp}}{B}. \quad (4.8)$$

If the magnetic field changes only slightly over a cyclotron period, the electrons are guided adiabatically. This means that the motion can compensate for changes in the magnetic field by adapting the cyclotron radius. The magnetic flux  $\Phi = \int B dA$  enclosed by the cyclotron track is conserved then. This can be expressed as

$$\gamma\mu \approx \mu = \frac{E_{\perp}}{B} = \text{const.} \quad (4.9)$$

Therefore the transversal energy  $E_{\perp}$  will drop together with the magnetic field strength when the electron approaches the middle of the spectrometer. From eq. 4.2 follows that this energy is transformed in longitudinal energy, as also illustrated at the bottom of figure 4.1.

From eq. 4.9 the energy resolution  $\Delta E$  of an ideal MAC-E filter can be derived. It is assumed that an electron starts in the centre of the field coil with the maximum kinetic energy  $E_{\text{kin,start}}^{\text{max}}$  stored in the transversal energy component  $E_{\perp,\text{start}}^{\text{max}}$ . When the electron reaches the analysing plane with the minimum magnetic field  $B_{\text{ana}}$ , it still retains a small amount  $E_{\perp,\text{ana}}$  of transversal energy which is determined by the magnetic field in the analysing plane:.

$$\frac{E_{\text{kin,start}}^{\text{max}}}{B_{\text{max}}} = \frac{E_{\perp,\text{start}}^{\text{max}}}{B_{\text{max}}} = \mu = \frac{E_{\perp,\text{ana}}^{\text{max}}}{B_{\text{ana}}} \quad (4.10)$$

The magnetic field lines are parallel to the electric field at the analysing plane. Thus, the remaining transversal energy  $E_{\perp,ana}^{\max}$  is not analysed by the retarding potential and therefore determines the energy resolution

$$\Delta E = E_{\perp,ana}^{\max} = E_{kin,start}^{\max} \frac{B_{ana}}{B_{max}} \quad (4.11)$$

of an ideal spectrometer.

For the KATRIN experiment, the maximum starting energy  $E_{kin,start}^{\max}$  is given by the endpoint energy  $E_0 \approx 18.6$  kV of the tritium  $\beta$  spectrum. The magnetic field drops by a factor of 20000 from the maximum value  $B_{max} = 6$  T at the pinch magnet to a minimum of  $B_{ana} = 3$  G =  $3 \cdot 10^{-4}$  T at the analysing plane. Hence, the energy resolution is

$$\Delta E = \frac{B_{ana}}{B_{max}} E_0 = \frac{3 \cdot 10^{-4} \text{ T}}{6 \text{ T}} 18600 \text{ eV} = 0.93 \text{ eV}. \quad (4.12)$$

This corresponds to a relative resolution of  $\Delta E/E_0 = 5 \cdot 10^{-5}$ .

### 4.3 Transmission properties

On the way from the entrance region to the analysing plane of the spectrometer, most of the transversal energy of the electrons is transformed into longitudinal energy. As stated above, only the longitudinal component of the electron energy can be analysed with the retarding potential  $U_0$ . Thus, electrons with the same starting energies but different starting angles have different transversal energies and therefore also different longitudinal energies in the analysing plane. The retarding potential at which electrons with a fixed kinetic energy will just pass the filter therefore depends on the starting angles. This gives rise to the calculated energy resolution.

To overcome the retarding potential  $U_0$ , the longitudinal energy of an electron in the analysing plane must be greater zero:

$$E_{\parallel,ana} > 0 \quad (4.13)$$

It can be expressed as

$$E_{\parallel,ana} = E_{kin,ana} - E_{\perp,ana} \quad (4.14)$$

$$= E_{kin,ana} - E_{\perp,start} \frac{B_{ana}}{B_{max}} \quad (4.15)$$

$$= (E_{kin,start} - qU_0) - E_{kin,start} \sin^2 \Theta_{start} \frac{B_{ana}}{B_{max}} > 0 \quad (4.16)$$

Hence, a transmission condition is be given by

$$\Theta_{start} \leq \Theta_{max} = \arcsin \sqrt{\frac{E_{kin,start} - qU_0}{E_{kin,start}} \frac{B_{max}}{B_{ana}}}. \quad (4.17)$$

Only electrons with a starting angle  $\Theta_{start}$  within the cone spanned by the angle  $\Theta_{max}$  can overcome a given retarding potential  $U_0$ .

The tritium source of the KATRIN experiment features a magnetic field  $B_{\text{source}} = 3.6 \text{ T} < B_{\text{max}}$ . Electrons coming from the source therefore have to migrate into a region with a higher magnetic field strength. Hence, they are subject to the magnetic mirror effect, which reflects electrons with angles higher than a critical angle

$$\Theta_{\text{mirror}} = \arcsin \sqrt{\frac{B_{\text{source}}}{B_{\text{max}}}} \approx 50.77^\circ. \quad (4.18)$$

This is a favourable condition, as these electrons have longer pathlength and therefore a higher chance for scattering processes in the source section.

Using the abbreviation  $E_{\text{kin}} = E$  one obtains the analytic transmission function  $T(E, U_0)$  of a MAC-E filter as shown in figure 4.2:

$$T(E, U_0) = \begin{cases} 0 & E - qU_0 < 0 \\ \frac{1 - \sqrt{1 - \frac{E - qU_0}{E} \frac{B_{\text{source}}}{B_{\text{ana}}}}}{1 - \sqrt{1 - \frac{\Delta E}{E} \frac{B_{\text{source}}}{B_{\text{ana}}}}} & \text{for } 0 \leq E - qU_0 \leq \Delta E. \\ 1 & \Delta E \leq E - qU_0 \end{cases} \quad (4.19)$$

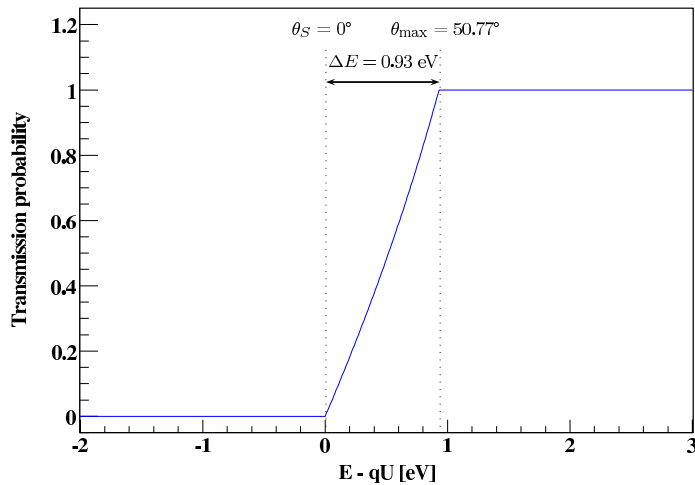


**Figure 4.2:** The analytic transmission function as given by eq. 4.19. The width of the transmission function is determined by the maximum starting angle  $\Theta$ . Figure taken from [Wol08].

In the KATRIN main spectrometer, an inner electrode system is installed for background suppression (see section 4.6). This electrode system has a big influence on the electric fields inside the spectrometer. It is important to assure that the longitudinal energy  $E_{\parallel}$  of the electrons in the fluxtube is always greater zero not only in the analysing plane, but on the whole way through the spectrometer. Otherwise, the electrons cannot reach the analysing plane as they are reflected. This can be avoided with a proper electrode design. The problem is most prominent in the entrance and exit regions of the KATRIN main spectrometer and will be discussed in detail in chapter 6.

## 4.4 Electric and magnetic field inhomogeneities

For the derivation of the transmission properties in the last section it was assumed that the retarding potential  $U_0$  and the magnetic field strength are constant in the whole analysing plane. For a real spectrometer, this is not the case.

The electric potential across the analysing plane is not constant because of the influence of parts of the inner electrode system (see 4.6) with potentials  $U \neq U_0$  and the fact that the spectrometer has not an infinite length.

For the KATRIN main spectrometer, the potential depression  $\Delta U$  is defined as the difference of the electric potential in the middle of the analysing plane to the potential at the edge of the fluxtube at  $r = 4.5$  m:

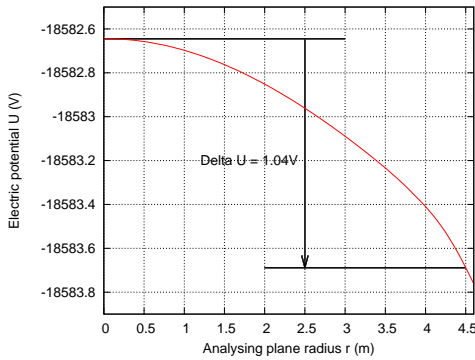
$$\Delta U := U(r = 0) - U(r = 4.5 \text{ m}) \quad (4.20)$$

It amounts to  $\Delta U = 1.04$  V for the electrode setup proposed in this thesis (see figure 4.3(a)).

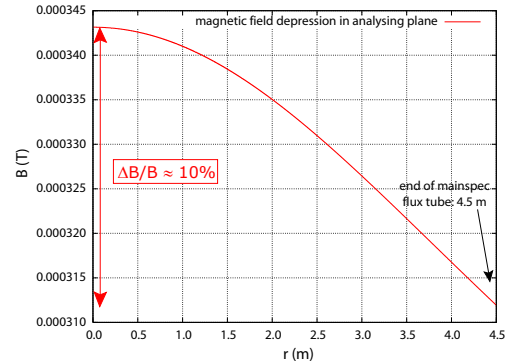
Like the electric potential, also the magnetic field strength is not constant over the analysing plane. This leads to a radial dependence of the energy resolution and an additional broadening of the transmission function. The magnetic field depression  $\Delta B$  is defined similar to  $\Delta E$ . For the KATRIN main spectrometer it is  $\Delta B \approx 0.31$  G, as shown in figure 4.3(b).

The impact of magnetic and electric field inhomogeneities is shown in figure 4.4. The effect of the electric field inhomogeneity is much larger than the effect of the magnetic field deviation.

To compensate for these effects, the transmission function has to be measured experimentally for different regions of the analysing plane (which correspond to different start and detector radii). This calls for a segmented detector, as will be used in the KATRIN experiment (see section 5.1.5).



(a) Electric field depression



(b) Magnetic field depression (figure taken from [Hug08])

**Figure 4.3:** The electric potential depression and magnetic field depression along the analysing plane ( $Z = 0$ ) for the KATRIN main spectrometer.

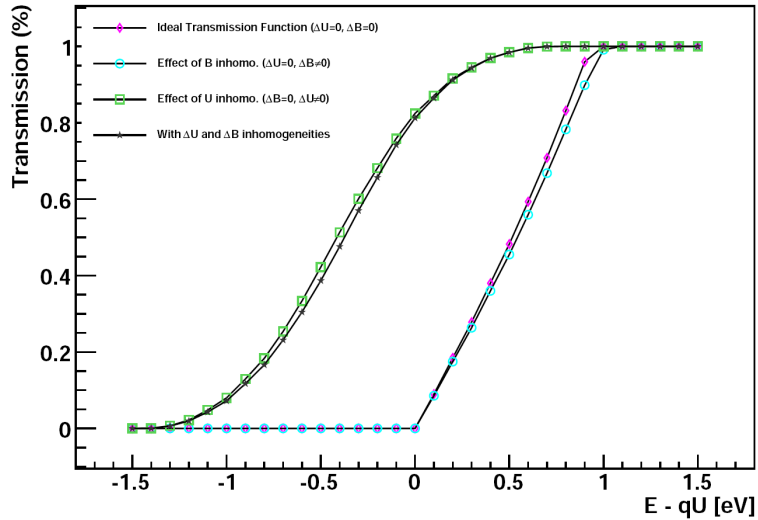


**Figure 4.4:** Monte-Carlo simulation of the transmission function of the KATRIN main spectrometer. Shown is a simulation of the transmission function with and without magnetic and/or electric field inhomogeneities of  $\Delta U \approx 1.2$  V and  $\Delta B \approx 0.4$  G along the analysing plane. Figure taken from [Dun07].

## 4.5 Background sources

As seen in the previous sections, a MAC-E filter is a high precision instrument well suited to analyse the endpoint region of the tritium  $\beta$  spectrum with its low countrates. Connected to the low expected signal rate is the demand for low a background rate. As the endpoint region holds most of the information on the neutrino mass, a higher background level leads to longer measurement times and a larger effect of systematic errors on the neutrino mass. For the KATRIN experiment, a total background rate of 10 mHz is accepted to achieve the required sensitivity of  $m(\bar{\nu}_e) < 0.2$  eV with 90% confidence level in a measurement time of 36 month [KAT04].

Some possible background sources for MAC-E filters will be discussed in the next paragraphs with special regard to the KATRIN main spectrometer.

### 4.5.1 Electrons emitted from the vessel hull

Electrons can be emitted from the vessel hull by incident cosmic muons or due to the decay of radioactive isotopes in the material of the vessel hull. Under certain conditions<sup>1</sup> electrons produced in such processes may enter the sensitive spectrometer volume. If they reach the detector, they account for background. A possible way to reduce the background of those sources is the insertion of an inner wire electrode into the spectrometer, as described in section 4.6.

<sup>1</sup>See e.g. [Glu05] for details.

### 4.5.2 Penning Traps

The Penning trap and the corresponding discharge mechanism was already explained in chapter 3.3. Penning traps inside the main spectrometer can give rise to an increased background or cause voltage and/or pressure instabilities.

Traps located inside the fluxtube region of the spectrometer are very critical. Electrons emerging from such traps just need enough energy to reach the detector to contribute to the background.

The expected background induced by traps outside the fluxtube is not as high because of the magnetic shielding properties of a MAC-E filter (see section 4.6). Nevertheless, plasma instabilities or space charge effects could allow particles to penetrate into the fluxtube region or cause voltage and/or pressure instabilities. Hence, these Penning traps are still dangerous and have to be avoided.

An inner electrode system can be helpful to suppress Penning traps because more complex geometries can be realised compared to the spectrometer vessel alone. On the other hand, Penning trap can be introduced in the spectrometer by the more complicated electrode geometry. Well chosen geometries can avoid the development of Penning traps or reduce their trap depth. This is discussed in detail in chapter 6.

### 4.5.3 Bumps in the longitudinal energy along the spectrometer

Another type of particle trap can be found when following the longitudinal energy of electrons along the spectrometer. Assuming they started at the spectrometer entrance with just enough energy to reach the analysing plane, electrons in an ideal spectrometer loose their longitudinal energy constantly until  $E_{\parallel} = 0$  is reached in the analysing plane. This behaviour can be disturbed by unfavourable electrode geometries. In such setups, bumps in the course of  $E_{\parallel}$  can develop as shown in figure 4.5. These bumps can host a particle trap. A possible trapping scenario is an electron which reaches the trapping region, looses its longitudinal energy and thus is stored in this region.

As it is not clear to what extend this effects can produce particle traps that account for additional background, they have to be avoided.

### 4.5.4 Field emission

An inner electrode system can be used to reduce the background in a MAC-E filter (see section 4.6). As typically several different potentials are applied to the structure, high electric field strength can occur. As discussed in section 3.1, this can lead to field emission. As the emitted electrons can reach the fluxtube and thus contribute to the background, high electric field strengths have to be avoided in the electrode design.

For the optimisation of the electrode system in the flange region of the KATRIN main spectrometer discussed in chapter 6 this is taken into account. An experimental study of the possible occurrence of field emission at the wire electrode of the main spectrometer can be found in chapter 7.

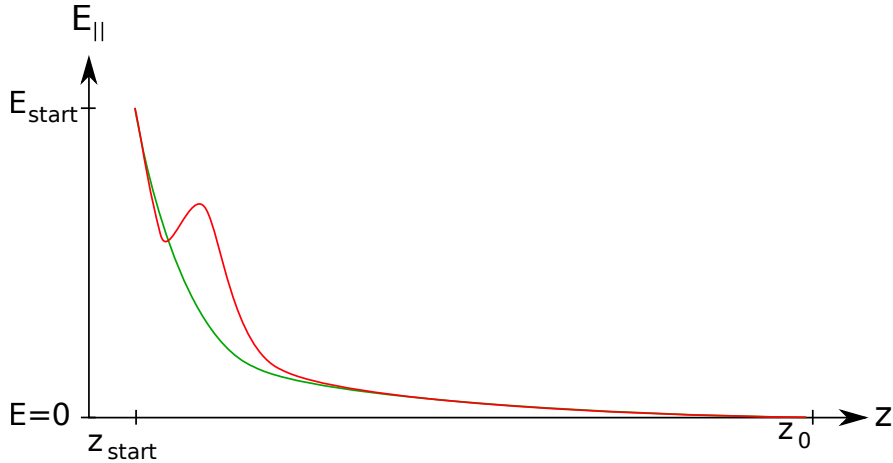


**Figure 4.5:** Schematic view of possible traps indicated by bumps in the longitudinal energy  $E_{\parallel}$  along the spectrometer. Shown is the longitudinal energy of an electron started at the spectrometer entrance  $z_{start}$  with  $E_{\parallel, start} = eU_0$  which allows the electron to just reach the analysing plane. The green line shows an ideal progression where the electron continuously loses its longitudinal energy until it reaches  $E_{\parallel} = 0$  at  $z_{start}$ . The red line shows a disturbed case with a bump indicating a possible trap position.

## 4.6 Background suppression with an inner wire electrode

Because of the large magnetic field, a MAC-E filter features an inherent magnetic shielding. This can prevent charged particles from the walls from reaching the detector. The transfer efficiency  $\varepsilon$  for electrons emitted from the vessel hull to the detector has been measured for the Mainz ( $\varepsilon = 10^{-5}$ ) and Troitsk ( $\varepsilon = 10^{-6}$ ) spectrometers. For the KATRIN experiment, a factor of similar order is expected [KAT04].

Nevertheless, the background can be reduced further by the insertion of an inner wire electrode as illustrated in figure 4.6. The wire grid is on a more negative potential than the vessel hull. If the energy of an electron emitted from the vessel hull is not high enough to pass the potential barrier, it is reflected back to the vessel hull. The efficiency of this screening is given by the screening factor (see [Val09] and references therein)

$$S = 1 + \frac{2\pi L}{s \ln \frac{s}{\pi d}}. \quad (4.21)$$

Here  $s$  denotes the spacing between the wires of the grid which have a diameter  $d$ . The grid is mounted at a distance  $L$  to the vessel hull.

Although a larger diameter of the wires increases the screening factor, the wires may not be too thick: With the diameter also the mass of the wires increases, with the consequence of an increasing background due to the same reasons (radioactivity, incident muons) as for the vessel hull. Also, a wire electrode needs some kind of mounting frame, which also acts as a source of background electrons.

For the KATRIN main spectrometer, the design has been optimised by introducing a wire electrode with a second, inner<sup>2</sup> wire layer with a smaller diameter. This wire layer

<sup>2</sup>The inner wire layer is the layer facing the spectrometer inside.

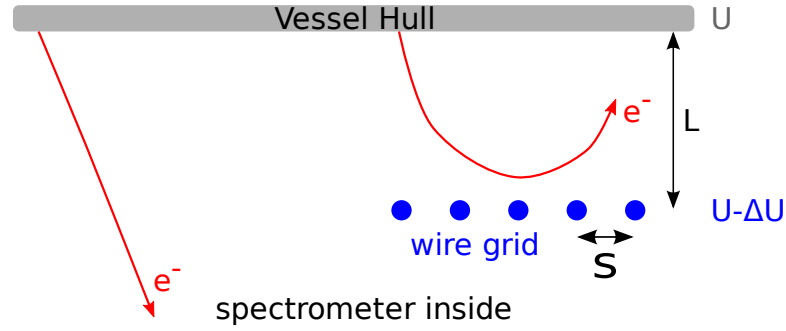


**Figure 4.6:** Schematic view of the principle of background suppression with a wire screening grid. On the left side, without a wire grid, electrons emitted from the vessel hull (by radioactivity or incident cosmic muons) can enter the spectrometer volume. On the right side the wire electrode (wire diameter is exaggerated) is depicted. As it is put on a more negative potential, electrons are reflected to the vessel hull and thus cannot give rise to background.

then shields the outer wire layer that has a larger wire diameter. This is illustrated in figure 4.7.

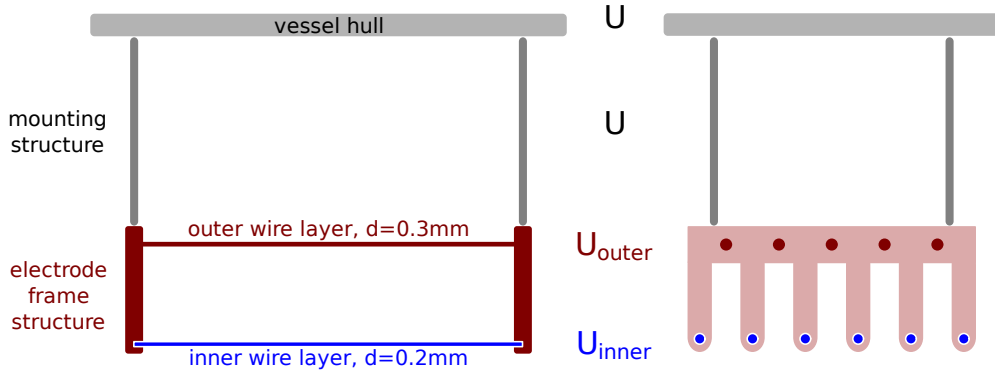


**Figure 4.7:** Schematic view of a dual layer wire electrode for background suppression viewed from the side and from the front. Shown is the vessel hull with a simplified mounting structure and an element of a dual layer wire electrode with a simplified frame structure to hold the wires. Based on the principle illustrated in figure 4.6, this setup provides better shielding than a single layer electrode.

The vessel hull and the mounting structures for the electrode frames are on the same potential  $U$ . They are shielded by the thick outer wire layer ( $d_{\text{outer}} = 0.3 \text{ mm}$ ) which is on a more negative potential  $U_{\text{outer}} = U - 100 \text{ V}$ . The wires are mounted into a frame structure which is also on the potential  $U_{\text{outer}}$ .

The thin inner wire layer ( $d_{\text{inner}} = 0.2 \text{ mm}$ ) with an even more negative potential  $U_{\text{inner}} = U - 200 \text{ V}$  provides shielding for the electrons emerging from the outer wire material and large parts of the frame structure. The electrode frame structure is formed like a comb to keep the mass low.

For details on the inner wire electrode setup see section 5.2.

# 5 The KATRIN experiment

In the last decades there was a significant improvement of the neutrino mass limits by investigating the  $\beta$ -spectrum of tritium. The Mainz and Troitsk neutrino mass experiments have yielded the currently best upper limits on the mass of the electron antineutrino using the kinematics of  $\beta$  decay.

The goal of the KATRIN experiment is to improve the sensitivity for the kinematic measurement of the neutrino mass by an order of magnitude, thus reaching the meV scale. With three years worth of data, the KATRIN experiment aims to be able to detect a neutrino mass of  $m(\bar{\nu}_e) = 0.3 \text{ eV}/c^2$  with  $3\sigma$  significance. A mass of  $m(\bar{\nu}_e) = 0.35 \text{ eV}/c^2$  will be detected with  $5\sigma$  significance. In case no evidence for a non-zero neutrino mass is found, KATRIN will set a new upper limit of  $m(\bar{\nu}_e) < 0.2 \text{ eV}/c^2$  with 90% confidence level [KAT04].

Like its predecessor experiments, KATRIN relies on a MAC-E filter type spectrometer. A major role in the improvement of the sensitivity play the gaseous tritium source and the enhanced size of the main spectrometer. The main spectrometer is the currently biggest MAC-E filter with a nominal length of 23.28 m and a diameter of 9.8 m. Along with that, many other aspects of the experiment also have to be improved in order to accommodate this high sensitivity.

In the following sections the main components of the KATRIN experiment will be described. The inner electrode system of the spectrometer will be explained in more detail in section 5.2.

## 5.1 KATRIN components

The KATRIN setup can be subdivided into several sections. Figure 5.1 shows an overview of these sections.

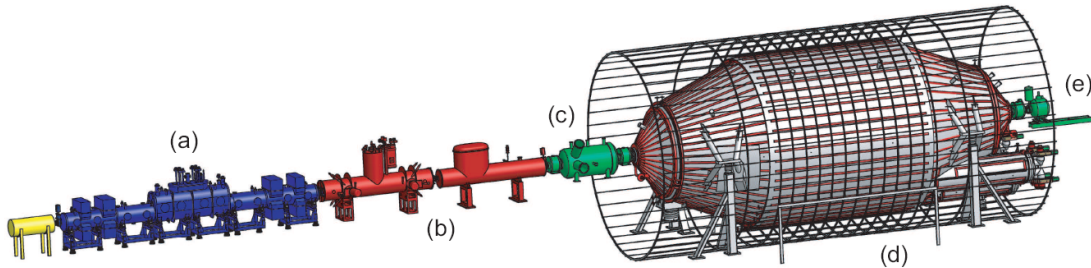


**Figure 5.1:** Overview of the KATRIN experiment: a) source section, b) transport section, c) pre-spectrometer, d) main spectrometer surrounded by air coils, e) detector.

### 5.1.1 Windowless gaseous tritium source (WGTS)

The main source for the KATRIN experiment is a windowless gaseous tritium source. It is one of the most complicated parts of the KATRIN setup. Because the effect of the neutrino mass on the spectrum is best visible in the endpoint region of the tritium  $\beta$  spectrum, a source with a high intensity is needed. Also, systematic effects have to be understood well so they can be accounted for.

A solid tritium source with the desired decay rate of  $10^{11}$  Bq/s would show charge effects up to 10 V across the frozen film [Ott08], preventing to achieve the desired energy resolution of  $\Delta E < 1\text{eV}$ . In gaseous sources there is no such effect, but the construction of such a source is much more complicated.

The WGTS has a length of 10 m, the decay tube has a diameter of 90 mm. It is kept at a temperature of 27 K and is located in a homogeneous magnetic field of  $B_{\text{source}} = 3.6$  T. The tritium is injected in the middle of the source and removed at both ends of the source by turbo molecular pumps to be repurified and injected into the source again. The intended tritium flow rate is  $5 \cdot 10^{19}$  molecules/s, which requires a total amount of 40 g  $T_2$  to be available on site. This supported the Forschungszentrum Karlsruhe (FZK) as location for the experiment, as it hosts Europe's largest tritium lab.

### 5.1.2 Transport section

The gas flow from the WGTS has to be reduced drastically before reaching the spectrometers to prevent a tritium contamination. To achieve an upper limit of  $10^{-14}$  mbar l/s entering the pre-spectrometer, the reduction of the gas flow is done in two steps.

First tritium that escapes the source is removed by turbo molecular pumps in a differential pumping section. Then, in a second step, the remaining tritium molecules are frozen on the surface of the beam tube which is covered with frozen argon (cryo pumping section).

To improve the efficiency of the pumping, the electron flux is guided magnetically through bends in the beam line while neutral gas atoms move in a straight line. Thus, they can be removed at the corners of the bends more easily.

### 5.1.3 Pre-spectrometer

The pre-spectrometer is a spectrometer of the MAC-E type (see chapter 4) with a length of 3.4 m and a diameter of 1.7 m. It features an inner wire electrode and full metal electrodes at the entrance and exit regions for background suppression (see section 4.6 for more details about the wire electrode principle). In the KATRIN experiment the pre-spectrometer fulfils different purposes.

In the early phase of the experiment, it is used as a test setup in order to gain a better understanding of the mechanisms which are important in MAC-E filter type spectrometers. Especially the inner wire electrode and the full metal electrodes are important factors as they provide useful information on background reduction and Penning trap properties which can then be adopted for the main spectrometer.

In the final KATRIN setup, the pre-spectrometer will reduce the electron flux from the source section (which is of the order  $10^{10} \text{ s}^{-1}$ ) by reflecting the for the measurement of the endpoint region of the tritium  $\beta$  decay uninteresting electrons with  $E \lesssim E_0 - 200 \text{ eV}$ .

This is done to reduce background effects. Hence, the energy resolution  $\Delta E \lesssim 100$  eV of this spectrometer is not crucial. The remaining electron flux to the main spectrometer is of the order  $10^4 \text{ s}^{-1}$ .

### 5.1.4 Main spectrometer

The main spectrometer (see also figure 5.3) is the main tool for the precision analysis of the tritium  $\beta$  spectrum. It is a MAC-E filter with a nominal length of 23.28 m and a central radius of 4.9 m. The magnetic field drops by a factor of 20000 from the pinch magnet at the detector side to the analysing plane, leading to a resolution of  $\Delta E = 0.93$  eV in the region of the tritium endpoint energy  $E_0 \approx 18.6$  keV (see chapter 4 for a detailed derivation and details about the MAC-E filter principle).

To correct for the earth magnetic field, the main spectrometer is surrounded by an air coil system.

An integrated tritium spectrum can be measured by varying the electric retarding potential  $U_0$  of the main spectrometer and counting the electrons at the detector.

As the pre-spectrometer, the main spectrometer features an inner electrode system for background reduction as explained in section 4.5. The inner electrode system will be discussed more in detail in section 5.2.

### 5.1.5 Detector

A segmented 148 pixel PIN diode will be used as a detector. In figure 5.2 the detector layout is shown. Each segment has the same sensitive area. By segmenting the detector a spatial resolution is achieved. This is required to correct for the inhomogeneities in the electric potential and the magnetic field in the analysing plane (see section 4.4) as well as to improve the analysis of the background noise generated in the spectrometers. In principle, the detector does not need to have a high energy resolution, as the precise analysis of the energy spectrum is done by the main spectrometer. But to improve background suppression, a reasonable good energy resolution is still needed. The aspired resolution is about 600 eV in the region of the tritium endpoint.

For an adequate background suppression, the detector will feature an active and passive shielding. A possible post-acceleration voltage of 30 keV improves the reduction of background effects.

An additional detector magnet creates a magnetic field to further reduce background effects and to guide the electrons to the sensitive area of the detector. The strength of this magnetic field will either be  $B_{\text{det}} = 3.5$  T or  $B_{\text{det}} = 6$  T.

As the detector magnetic field has an influence on the magnetic fields in the vicinity of the main spectrometer, both cases have to be included in the electrode design simulations presented in chapter 6.

## 5.2 The inner wire electrode of the main spectrometer

As stated in section 5.1.4, the KATRIN main spectrometer features an inner electrode system to reduce background and to improve the possibility to shape the electric fields. The principle of a wire electrode was already discussed in section 4.6.

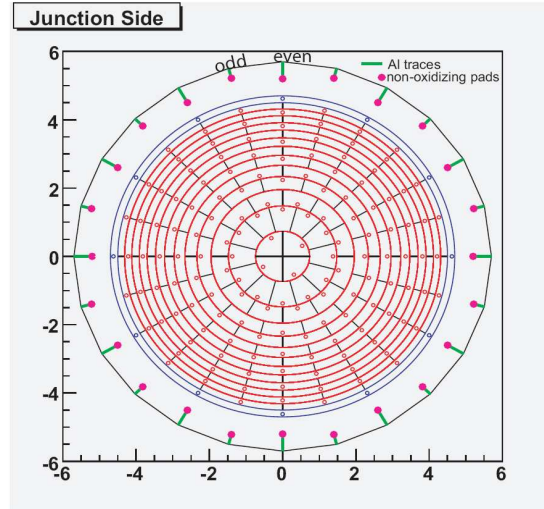


**Figure 5.2:** The segmented PIN diode detector (figure taken from [Ste07])

### 5.2.1 Modular setup of the electrode system

The inner electrode system consists of single and dual layer wire electrodes as well as full metal electrodes. It is built in a modular way, as can be seen in figures 5.3 and 5.4.

The wire electrode is divided into 16 electrode rings numbered from 02 (source side) to 16 (detector side). A ring consists of a varying number of modules, ranging from 20 modules in the cylinder part of the spectrometer to only 4 modules for the very outer wire electrode rings 02 and 16. The number of modules and other parameters of the wire electrode are given in table 5.1.

The electrodes at the entrance and exit regions are implemented as full metal electrodes consisting of thin sheets of metal. The protruding electrode ends need to be stabilised by an end bulge (ground electrode) or an end ring (shielding electrode). These end bulges or end rings also serve the purpose to reduce the electric field strengths at these positions. Details on the mechanic setup of the shielding electrode can be found in section 6.2.1.

**Table 5.1:** Parameters of the main spectrometer inner electrode system

module ring	number of modules	number of layers	wires per module and layer	wire diameter (inner/outer)
07-11	20	2	60	0.2 mm / 0.3 mm
06 / 12	20	2	52	0.2 mm / 0.3 mm
05 / 13	20	2	42	0.2 mm / 0.3 mm
04 / 14	20	2	34	0.2 mm / 0.3 mm
03 / 15	10	1	40	0.2 mm
02 / 16	4	1	50	0.2 mm

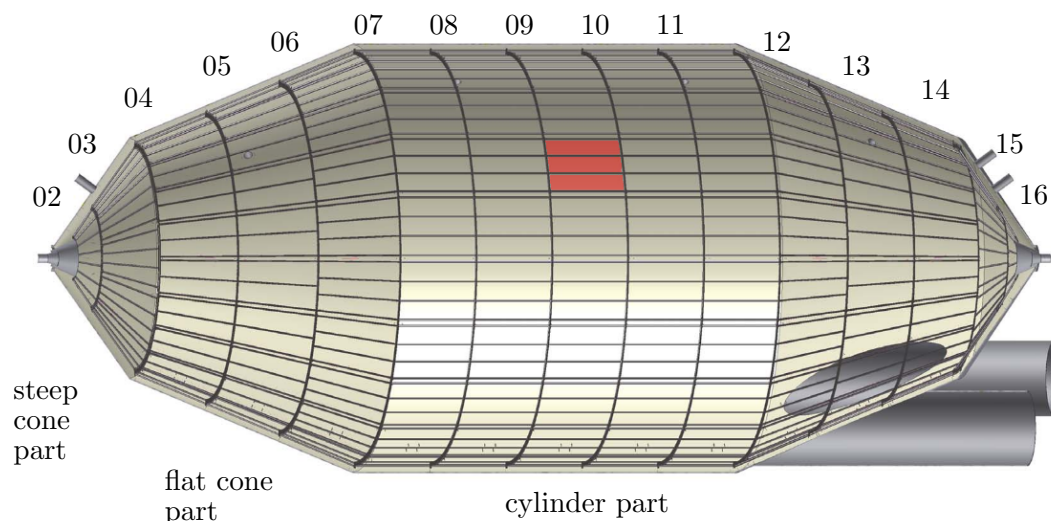


**Figure 5.3:** Cutaway drawing showing the modular setup of the inner electrode of the main spectrometer. The individual module rings are numbered. The area covered by one module of ring 09 is marked in red. On the lower right of the drawing the pumping ports are visible.

## 5.2.2 Wire electrode modules

As the overall shape of the inner electrode system follows the form of the vessel hull, there are electrode modules with several different forms. All wire modules consist of two comb- or ring-like structures called combs<sup>1</sup> which are connected by c-shaped profiles (c-profiles). While for the cylinder and flat cone part modules with two wire layers are used, the steep cone modules only have a single wire layer.

**Mounting of the wires** The wires are mounted into the combs by ceramic insulators (see figure 5.5(a)). They hold the wires in place by friction and insulate them electrically from the combs.

The potential for the wires is distributed by a crosswire on the outside of the combs which connects all wires of one layer in a module (see figure 5.5(b)).

**Dual wire layer modules** For the wire electrode modules of the cylinder and flat cone part, two wire layers are used for an improved background reduction. The electrode module frame structure has to house both wire layers in a way that assures mechanical stability and feasibility but also maintain a small mass and surface to reduce background effects and to improve vacuum properties. For the dual layer electrodes, this is realised by two metal combs connected by c-profiles. An example of a dual layer electrode module is shown in figure 5.6.

As explained in section 4.6), the inner wire layer is on a electric potential which is 100 V more negative as the inner wire layer to improve background suppression. For the outer

<sup>1</sup>Both structures are called combs to avoid ambiguousness with the module rings (e.g. module ring 02).

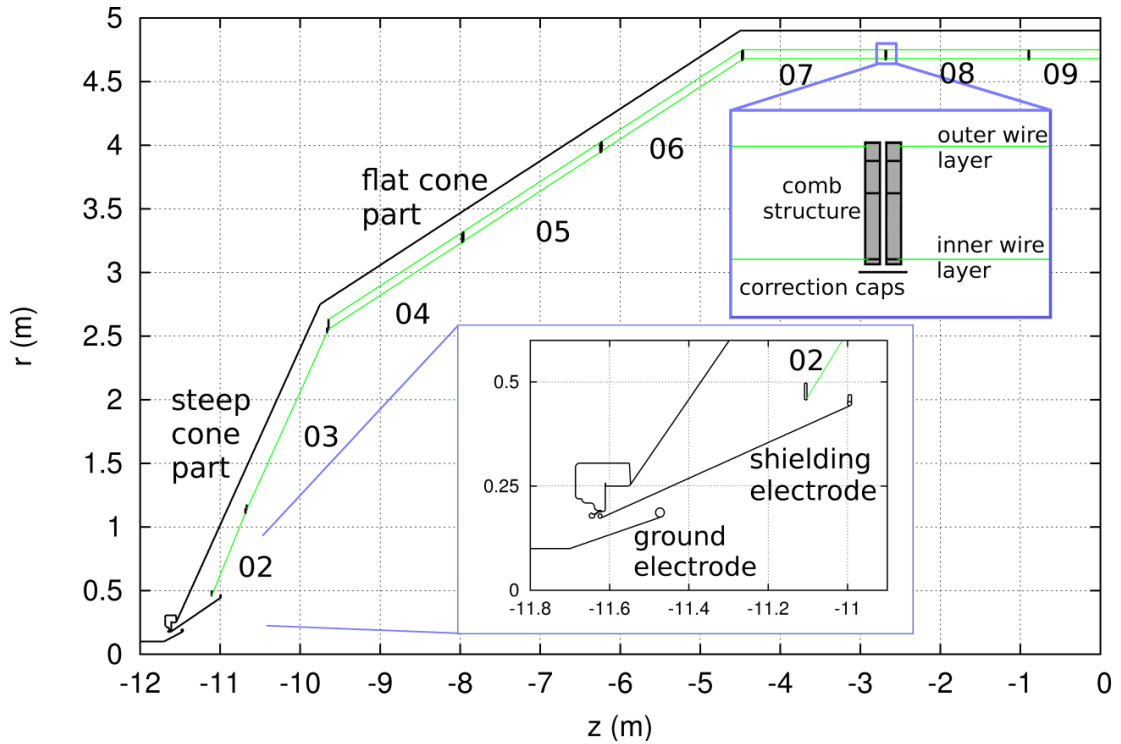


**Figure 5.4:** A schematic view of the electrode geometry. Wires are green, solid metal parts are black. The magnification shows the cap structure used to improve the electric field homogeneity for the central modules (see section 5.2.3). As the geometry is mirrored in the  $z = 0$  plane, only one spectrometer side is shown.

wire layer shorter ceramics are used to mount the wires so that the crosswire has direct contact to the comb, putting the wires on comb potential as desired. For the inner wire layer the ceramics are longer so that the crosswire does not touch the comb. Hence the wires are insulated from the comb and can be put on a different potential<sup>2</sup>.

**Single wire layer modules** For the steep cone region two layers were not feasible mechanically because of the steep angle of the modules and the resulting shear forces<sup>3</sup>. Therefore, only a single wire layer is used. This can be tolerated as in the steep cone region the high magnetic field strength are expected to provide a high magnetic shielding (see section 4.6).

As only one wire layer is used, the comb structure used for the dual layer modules is exchanged for simple rings as is shown in figure 5.7 in the steep cone part. Like the inner wire layer of the dual layer modules, the wires are mounted into the combs by

<sup>2</sup>This is done by connecting the crosswire to high voltage connectors mounted at the sides of the c-profiles

<sup>3</sup>The modules have be built in a way that the comb plane is perpendicular to the spectrometer symmetry axis. This way the combs remain plain. Placing the combs perpendicular to the vessel hull would result in twisted comb geometries with only bent surfaces which cannot be produced mechanically in a reasonable way.

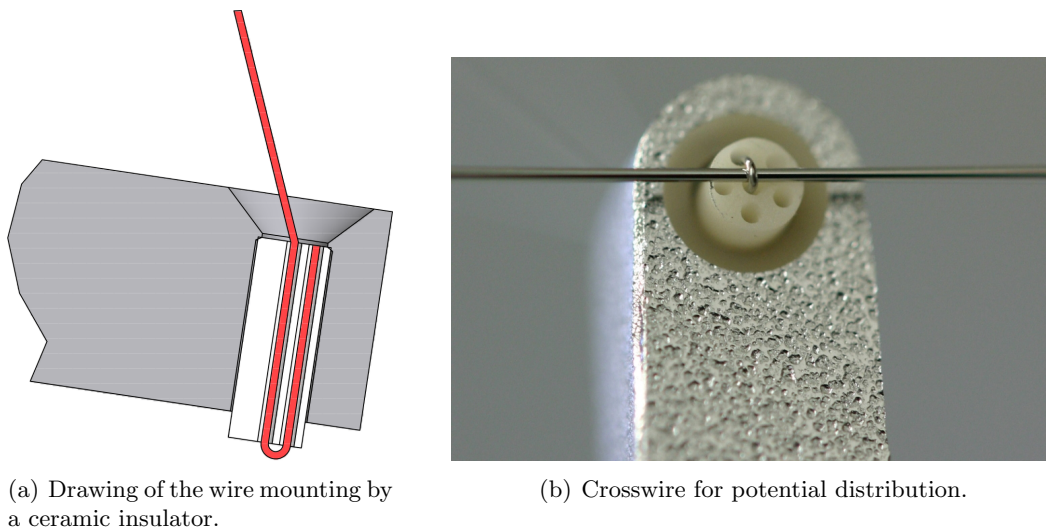


**Figure 5.5:** *The mounting of the wires. (a) shows how the wires are held in place by the ceramics. The crosswire is not shown. (b) is a picture of a wire mounting position of the inner layer. The crosswire is used to distribute the electric potential.*

longer ceramics so that they can be put on a different electric potential. Also here the potential is distributed by a crosswire.

### 5.2.3 Cylinder module caps

As inhomogeneities of the electric field have a big impact on the transmission properties at the analysing plane, special care has to be taken to smooth the electric fields in this region. The combs of the cylinder modules produce distortions of the electric field since they are at set to 100 V more positive potential than the inner wire layer.

To shield this positive potential, the cylinder modules feature an additional structure at the junctions of the module rings. The junction between the module rings are covered by thin metal barrel hoops which is called caps (see figure 5.8). They consist of a thin metal sheet and are attached to the combs using special formed teeth and a ceramic insulator, as they are put on the same potential as the inner wire layer. This way they shield the more positive potential of the combs.

Totally there are 4 rings of these corrections caps, one for each ring junction between the rings 07, 08, 09, 10 and 11.

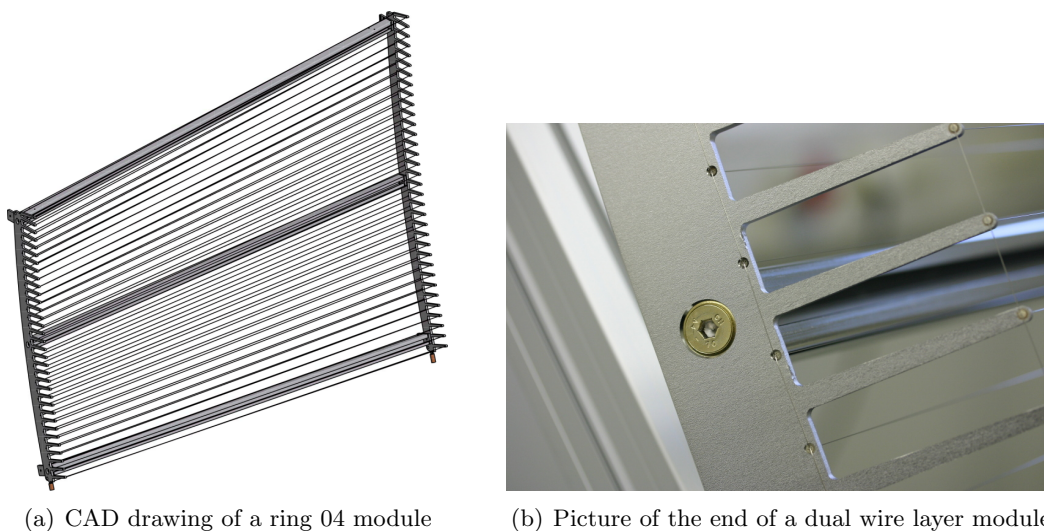


**Figure 5.6:** Drawing (a) and picture (b) of a dual wire layer module. The wires of the inner layer are mounted into the teeth of the combs while the outer wire layer is mounted into the comb body. Longer ceramics for the inner wire layer prevent the crosswire from contacting the comb while the shorter ceramics of the inner layer make sure that the crosswire has contact to the comb. The screws to connect the c-profiles are gold-plated to prevent them from jamming during module production.

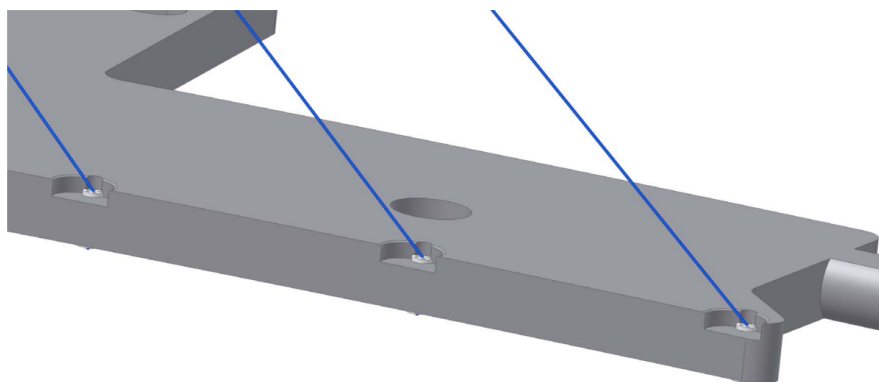


**Figure 5.7:** Drawing of a steep cone electrode mounting ring. The wires (blue) are mounted into the ring using ceramic tubes.

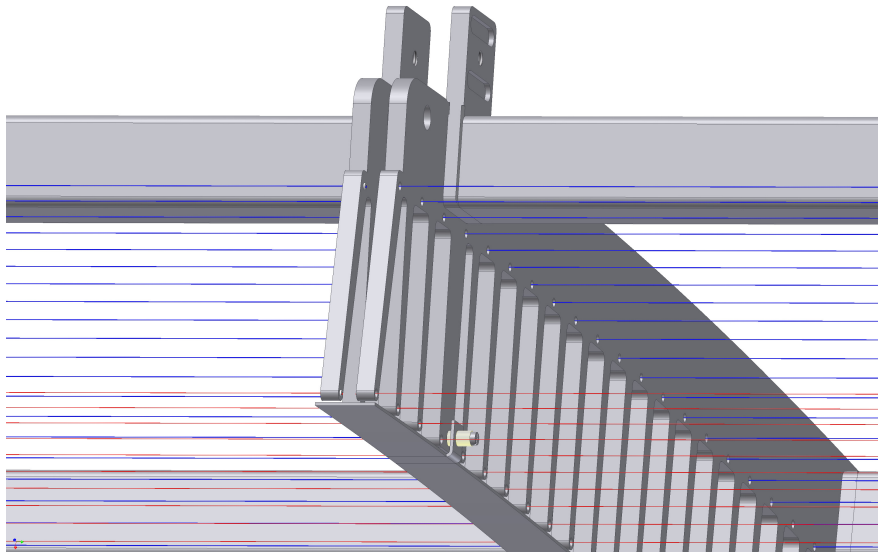


**Figure 5.8:** *Drawing of a the cylinder module caps. The barrel hoops consist of thin metal sheets and are put on the potential of the inner wire layer to shield the influence of the comb potential on the electric field.*



# 6 Design of the inner electrode system of the main spectrometer

In this chapter one of the major topics of this thesis will be discussed, the electromagnetic design of the steep cone part of the KATRIN main spectrometer inner electrode system. The setup of the cylindrical and the flat cone part of the main spectrometer was already fixed at the start of this diploma thesis and is discussed in [Val09].

The design of the steep cone part of the inner electrode system is challenging to design. Several effects like electric field strengths and Penning traps have to be accounted for. In addition, the transmission properties of the main spectrometer are very sensitive to changes in this region. As the space especially in the flange region is very limited, a careful analysis of the electrode system is needed to find a design which does not only takes into account the requirements of the electromagnetic design but is also feasible regarding the mechanical setup and installation. This chapter will describe simulations which have been conducted to find an adequate design of the electrode system.

In the first section, the tools used for the simulations will be explained. Section 6.2 describes the design optimisation process in detail. The last section summarises the obtained parameters and results.

## 6.1 Simulation tools

Because of the special demands resulting from the main spectrometer geometry, most of the simulation tools were created especially for the KATRIN experiment. The principles and programs for the calculation of the electric and magnetic fields were already explained e.g. in [Hug08] and [Voe08]. They are summarised here shortly for the sake of completeness. The argumentation follows the ones presented in these references. More details on the usage of the programs like command line parameters and detailed file formats can also be found in [Hug08].

### 6.1.1 Magnetic field calculations

To calculate the magnetic field generated by an electric current one can use the Biot-Savart law:

$$d\vec{B} = \frac{\mu_0}{4\pi} \frac{I d\vec{l} \times \hat{r}}{r^2}. \quad (6.1)$$

Here  $d\vec{l}$  is an infinitesimal segment of an infinitesimal thin conductor at point  $P$  pointing in the direction of the current  $I$ . This current induces the magnetic field  $d\vec{B}$  at a point  $P'$ , with  $\hat{r}$  denoting the unit vector in direction of  $P'$ . The distance between the  $P$  and  $P'$  is  $r$  (compare figure 6.1).

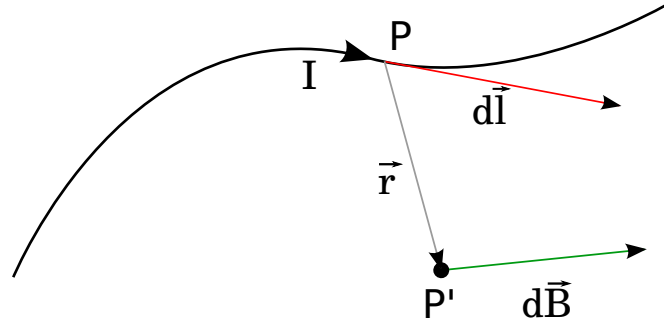


**Figure 6.1:** Illustration to the Biot-Savart law (see eq. 6.1).

If the field coils are lined up along one symmetry axis, the system can be characterised by the  $r$ - $z$  plane in cylindrical coordinates. For thin coil wires it is possible to find an analytical solution for equation 6.1 which uses complete elliptic integrals. If the wire thickness cannot be neglected a numerical calculation for the radial direction is needed. With elliptic integrals the magnetic field can be calculated at every point with a high precision, but at the cost of a large computation time.

A faster method to calculate magnetic fields induced by axial symmetric coils is the use of Legendre polynomial expansion. The field in a point  $\vec{P} = (r, 0, z)$  can be expressed as a function of its derivatives in a so called source point  $z_0$  on the symmetry axis and the Legendre polynomials  $P_n(u)$  [Glu06a]:

$$B_r = -s \sum_{n=1}^{\infty} \frac{B_n^{cen}}{n+1} \left( \frac{\rho}{\rho_{cen}} \right)^n P_n'(u) \quad (6.2)$$

$$B_\phi = 0 \quad (6.3)$$

$$B_z = \sum_{n=0}^{\infty} B_n^{cen} \left( \frac{\rho}{\rho_{cen}} \right)^n P_n(u) \quad (6.4)$$

with  $u = \cos \theta = \frac{z-z_0}{\rho}$  and  $s = \sin \theta = \frac{r}{\rho}$  (see illustration in figure 6.2).  $\rho$  denotes the distance from  $P$  to  $z_0$ ,  $\rho_{cen}(z_0)$  is called the convergence radius and equals the distance from  $z_0$  to the nearest coil. The source coefficients  $B_n^{cen}(z_0)$  are given by an integral over the coil profile:

$$B_n^{cen}(z_0) = \int_{R \in \text{coil body}} dR \int_{Z \in \text{coil body}} dZ b_n(Z, R) \quad (6.5)$$

where  $b_n(Z, R)$  is a function of the current density in the coil and the distance between the source point  $z_0$  and the point  $(Z, R)$  in the coil body.

The series shown above converge only for  $\rho < \rho_{cen}$ , thus  $P$  has to be inside a convergence circle with a radius  $\rho_{cen}$  around  $z_0$ . The series converge faster for points closer to the sourcepoints (smaller  $\frac{\rho}{\rho_{cen}}$ ), therefore the computation time is lower as well. Hence, the calculation of more source points can speed up the computation of the magnetic field and allows the calculations of the magnetic field a larger area. For ratios up to

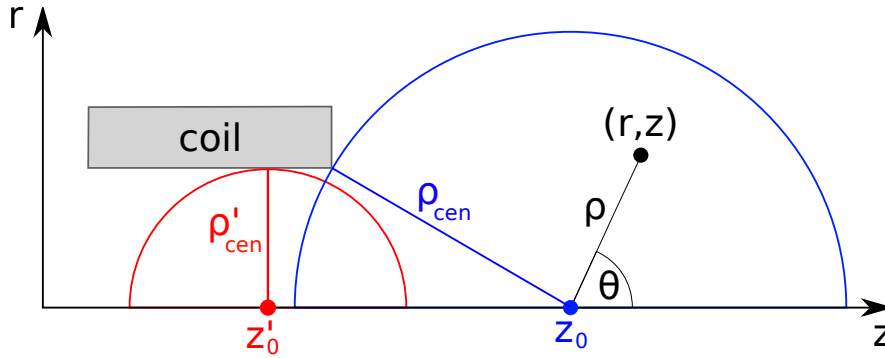


**Figure 6.2:** The convergence circles with radii  $\rho_{cen}$  and  $\rho'_{cen}$  for two different source points  $z_0$  and  $z'_0$ . Using more source points leads to a better coverage of the area and a faster computation of the magnetic field.

$\frac{\rho}{\rho_{cen}} \leq 0.99$  the Legendre polynomials provide a faster calculation than the elliptic integral method.

For the KATRIN experiment, a code named *magfield* was created by Dr. Ferenc Glück based on the Legendre polynomial expansion explained above. The program calculates the source coefficients  $B_n^{cen}$  for specified source points and writes them to the file `magsource.dat`. The magnetic field can then be calculated with routines using eq. 6.2 - 6.4. In the case that for a given point  $\frac{\rho}{\rho_{cen}} > 0.99$ , the field for this point is calculated with elliptic integrals. Two versions of this code exist for different geometric situations.

- The program *magfield2* is suited for setups with exactly one symmetry axis, e.g. the  $z$ -axis. This is the case for an idealised KATRIN spectrometer section where all magnets are aligned perfectly along the  $z$ -axis. The influence of the tilted magnets of the transport section is negligible at the main spectrometer, hence *magfield2* was used for the simulations in this thesis. As input the program needs the position and dimensions of the coils and the coil current. These parameters are stored in a file called `inputcoil.dat`.
- For setups with more than one symmetry axis, the program *magfield3* is used. For the KATRIN setup is needed to calculate the magnetic fields of the the tilted coils of the transport section or coils which are not perfectly aligned, e.g. to calculate the impact on the fluxtube.

## 6.1.2 Electric field calculations

### Boundary element method

Commercial programs<sup>1</sup> to calculate electric fields were tested for the KATRIN setup [Val04], but none of them turned out to be suitable. The problem is based on the different size scales needed: Inside the huge 23 m long vessel of the main spectrometer, wires are located with tiny diameters 0.2 mm or 0.3 mm. Programs based on the *finite difference method* (FDM), like *SIMION*, divide the volume by an equidistant grid and

<sup>1</sup>Common programs are e.g. *CPO* [CPO] or *SIMION* [SIMION].

then calculate the electric fields based on this grid. Therefore a very close-meshed grid is needed to account for the wires in the simulations. The huge size of the spectrometer then leads to massive memory problems.

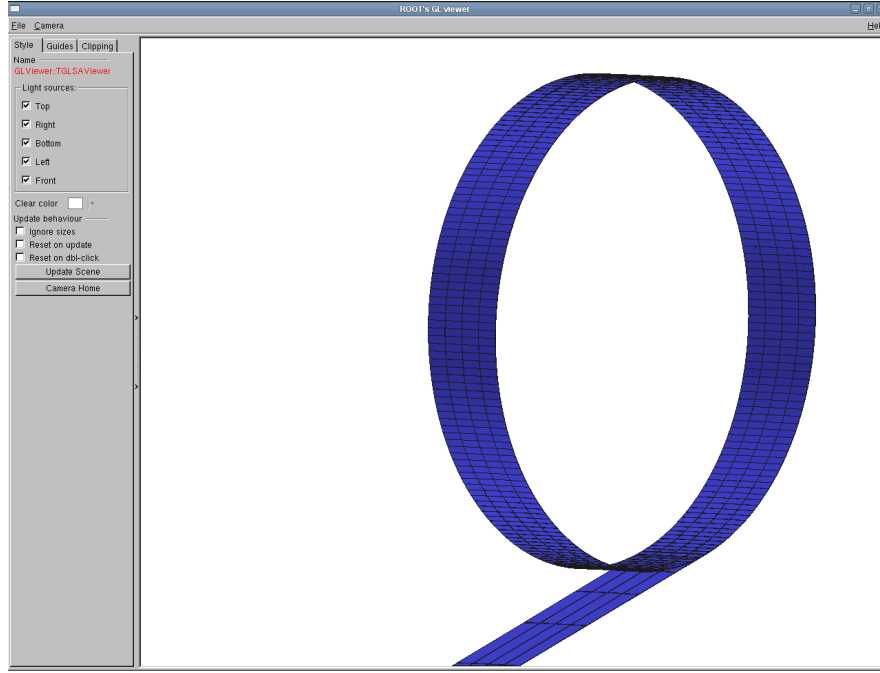


**Figure 6.3:** Example of electrode discretisation viewed with *ROOTsim* (see section 6.1.4). Shown is a cut in the  $\phi$  plane of the ground electrode inner endbulge.

Therefore, the electric fields for the KATRIN main spectrometer are calculated by using the *boundary element method* (BEM). It is based on the division of the electrodes  $I$  into (small) surface elements  $i$ , which are assumed to have a constant charge density<sup>2</sup> on a given electrode (see figure 6.3). For every surface element  $i$  generated this way, the potential  $U_i$  has to equal the applied electrode potential  $U_I$ , as the surfaces of electric conductors are equipotential surfaces. The potential  $U_i$  in the centre<sup>3</sup> of element  $i$  can be expressed as the sum of the potential contribution  $\Phi_{ij}$  of all other surface elements  $j$  to the element  $i$ :

$$U_i = \sum_j \Phi_{ij}. \quad (6.6)$$

The contribution  $\Phi_{ij}$  from element  $j$  to the potential  $U_i$  at element  $i$  is given by

$$\Phi_{ij} = \frac{1}{4\pi\epsilon_0} \int d^2r_j \sigma_j \frac{1}{|\vec{r}_i - \vec{r}_j|} \quad (6.7)$$

$$= \frac{\sigma_j}{4\pi\epsilon_0} \int d^2r_j \frac{1}{|\vec{r}_i - \vec{r}_j|} \quad (6.8)$$

$$\equiv \sigma_j k_{ij} \quad (6.9)$$

<sup>2</sup>This ansatz is allowed as the charge density is continuous.

<sup>3</sup>The approximation that the potential contribution is summed up only for the centre of an element  $i$  is allowed if the elements are small enough.

where  $\sigma_j$  denotes the surface charge density of the surface element  $j$ . It is integrated over the complete surface with the constant charge  $\sigma_j$  of element  $j$ . The factor  $k_{ij}$  just depends on the (known) electrode geometry. Using eq. 6.9, one can express eq. 6.6 as a linear system of equations:

$$K\vec{\sigma} = \vec{U}, \quad (6.10)$$

with  $K$  denoting a matrix built of the  $k_{ij}$  describing the geometry.  $\vec{U}$  is given by the applied electrode potentials. Hence, this system can be solved and  $\vec{\sigma}$ , describing the surface charge densities of all elements, can be calculated.

From that the electric potential at a point  $\vec{r}$  can be calculated by summation over all the electrode elements  $l$ :

$$U(\vec{r}) = \frac{1}{4\pi\epsilon_0} \sum_l \sigma_l \int d^2r_l \frac{1}{|\vec{r} - \vec{r}_l|} \quad (6.11)$$

The electric field for an arbitrary point then follows by numerical differentiation.

Apparently, the combination of large and small scale structures does not state a problem for the BEM. It is therefore well suited for the calculations of the electric properties of the main spectrometer.

Nevertheless, the BEM also has limitations: The number of elements  $N$  (corresponding to the discretisation) is limited by the memory size of the computer. The memory size needed rises approximately with  $N^2$ . With a memory size of 1 GB approximately  $N = 10^4$  elements can be calculated. Typical geometries used in the design simulations presented in this chapter consist of about 3000 elements.

### The elcd code

For the KATRIN experiment the *elcd* program code has been created by Dr. F. Glück based on the BEM discussed above to calculate the electric charge densities (for details see[Glu04]). Two different versions of the code exist.

- The *elcd3\_2* code is intended for configurations with full metal electrodes which are completely rotationally symmetric and wires with the z-axis as common symmetry axis. This is not sufficient for detailed simulation of the wire electrodes of the main spectrometer because the combs of the wire module do not match this symmetry.
- The *elcd3\_3* code supports electrodes with just partial rotational symmetry. Electrodes are divided into rectangular elements which can be rotated to form a partial symmetry to save computing time. This allows to include the comb structure of the wire electrode in the simulations. The use of rectangles on the other hand does not support the round structures of the spectrometer vessel and conical electrodes. These structures have to be approximated by rectangles.

The routine to calculate the surface charge densities with the BEM described above is called *elmmain*. The calculated surfaces charge densities are stored in file called `element.dat`. Electric fields can be calculated with the *scan* routine.

### 6.1.3 Calculations including magnetic and electric components

Additional programs exist which use parts of the *elcd* and the *magfield* code:

- The *fieldlinepot* program calculates the electric potential along the path of a magnetic field line. For the calculation of the magnetic field lines a Runge-Kutta algorithm is used based. *Fieldlinepot* can be utilised to search for particle traps along the field lines.
- The *transmission* program allows to calculate the longitudinal energy of electrons along paths at the edge of the fluxtube. This is done under the assumption of adiabatic energy transformation, the principle of the MAC-E filter. In the simulations this program is used e.g. to search for too early retardation.

### 6.1.4 Geometry creation

For the *elcd* code a discretised geometry is needed as input. Because of the large number of electrode elements resulting from the discretisation, the form of such an input file (*geometry.dat*) is complicated<sup>4</sup>. As many different geometry files have to be created in the electromagnetic design process, a program is needed to create these files in a convenient way.

The *MainSpec* program was created by S. Vöcking for this purpose [Voe08]. It is written in Python (an object oriented, interpreted programming language, see [Pyt]) with a graphical user interface (GUI). Additionally, the geometries can be viewed in 3D using *ROOTsim*, a program based on *ROOT*'s OpenGL viewer ([ROOT]) (see also figure 6.3).

With the GUI all parameters of the geometry (e.g. potentials, electrode positions) can be viewed and changed easily. Geometries can be stored as *xml* files so they can be loaded into the program at a later time.

During the electromagnetic design process the requirements for the *MainSpec* program changed. New parameters became important while others were fixed and should not be modified any more. Hence, the program was adapted to the new needs.

One added feature is the so called *cmdMainSpec* code which is divided into two parts.

- One part is also written in Python and accesses the classes of the *MainSpec* program which are used to actually create the geometry. Thus, every change in the *MainSpec* code is directly implemented in *cmdMainSpec* as well which is important for consistency.
- The interface for *cmdMainSpec* is no GUI but a script based interface which allows to create many geometries in a sequence. This can be used to scan one or more<sup>5</sup> parameters in given ranges. The base geometry is loaded from a *xml* file previously created with *MainSpec*, the given parameters are then applied appropriately to this geometry.

<sup>4</sup>A typical geometry file consists of 3000 rows with 16 columns each.

<sup>5</sup>In principle the number of parameters is not limited by the script framework, but a change of more than two parameters at once was not needed up to now.

A typical application of scanning one parameter is the variation of an electrode potential. A two parameter scan can be used e.g. to optimise electrode positions, using the  $r$  and  $z$  coordinates as parameters.

### 6.1.5 Overview

An overview of the programs described above is given in figure 6.4. The following list describes the elements of a typical simulation workflow.

Typically all these simulations are done on the local cluster to save calculation time and to avoid the inconsistencies of the data which could be caused e.g. by different operating systems (64 bit, [32]bit).

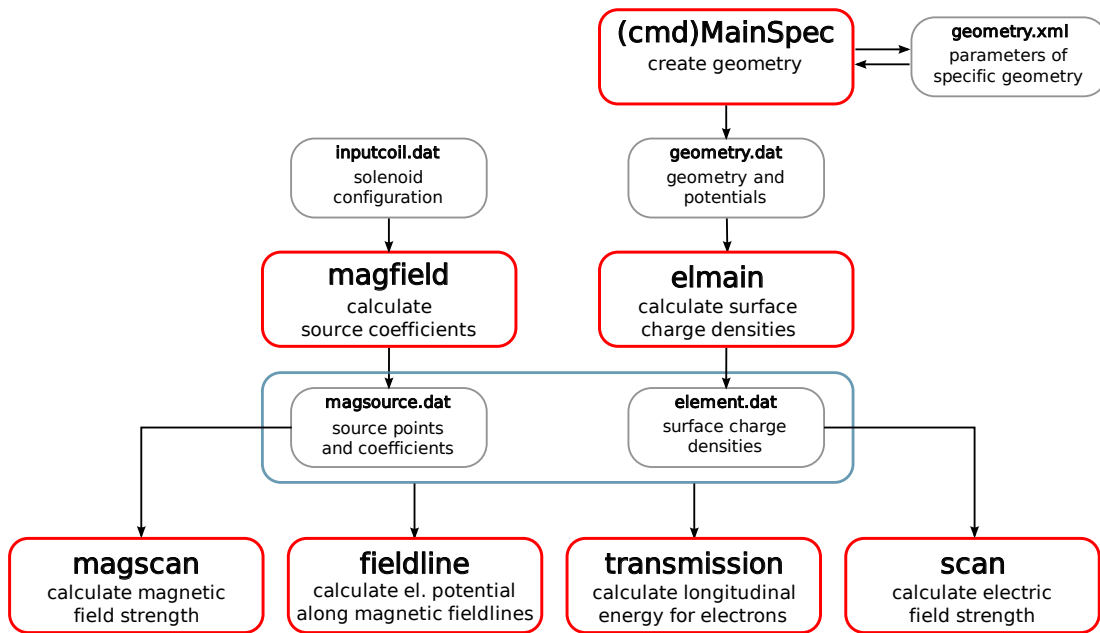


**Figure 6.4:** Scheme of the simulation tools (not comprehensive). The red boxes mark programs, the grey boxes represent input/output files. The fieldline and transmission code needs the *element.dat* and the *magsource.dat* as input files.

- The *magsource.dat* file calculated by the *magfield* program does not need to be calculated for every simulation with a new electrode geometry. From the *magsource.dat* file, the magnetic field at a given point can be calculated by use of the *magscan* routine.
- The geometry creation can be done either by direct use of *MainSpec* or via the *cmdMainSpec* script-based interface.
- The *elmain* routine calculates the surface charge densities using the *geometry.dat* file created in the last step. From the resulting *element.dat* file, the electric field at a given point can be calculated by using the *scan* routine.

- The *fieldline* and *transmission* programs can be employed to calculate the electric potential along the magnetic field lines and the transmission properties.

## 6.2 Optimisation of the electrode design

The final electrode design has to meet several requirements to comply with the background and transmission criteria of the KATRIN experiment. These topics were already discussed in chapters 3 and 4. Nevertheless they are mentioned here again to give an overview of the many topics which have to be accounted for in the design of the electrode system.

- The designated magnetic flux tube equivalent to  $191 \text{ Tcm}^2$  (see [KAT04]) has to pass through the spectrometer with a given safety margin.
- The transmission properties must prevent too early retardation.
- The potential depression along the analysing plane has to be as small as possible.
- In order to avoid field emission, the electric field strength has to be kept below  $1 \text{ MV/m}$ , especially at cathode parts like the shielding electrode.
- Penning traps have to be avoided or their depth has to be kept below  $e\Delta U \approx 15.4 \text{ eV}$ , the ionisation energy of  $H_2$
- Particle traps caused by bumps in the longitudinal energy along the spectrometer have to be avoided.
- The construction and installation of the electrode must be feasible.

As the space in the steep cone region is very limited (see figure 6.5), a trade-off between the different goals described above had to be found with the design of the electrode system.

At the beginning of the analysis described in this chapter, the design process for the cylinder part and the flat cone part was largely finished. A discussion of the general layout of the electrode can be found in [Val04]. Many details of the electrode design were already discussed in [Hug08]. An additional electrode (the so called shielding electrode) to suppress deep Penning traps in the flange region has been introduced there. More information on the electromagnetic properties can be found in [Val09].

Based on these results, a systematic search for the best parameters of the steep cone electrodes and possible additional problems has been performed in the course of this thesis.

For the simulations the mirror symmetry of the spectrometer at the  $z = 0$  plane is used. The magnetic fields are not symmetrical to this plane. Both magnetic field settings at the detector magnet ( $B_{\text{det}} = 3.5 \text{ T}$  or  $B_{\text{det}} = 6 \text{ T}$ , see section 5.1.5) have to be taken into account. As the influence of the detector magnet is negligible on the source side of the spectrometer, three different situations have to be simulated: The detector side with both detector magnet settings and the source side with one (arbitrary) detector magnet setting.

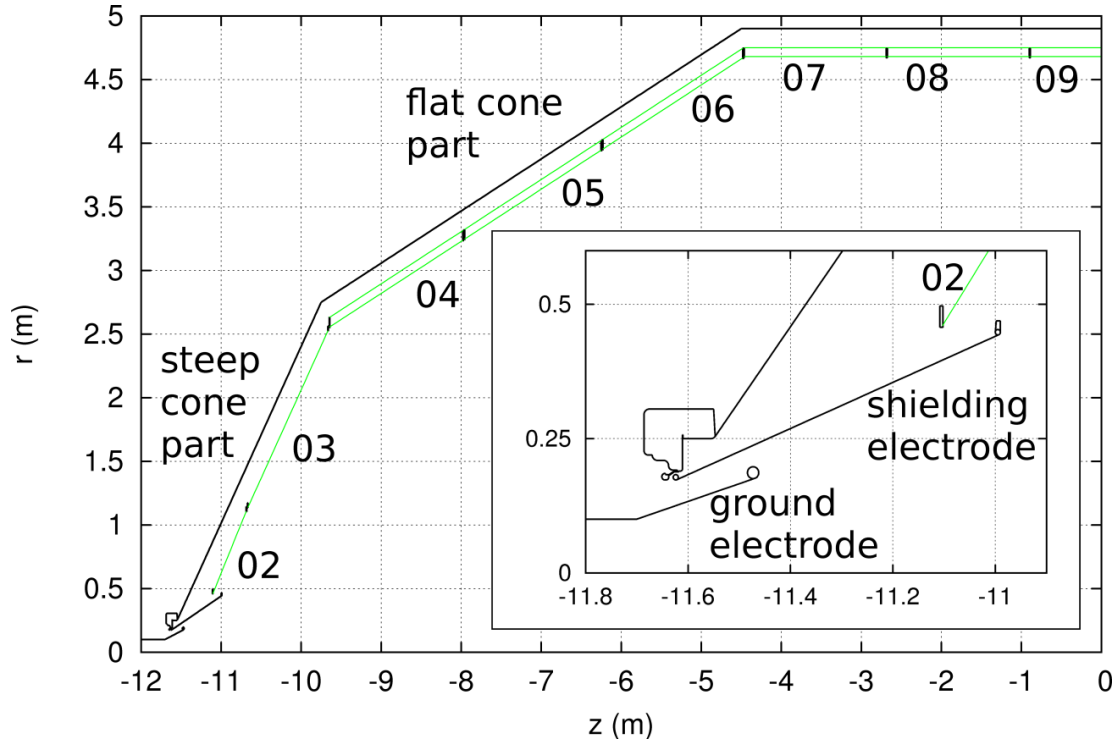


**Figure 6.5:** Overview of the steep cone and flange region. The numbers denote the electrode rings. While the modules of the flat cone (rings 04, 05, 06 and their counterparts) and the cylindrical part (07 - 12) feature a dual layer wire electrode, while the steep cone modules (ring 02, 03 and their counterparts) consist of a single wire layer. The shielding electrode and the ground electrode are full metal electrodes.

The uncertainty of the simulated trap depth is about 1 V. It results primary from the fact that the trap depth is determined by the electric potential along a magnetic field line. The calculated magnetic field line has to “hit” the position of the maximum trap depth precisely. This leads to the need to compute a dense net of field lines which increases computation time.

The inner electrode system is symmetrical to the analysing plane. For an easier orientation, the electrode module rings will always be named as if they would be on the source section (02, 03,...) in this chapter.

In the following sections the optimisations done at several parts of the electrodes will be discussed in detail. The process is structured as follows:

- *Shielding electrode end bulge design:* The design of the shielding electrode end bulges was changed on both ends to fulfil both mechanical and electromagnetic design requirements.
- *Ground electrode:* The ground electrode can be adapted to the fluxtube to obtain lower field strength in the flange region. This can only be done while keeping a safety gap to the fluxtube. Additionally, sufficient transmission properties have to be assured.

- *Relative positioning of shielding electrode and ring 02:* As a Penning trap is located at the end of the shielding electrode, the influence of the ring 02 electrode position on this trap was investigated.
- *Absolute positioning of the shielding electrode/ring 02 system:* After fixing the relative positions of ring 02 and the shielding electrode, the absolute position of the shielding electrode/ring 02 system was optimised.
- *Shielding electrode modifications:* As an additional Penning trap was discovered at ring 02, modifications of the shielding electrode and the ring 02 potential were needed.
- *Comb potentials:* The potential applied to the combs of the wire electrode modules for background suppression was optimised for ring 02 and ring 03<sup>6</sup>.

### 6.2.1 Shielding electrode design and mechanical realisation

To suppress high electric field strengths, the ends of the full metal electrodes must be rounded. For the two ends of the shielding electrode two different solutions have to be applied.

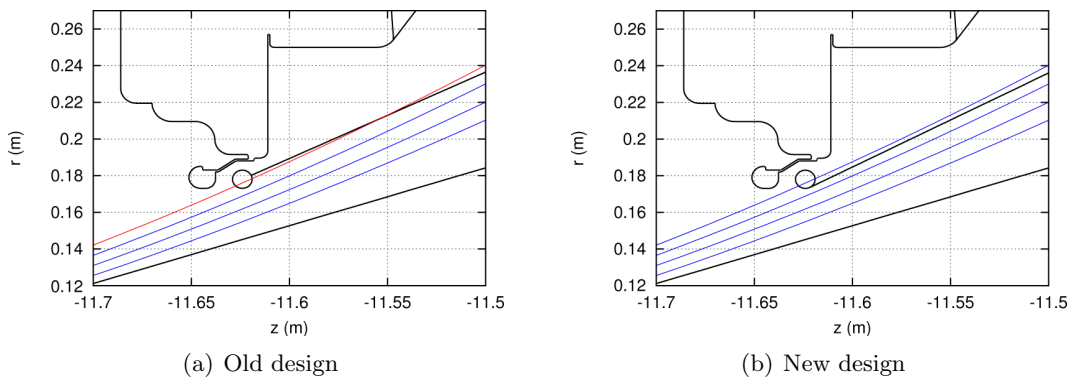


**Figure 6.6:** Two different designs of the outer end of the shielding electrode. The old design shown in (a) hosts a Penning trap at field lines cross the electrode twice (field line marked in red). The new design shown in (b) does not allow this type of field lines, hence no trap can develop at this position.

At the outer endpoint of the shielding electrode, a setup as shown in figure 6.6(a) was planned. There are magnetic field lines crossing the electrode twice, inbetween passing an area with a more positive potential induced by the ground electrode. This gives rise to a deep ( $\Delta U > 150$  V) Penning trap. As there are no informations whether a trap of such small dimensions will give rise to background effects, it should be avoided. By using a setup proposed as a possible solution in [Hug08] (see 6.6(b)), field lines cannot cross the electrode twice any more, thus eliminating this trap location.

<sup>6</sup>Actually, as described in section 5.2, the combs in the steep cone are formed as rings as they do not need teeth for a second wire layer. Nevertheless they are called combs to avoid ambiguousness with the module rings (e.g. module ring 02).

As will be discussed later, the shielding electrode inner endpoint (the one facing the spectrometer centre) will exceed the flange radius. The electrode needs to be mountable through the flange without the need to remove the wire electrodes. This is because the installation of the wire electrodes will possibly start before the mechanical implementation of the shielding electrode is finished. To allow for an installation from the outside, the electrode has to be segmented in an outer part which fits through the flange as a whole and an inner part. This inner part is planned as a thin metal sheet which can be rolled-up to fit through the flange and then is unfolded inside the spectrometer. A possible realisation of such a setup is shown in figure A.2.

A metal ring is planned as endpoint geometry at the inner endpoint of the shielding electrode. It provides mechanical stability for the metal sheet and assures the roundness and the centred position of the electrode, The ring can be separated to simplify the installation process. This ring has no significant impact on the electromagnetic properties of the shielding electrode compared to the previously planned end bulge.

The mechanical realisation of such a setup is complicated. A mockup is currently under construction to test the feasibility of the planned setup. Special attention has to be given to the joint of the inner and outer electrode parts. The electric field strength at this position was calculated to be of the order 1 GV/m for a smooth surface. Thus, a very smooth transition between the two parts is needed not to heighten the electric field strength any more.

The experience with this mockup has to be analysed and discussed with the engineers to find a solution which is practicable, but also complies with the demands from the electromagnetic design.

## 6.2.2 Ground electrode

In the design process of the ground electrode it is important to consider the resulting electric field strengths as well as to ensure good transmission properties.

To reduce the electric field strength the ground electrode has to be mounted with a maximum distance to the shielding electrode and the flange. A safety gap to the intended fluxtube of 191 Tcm<sup>2</sup> (see figure 6.7) has to be maintained. As the fluxtube is closest to the ground electrode at the source side the optimisations were accomplished for this position. The detector side is also noncritical then.

The safety gap is given by the cyclotron radius  $r_{\text{cycl}}$  in that region, the tolerance needed for the mechanical setup and the uncertainty of the fluxtube due to the unideal alignment of the magnets.

The cyclotron radius was derived to be

$$r_{\text{cycl}} = \frac{\sqrt{2m_e E_{\perp}}}{eB} \quad (6.12)$$

in section 4.2 (eq. 4.7). Here  $m_e$  denotes the mass of the electron with the charge  $e$ ,  $B$  the magnetic field and  $E_{\perp}$  the kinetic energy of the particle in the cyclotron motion perpendicular to the magnetic field. All these values can be obtained with the set of simulation tools at hand. In the high magnetic field region of the ground electrode kink ( $B \approx 0.7$  T), the cyclotron radius for an electron at the edge of the fluxtube is  $r_{\text{cycl}} \approx 0.2$  mm. This radius increases to  $r_{\text{cycl}} \approx 0.4$  mm for electrons in the vicinity

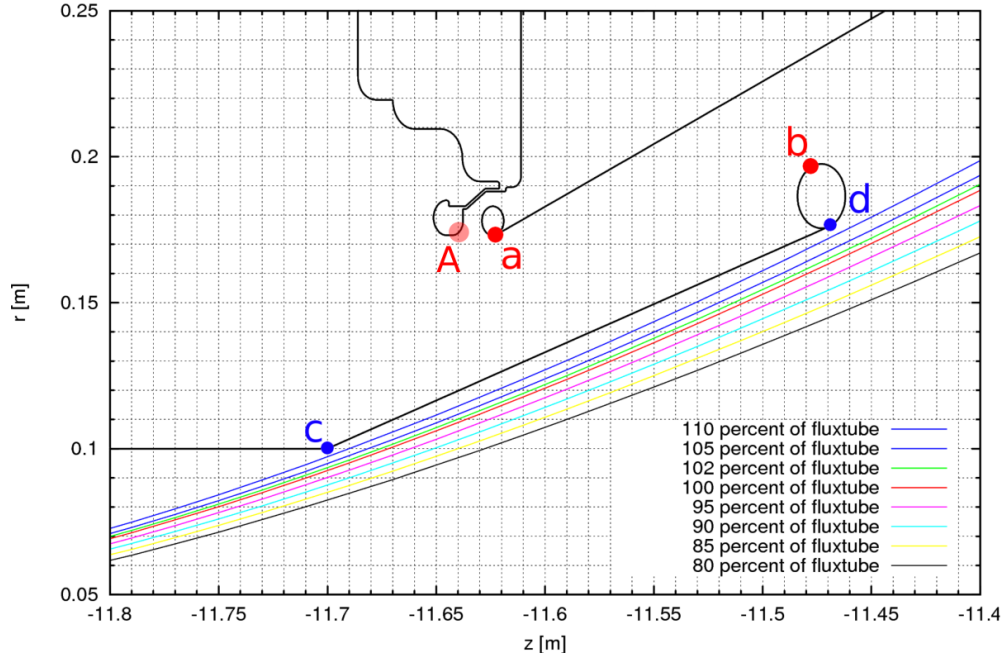


**Figure 6.7:** The fluxtube in the source region. The optimised ground electrode retains a distance of about 5mm to the 191 Tcm<sup>2</sup> fluxtube (100% fluxtube).

At the red marked positions the maximum field strength are located: point *a* and *A* at the shielding electrode and flange (cathode), point *b* at the ground electrode (anode). Point *c* marks the position of the ground electrode kink, *d* marks the inner endpoint of the ground electrode.

of the ground electrode end bulge and  $r_{\text{cycl}} \approx 0.9$  mm in the region of the shielding electrode inner end ring, where the magnetic field drops to about  $B \approx 0.05$  T.

The mechanical tolerance has to be divided into two parts:

- The out-of-roundness for an electrode with the dimensions of the ground electrode or shielding electrode can be severe. It also depends on the mounting structure and the shape of the electrode end as well as on the electrode material. For the ground electrode it was estimated to approximately  $\pm 1.5$  mm.
- The adjustment of the electrode position is challenging as both electrodes have to be mounted from the outside and therefore are difficult to access. This adds another uncertainty of about  $\pm 1.5$  mm to the mounting accuracy.

The uncertainty of the fluxtube due to the alignment of the magnets has not been calculated up to now. It was chosen to maintain a safety gap of  $d_{\text{gap}} > 5$  mm to the fluxtube for the proposed setups until these calculations have been done.

The maximum field strength at cathode potential is located at the outer bulge of the shielding electrode (see point *a* in figure 6.7). The field strength here depends on the distance to the ground electrode (and on the geometry of the shielding electrode, see section 6.2.4).

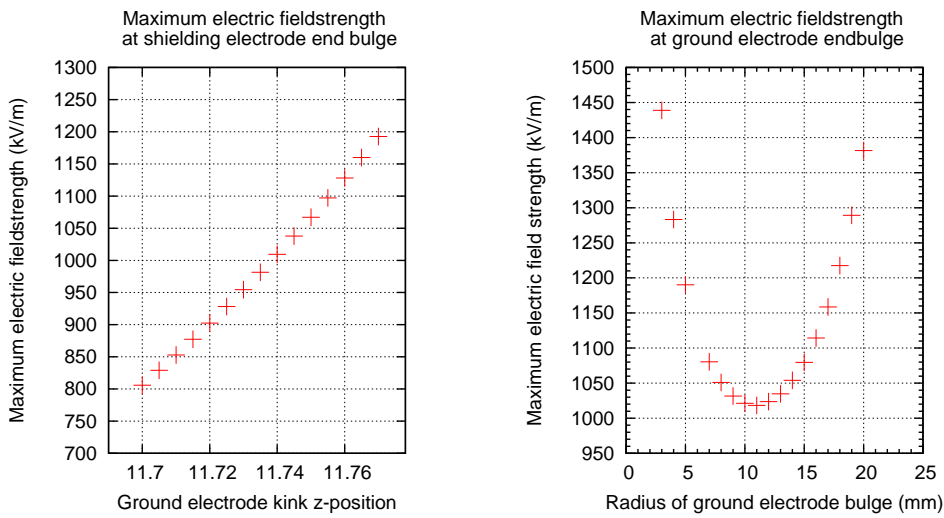
The maximum field strength at the ground electrode (anode) is located at the end bulge (marked *b* in figure 6.7). It depends on the distance to the shielding electrode as well

as on the bulge radius.

### Kink position

The dependence of the field strength at the shielding electrode end bulge (position  $a$  in figure 6.7) on the  $z$ -position of the ground electrode kink (position  $c$  in figure 6.7) can be seen in figure 6.8(a).

The  $z$ -position of the kink was shifted closer to the fluxtube ( $z_{\text{kink}} = -11.70$  m), maintaining a distance of  $\approx 7$  mm between ground electrode and fluxtube. Thereby an improvement of the maximum field strength at the shielding electrode end bulge of  $> 300$  kV/m compared to an earlier proposed setup with a distance of 30 mm to the fluxtube ( $z_{\text{kink}} = -11.76$  m) was gained.



(a) The maximum field strength at the shielding electrode end bulge depending on the ground electrode kink  $z$ -position

(b) The maximum field strength at the ground electrode end bulge depending on the radius of the ground electrode end bulge.

**Figure 6.8:** Maximum electric field strengths depending on different ground electrode parameters.

### Endpoint position

The inner, tilted part of the ground electrode (the electrode part ranging from  $c$  to  $d$  in figure 6.7) was elongated<sup>7</sup> for two reasons:

- The shielding electrode has a larger angle than the ground electrode. Hence, the distance between them will be larger for a longer ground electrode, resulting in a lower electric field strength.

<sup>7</sup>That means the endpoint was shifted to the middle of the spectrometer while keeping the electrode angle constant.

- A longer electrode provides better transmission properties. For a shorter ground electrode a bump in the longitudinal energy develops (cf. figure 6.9) which indicates a possible particle trap as explained in section 4.5. This is already the case for an electrode 10% ( $\approx 23$  mm) shorter than the chosen setup. For even shorter electrodes the depth of this bump increases.

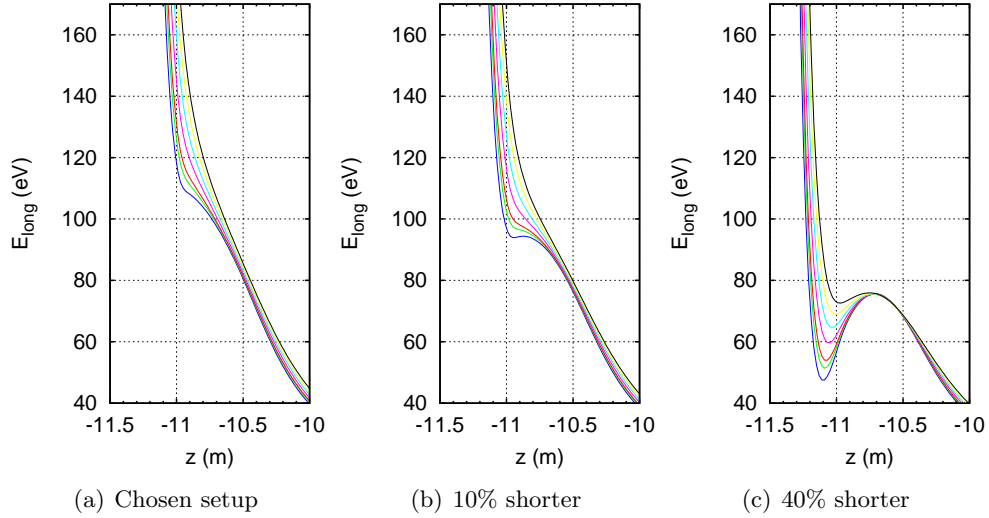


**Figure 6.9:** The longitudinal energy  $E_{\parallel}$  of electrons at the edge of the fluxtube (compare figure 6.7) for the flange region. The electrons are assumed to start in the centre of the main spectrometer entrance magnet with a kinetic energy just sufficient to reach the analysing plane.  $E_{\parallel}$  drops fast due to the rising electric potential. a) The chosen setup with an electrode endpoint of  $z_{GE,endpoint} = 11.46955$  m,  $r_{GE,endpoint} = 0.17605$  m b) Results for a setup with an electrode 10% shorter. The bump begins to show. c) A deep bump corresponding to a trap depth of about 20 V for 100% fluxtube (red) for an electrode 40% shorter.

But there are also negative aspects of a longer ground electrode:

- Most critical is the influence of the ground electrode potential on the Penning trap at the inner end of the shielding electrode (see section 6.2.4): The ground potential induces this Penning trap which becomes deeper as the ground electrode endpoint is drawn nearer to the trap position.
- A long electrode with a diameter exceeding the flange radius and the outer radius of the shielding electrode radius complicates the mounting procedure of both electrodes.

Therefore, a compromise was chosen for the ground electrode length with an endpoint of  $z_{GE,endpoint} = 11.46955$  m<sup>8</sup>.

<sup>8</sup>A mechanical precision in the 0.01 mm scale is neither possible for the mechanical mounting nor is it covered by the geometry model used in the simulations. The last digit of this values results from the need to get straight numbers, especially for the angles, in the CAD models.

The radius of the inner endpoint of the ground electrode (marked  $d$  in figure 6.7) was reduced compared to former setups to reach lower electric field strength at the ground electrode end bulge. This parameter has a big influence on the maximum field strength. The maximum field strength at the ground electrode endbulge depending on the radius of the endpoint is shown in figure 6.10(b). For larger radii  $r_{GE,endpoint} > 0.2$  m the field strength rises rapidly, as the end bulge gets very close to the shielding electrode. The ground electrode end bulge overlaps with the shielding electrode for  $r_{GE,endpoint} \gtrsim 0.215$  m.

The maximum field strength at the shielding electrode depending on the radius of the ground electrode endpoint radius is shown in figure 6.10(a). For smaller endpoint radii  $r_{GE,endpoint} < 0.17$  mm the maximum cathode field strength is not located at the shielding electrode outer endpoint, but at the flange (marked  $A$  in figure 6.7). For larger radii the maximum field strength is located at the shielding electrode end bulge again and continues to rise slowly. For radii  $r_{GE,endpoint} \geq 0.195$  mm the maximum field strength at the shielding electrode is located at around  $z = 11.48$  m, thus at the point where the ground electrode bulge approaches the shielding electrode. From that point it rises as rapidly as does the corresponding field strength at the ground electrode end bulge.

The chosen end point of  $r_{GE,endpoint} = 0.17605$  m retains a safety gap of  $d_{gap} \approx 14$  mm to the fluxtube as this end of the electrode is harder to adjust as the kink position.

The influence of the ground electrode endpoint radius for a given  $z$  position on the transmission properties is small.

### End bulge radius

The radius of the ground electrode end bulge was optimised while keeping the inner endpoint of the ground electrode (marked  $d$  in figure 6.7) fixed. The results are shown in figure 6.8(b).

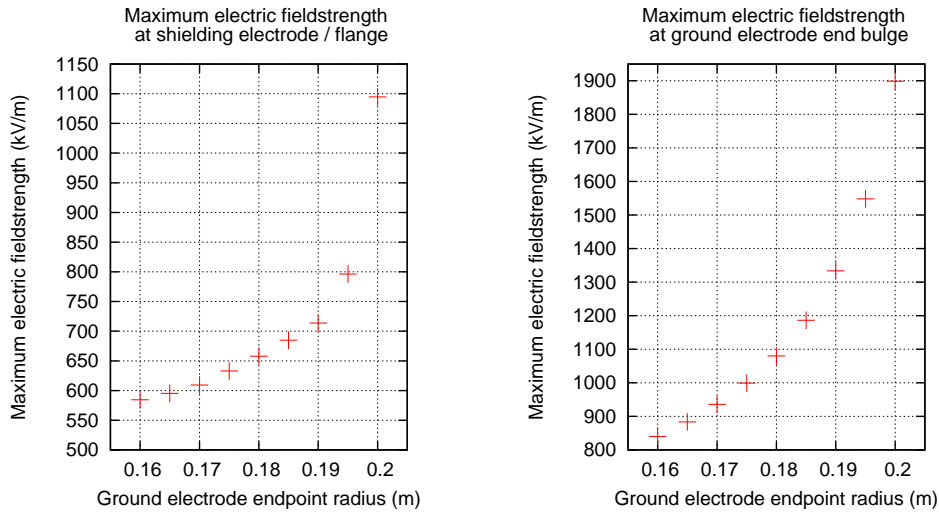
For smaller radii, the gap to the shielding electrode increases, but the field strength increases due to the higher curvature of the ring. At larger radii, the gap to the shielding electrode gets too small and the field strength rises fast. At a radius of  $R_{bulge} = 11$  mm the minimum field strength is achieved.

### 6.2.3 Relative placement of ring 02 and the shielding electrode

The mounting positions of ring 03 and the junction of rings 02 and 03 were already fixed at the beginning of this thesis. The residual ring 02 endpoint can be used as optimisation parameter.

Its position is strongly connected to the placement of the shielding electrode endpoint because of the influence of their respective electric fields. Therefore it is reasonable to first fix their relative positions and then in a next step optimise the absolute position of the fixed shielding electrode / ring 02 system.

The main topics for the relative positioning are the depth of the Penning trap at the inner end of the shielding electrode (see figure 6.11) and the transmission properties.



(a) The maximum field strength at the shielding electrode end bulge / flange (see text) depending on the ground electrode endpoint radius.

(b) The maximum field strength at the ground electrode end bulge depending on the ground electrode endpoint radius.

**Figure 6.10:** *Maximum electric field strength depending on the ground electrode endpoint radius.*

**Penning trap** As mentioned before this trap is partially induced by the more positive potential of the ground electrode. Hence, the trap depth shows a strong dependence on the distance between shielding electrode endpoint and ground electrode endpoint. This dependency will be covered in the next section.

The trap depth also depends both on the position and on the potential applied to the ring 02. A more negative potential attenuates the influence of the high ground electrode potential, thus making the trap more shallow. The simulations described in this section were done with a potential of  $U_{02} = 18500$  V and  $U_{SE} = U_{vessel} = 18400$  V.

Figure 6.12(a) shows the Penning trap depth depending on the position of the ring 02 endpoint relative to the fixed end of the shielding electrode. The depth mainly depends on the gap between the electrode ends, which can be seen as a ring structure in the trap depth in figure 6.12(a).

**Transmission properties** When analysing the transmission properties, it is expedient to follow one “ring” of constant trap depth to see how the transmission changes (cf. figure 6.12(b)). Following such a ring from the inside to the outside of the spectrometer a significant improvement of the transmission can be found at the point when the 02 ring is hidden behind the shielding electrode. Extending the ring 02 further behind the shielding electrode do not change the transmission properties significantly any more. This is explained by the fact that, although the ring 02 electrode has a higher (negative) electric potential, the parts behind the shielding electrode cannot influence the transmission any more.

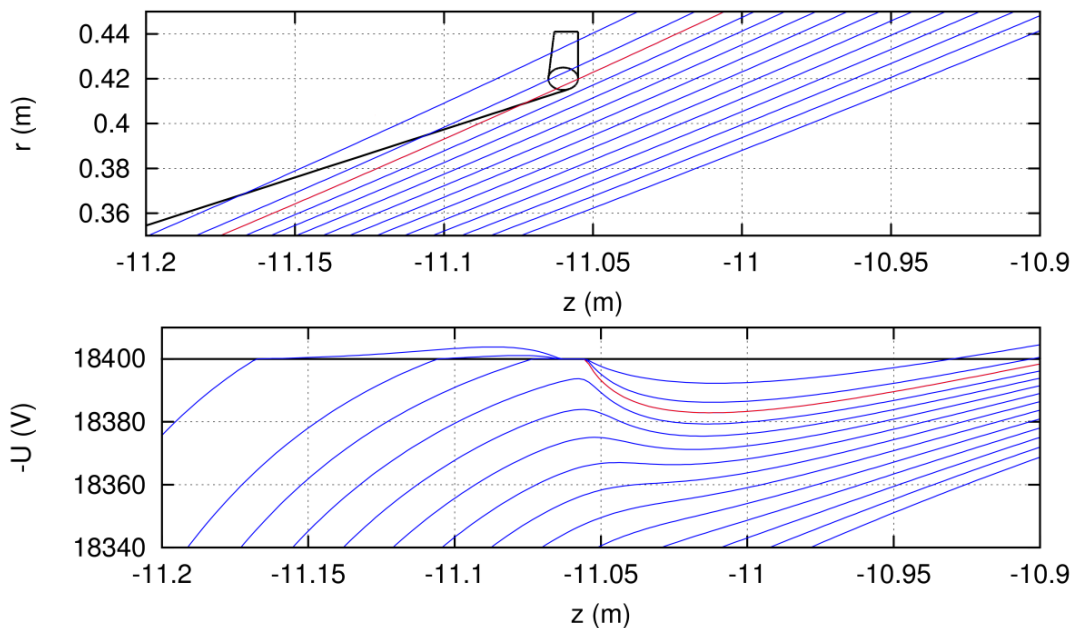
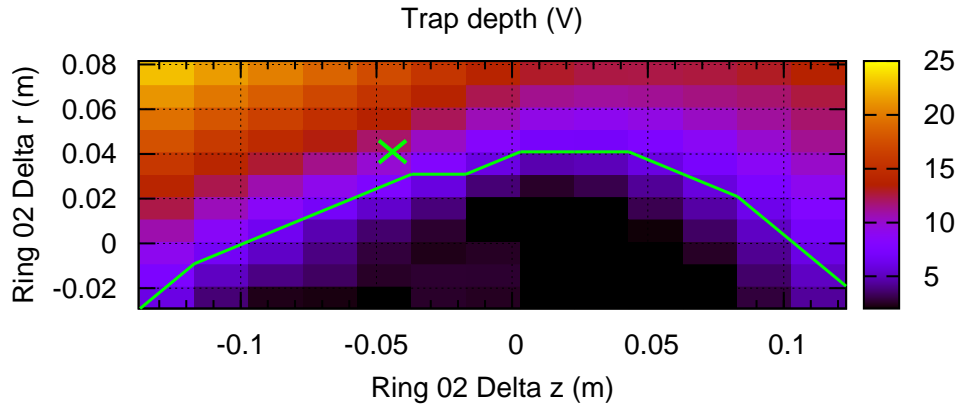


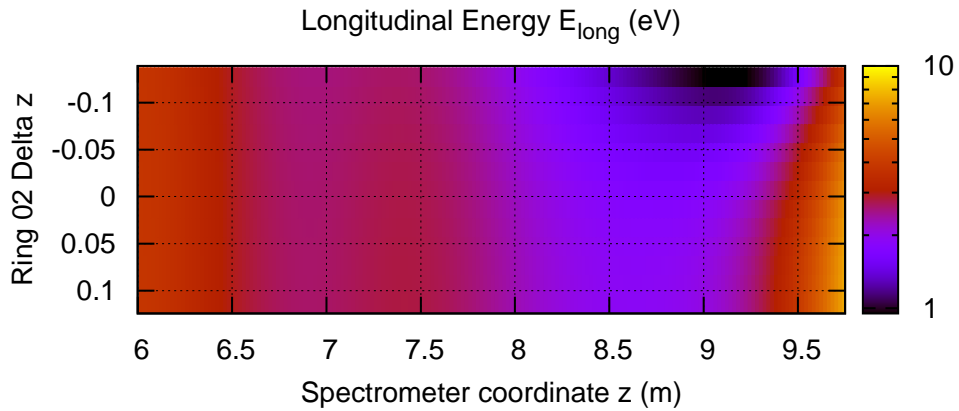
**Figure 6.11:** *The Penning trap at the end of the shielding electrode. Shown at the top is the geometric course of the magnetic field lines. At the bottom the electric potential along the same field lines is shown. The depth of the trap shown here is  $\Delta U \gtrsim 20$  V.*

**Conclusion** For the installation of the electrodes it is convenient to keep a gap between the electrodes large enough to be able to mount both electrodes without the risk of touching each other. Hence a preliminary<sup>9</sup> relative position of  $\Delta r = 0.041$  m and  $\Delta z = -0.044$  m between the shielding electrode end bulge centre and the ring 02 endpoint was chosen as marked in figure 6.12.

<sup>9</sup>Due to a Penning trap discovered at module ring 02, additional changes to the relative placement of the shielding electrode and the ring 02 endpoint were needed, see section 6.2.5).



(a) The depth of the Penning trap at the end of the shielding electrode (source side) depending on the relative position of the ring 02 endpoint and the shielding electrode end bulge centre. A positive  $\Delta z$  value means the ring 02 endpoint is located in the direction of the flange relative to the shielding electrode endpoint. The trap depth depends mostly on the gap between ring 02 and the shielding electrode, as can be seen in the ring structure of the plot. The green line marks a line of approximately constant trap depth (see (b)). The chosen preliminary relative position is indicated by the green cross.



(b) The longitudinal energy  $E_{\parallel}$  for electrons at the edge of 100% fluxtube depending on the relative  $z$ -positions of the ring 02 endpoint and the shielding electrode end bulge centre (following the green line of approximately constant trapdepth shown in (a)). For  $\Delta z_{02} < -0.05$  m (ring 02 is not covered by the shielding electrode) a valley in the longitudinal energy can be found at  $z_{spec} \approx 9$  m. It is more prominent on the detector side with 6 T at the detector magnet, as shown in the plot. Note that a logarithmic scale was used for  $E_{\parallel}$  to better visualise the effect.

**Figure 6.12:** *The relative positioning of ring 02 endpoint to the shielding electrode.*

## 6.2.4 Absolute placement of the shielding electrode

The next step is to specify the position of the shielding electrode / ring 02 system. Thus, the inner endpoint of the shielding electrode is optimised, co-moving the ring 02 endpoint with the fixed relative positioning as explained in the last chapter.

Within a reasonable parameter range, the shape of the geometry of this system does not change significantly. Thus the results obtained in the last step hold true also for a changed position of the shielding electrode / ring 02 system.

For the optimisation, several limits have to be taken into account which will be discussed in the next paragraphs.

**Influence of the ground electrode** As already mentioned in section 6.2.2, the length of the shielding electrode is limited by the ground electrode potential: With a too short electrode, the ground potential gives rise to a Penning trap (see figure 6.11).

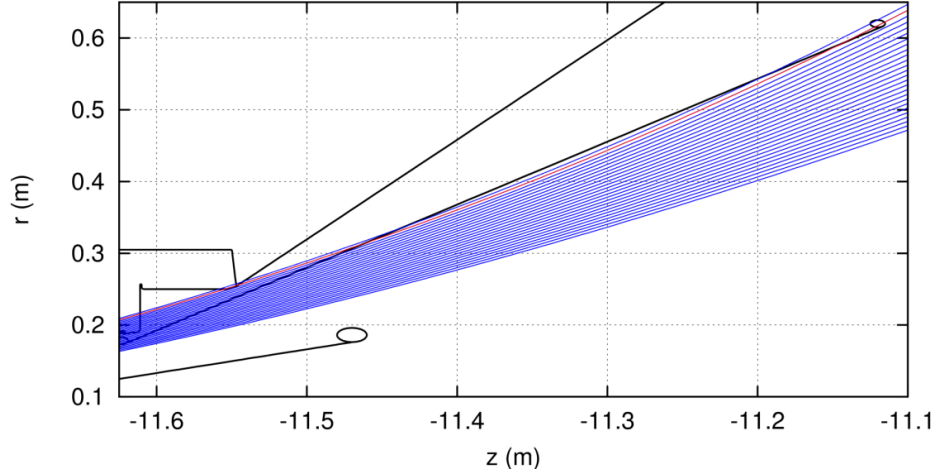
The depth of this trap depending on the shielding electrode endpoint position is shown in figure 6.14. Reducing the shielding electrode length leads to a fast growing Penning trap, while a longer shielding electrode can suppress the trap.

As stated in the last section, the absolute value of the trap depth also depends on the potential applied to ring 02. For more details of this correlation see section 6.2.5.

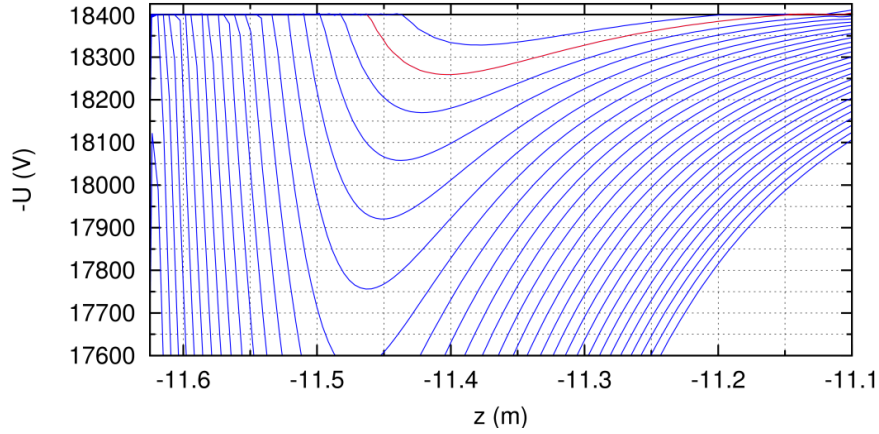
**Penning traps due to a too steep electrode** A higher radius of the shielding electrode endpoint leads to a steeper slope of the electrode. The electrode will then be cut by several field lines in a way that they emerge from the shielding electrode in the direction of the ground electrode and the spectrometer centre. Such a setup is shown in figure 6.13. Directly after leaving the shielding electrode the highly positive potential (with respect to the shielding electrode potential) from the ground electrode will cause a deep valley in the potential along these field lines. Following these field lines further, some will hit the shielding electrode again, forming a deep ( $> 100$  V) cathode-to-cathode Penning trap between the crossing points with the shielding electrode. Field lines that do not hit the shielding electrode again form an even deeper ( $> 1$  kV) cathode-to-vacuum trap. These traps have to be suppressed by choosing a smaller opening angle of the shielding electrode, thus suppressing these types of field lines.

**Electric fieldstrength** A smaller opening angle of the shielding electrode increases the field strength at the ground electrode bulge because the gap to the ground electrode decreases. Without the need for a smaller opening angle due to the Penning traps described in the last paragraph one would obtain a field strength as low as about 700 kV/m at the ground electrode. For a design with a smaller angle, without these traps kind of traps, the field strength rises by  $\approx 300$  kV/m.

The influence on the electric field strength at the outer end of the shielding electrode are different. Here the electrode angle does not have a strong impact on the gap between shielding and ground electrode, but the geometry changes slightly. For small angles, the position of the field strength maximum is located at the edge between the plain electrode and the bulge. As the opening angle of the shielding electrode increases, more of the end bulge curvature faces the ground electrode. The field strength maximum is then located on the curved part of the bulge and therefore is higher. The impact on



(a) For a too steep opening angle of the shielding electrode, field lines can cross it in a unfavourable angle, forming Penning traps.



(b) The resulting Penning trap has a depth of  $\Delta U > 100$  V for field lines hitting the electrode twice. Field lines not hitting the shielding electrode again show much deeper traps with  $\Delta U \gg 1$  kV.

**Figure 6.13:** *The Penning trap caused by a too steep angle of the shielding electrode. The field line forming the deepest cathode-to-cathode trap is marked in red.*

the field strength of this effect is with  $\approx 20$  kV/m much smaller than the previously discussed effects and also much smaller than the effects which have been achieved in this region by optimising the ground electrode (see section 6.2.2).

**Influence on the longitudinal energy** For smaller radii and a longer shielding electrode in  $z$  direction<sup>10</sup> the bump in the longitudinal energy  $E_{\parallel}$  at  $z_{spec} \approx 9$  m already mentioned in the previous section deepens, eventually reaching  $E_{long,min} = 0$ , which means reflection. This is explained by the fact that an electrode closer to the fluxtube has a higher impact on  $E_{\parallel}$ . By applying a slightly (a few 10 V, see below) more positive

<sup>10</sup>Using the parameter range shown in figure 6.14.

potential to ring 03, one can compensate for the too early retardation to some extent, but only at the cost of an increasing potential depression (from the order of 0.1 V).

Additionally, for a longer electrode a bump in the edge of  $E_{\parallel}$  at  $z_{spec} \approx \pm 11$  m develops, which will be discussed more in detail in the next section.

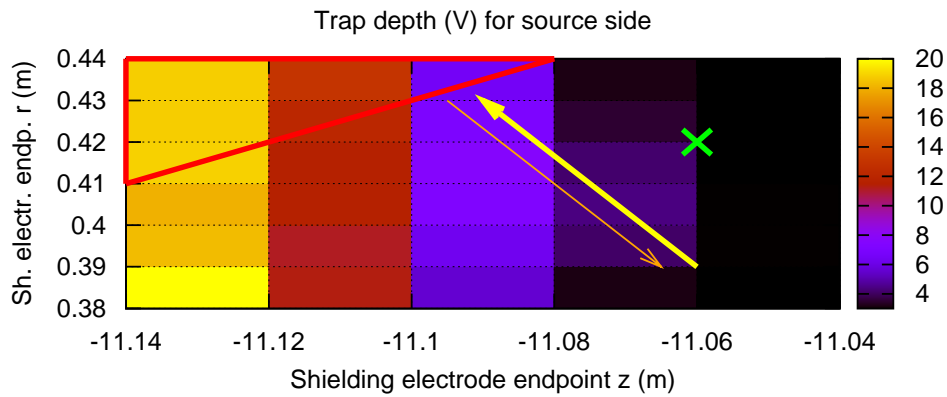
Concerning the potential depression small radii are favoured, but this effect plays a minor role compared to the effects mentioned before.

**Conclusion** Altogether, the position of the shielding electrode has to be optimised with regard to the electric field strength, the transmission properties and the potential depression. However, the Penning traps caused by a too steep electrode angle and the Penning trap at the end of the shielding electrode limit the parameter range. This is summarised in figure 6.14.

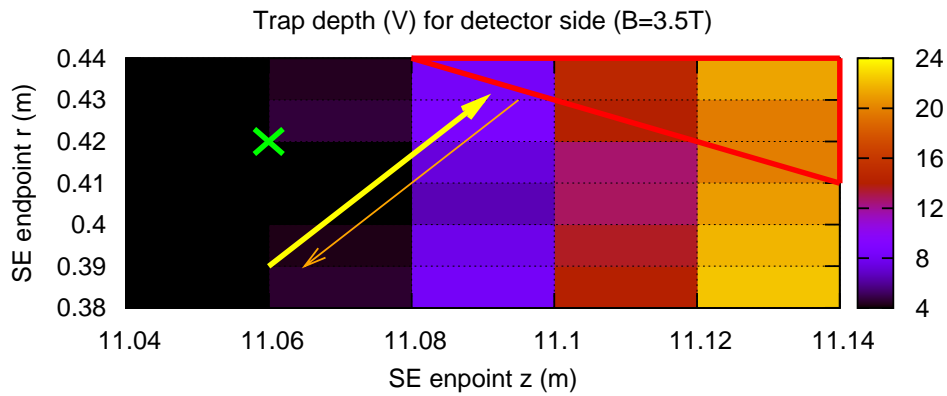
In the region without Penning traps with a critical depth the transmission properties are not sufficient. They have to be improved by applying a slightly more positive potential ( $U_{03} \approx -18560$  V instead of  $U_{03} \approx -18600$  V in previous setups) to the module ring 03. This causes an increasing potential depression.

The influence of the mounting position on the potential depression ( $\Delta U \approx 0.01$  V) is not as big as the influence of the ring 03 potential ( $\Delta U \approx 0.2$  V). Hence, it is reasonable to mount the electrode at a large radius while also keeping a safe distance to the regions with Penning traps. This is also advisable to reduce the electric field strength.

Considering all the limits and effects mentioned above, a preliminary (cf. section 6.2.5) endpoint position of  $r = 0.42$  m and  $z = 11.06$  m was chosen (see figure 6.14). With this, also the preliminary endpoint of ring 02 is fixed to  $z = 11103.3$  mm and  $r = 460$  mm by the results obtained in the last chapter.



(a) Detector side



(b) Source side

**Figure 6.14:** Summary of the limits on the endpoint position of the shielding electrode / ring 02 system:

The plots show the depth of the Penning trap at the end of the shielding electrode depending on the shielding electrode endpoint for (a) the source side and (b) detector side (detector magnet at  $B_{det} = 3.5\text{ T}$ ). The potential of ring 02 is set to  $U_{02} = 18500\text{ V}$  and the shielding electrode potential is  $U_{SE} = U_{vessel} = 18500\text{ V}$ . The trap depth is significantly reduced for a shielding electrode which is long enough.

Setups in the area of the red triangle host deep Penning traps because of field lines crossing the ground electrode twice or leaving it in an unfavourable angle.

Also shown are the tendencies for better transmission properties (significant effect, yellow line) and a smaller potential depression (small effect, orange line). The proposed mounting position is marked with a green cross.

## 6.2.5 Penning trap at module ring 02

A closer review of module ring 02 has revealed an additional Penning trap at this position. A cathode-to-vacuum trap is located at field lines emerging from the ring 02 wires in the direction of the spectrometer centre, as can be seen in figure 6.15<sup>11</sup>.

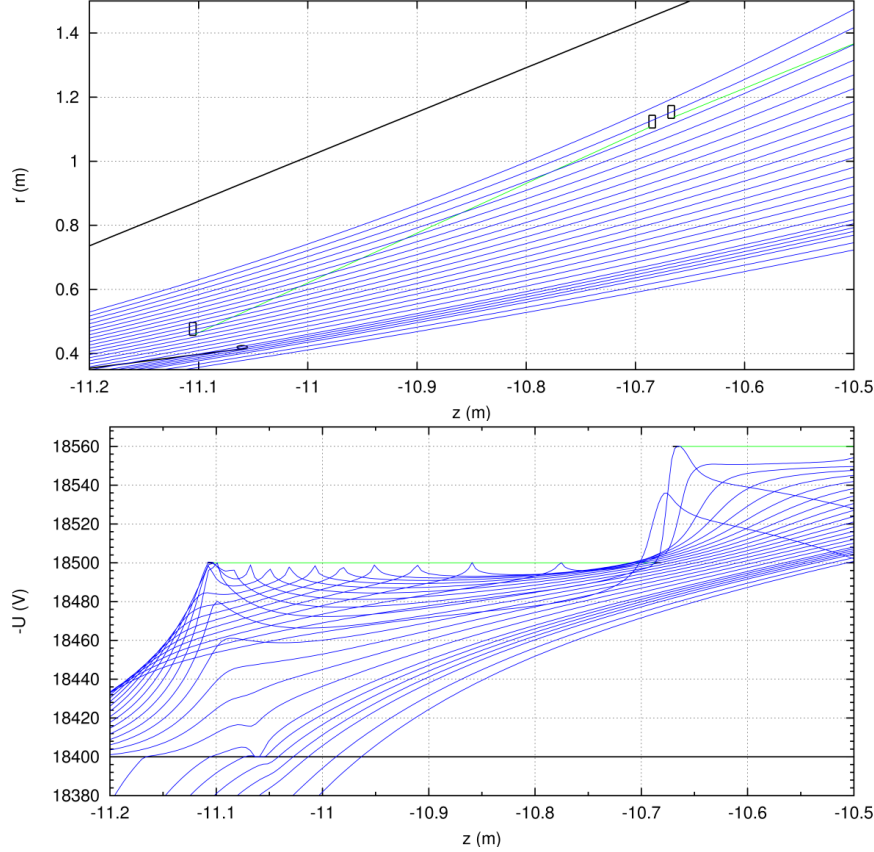


**Figure 6.15:** The magnetic field lines (top) and corresponding electric potentials (bottom) in the region of ring 02 for an unmodified shielding electrode as proposed in section 6.2.4. The potential of field lines emerging from the ring 02 wire electrode ( $U_{02} = -18500\text{V}$ ) drops due to the influence of the ground and shielding electrode potential, forming a Penning trap with  $\Delta U > 20\text{V}$ . The field lines eventually hit the electrodes again at ring 03 or the flat cone modules. The trap at the shielding electrode is small as expected from the optimisations done in the previous chapters.

The trap is induced by the ground electrode with its relative to ring 02 positive potential ( $\Delta U(02, GE) = 18.4\text{kV}$ ) and the shielding electrode. Although the potential difference between the shielding electrode and the ring 02 is much smaller ( $\Delta U(02, SE) = 100\text{V}$ ) the shielding electrode has an impact on the trap depth as it is located close to the trap.

<sup>11</sup>For a better visibility of the traps, the comb potential is set to wire potential ( $\Delta U_{comb,02} = 0\text{V}$ ) in the setups described in this section. The comb potential can and must be tuned separately, as also at this position Penning traps can develop. This will be discussed in the next section.

Figure 6.16 shows the dependence of the trap depth on the ring 02 potential. The trap depth decreases linearly with a more positive ring 02 potential<sup>12</sup>. It is reduced to  $U_{02trap} \approx 12$  V for  $U_{02} = U_{SE} = -18400$  V. As in this case only the ground electrode has a more positive potential than the ring 02 electrode it has to be the cause for the trap. Simulations have been made with shorter ground electrodes which show a decreasing trap depth, hence supporting this thesis.

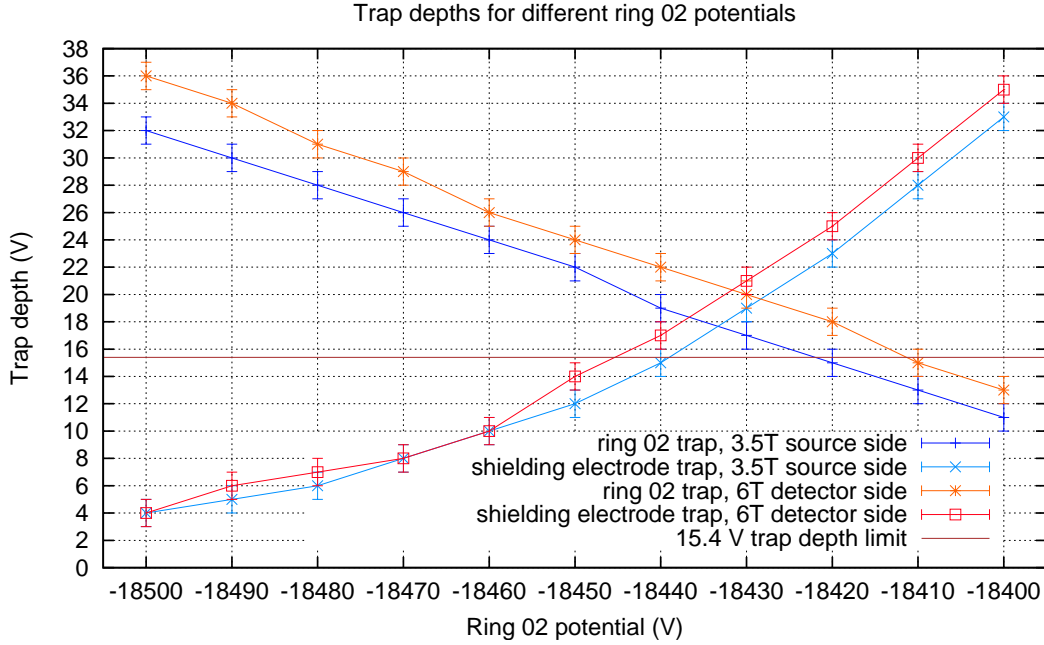


**Figure 6.16:** The depths of the traps at the end of the shielding electrode and ring 02 for a setup as proposed as preliminary setup in the last section depending on the potential of the electrode ring 02. Applying a more positive potential to ring 02 decreases the trap depth of the ring 02 trap at the cost of an increasing trap depth of the shielding electrode trap. It is not possible to tune both trap depths below the limit of  $e\Delta U < 15.4$  V with the ring 02 potential as single parameter.

The problem cannot be solved just by rising the ring 02 potential, as the trap depth at the end of the shielding electrode increases for smaller  $\Delta U(02,SE)$  (see figure 6.16). This is because of the relative to the shielding electrode more negative potential of ring 02. It influences the effective potential at the end of the shielding electrode (compare section 6.2.3). By reducing this potential difference  $\Delta U(02,SE)$ , the effective potential in this region gets more positive and thus the trap depth increases.

As can be seen in figure 6.16, it is not possible to tune both trap depths below the limit of  $e\Delta U < 15.4$  V with the ring 02 potential as single parameter.

There are several possible ways to solve this problem. As the parts for the ring 02

<sup>12</sup>Increasing the potential of ring 02 to even more positive values  $U_{02} > -18400$  V would further decrease the trap depth at ring 02 but give rise to new Penning traps between the vessel hull, the shielding electrode and the electrodes. As seen in figure 6.16, it is not expedient to do this anyway with regard to the trap at the end of the shielding electrode.

modules are already produced at the time when this problem was found, it would be solved most practically when maintaining the geometry of ring 02.

One possible solution is to elongate the shielding electrode while retaining its already optimised angle. By that, more of the ring 02 electrode will be shielded from the ground electrode potential, lowering the trap depth at ring 02. On the other hand the problematic end of the shielding electrode is moved away further from the ground electrode, thus lowering the trap depth at the shielding electrode.

Three possible setups have been simulated which correspond to elongations in z-direction of  $\Delta z = 65$  mm,  $\Delta z = 130$  mm and  $\Delta z = 260$  mm in relation to the formerly proposed setup ( $\Delta z = 0$ ).

The impact of a longer shielding electrode on the transmission properties is depicted in figure 6.17. For longer shielding electrodes, a bump in the edge of the longitudinal energy (at  $z \approx \pm 11$  m) develops. As discussed in section 4.5, such a setup can host a particle trap and has to be avoided. Thus, the setup with an elongation of  $\Delta z = 260$  mm is not suitable. For the shorter shielding electrode solutions the problem gets less prominent. The strength of this effect also depends on the ring 02 potential: A more negative potential can, in some cases, diminish the bump in the longitudinal energy, but this effect is small against the influence of the potential on the Penning traps.

The resulting trap depths for different shielding electrode length and two different potentials applied to ring 02 can be found in figure 6.18. A longer shielding electrode indeed improves both the trap depth at ring 02 and the trap depth at the shielding electrode. By tuning the potential of ring 02 one can find a trade-off between on the one hand the shielding effect with regard to the tank and the depth of the trap at the end of the shielding electrode and on the other hand the trap depth at ring 02.

Based on these results a setup is proposed with a shielding electrode which is  $\Delta z = 65$  mm longer in z-direction relative to the preliminary setup proposed in section 6.2.4<sup>13</sup>. The shielding electrode endpoint position (centre of endbulge) then is  $z = 10995$  mm and  $r = 448$  mm

The potential applied to the ring 02 electrode directly influences the trap depth at the ring 02 and the shielding electrode. It is therefore a good handle to find out the critical depth in the final KATRIN setup. A solution with the maximum shielding potential but without igniting traps has to be found experimentally when the test measurements at the main spectrometer take place.

---

<sup>13</sup>An even longer electrode would have two drawbacks, namely the inferior transmission properties in the steep cone region mentioned above and the mechanical feasibility and accuracy, which is demanding even for the chosen setup. The advantage of 10 V more shielding potential to the tank (which would be possible regarding the trap depth in a setup with  $\Delta z = 130$  mm) does not justify this.

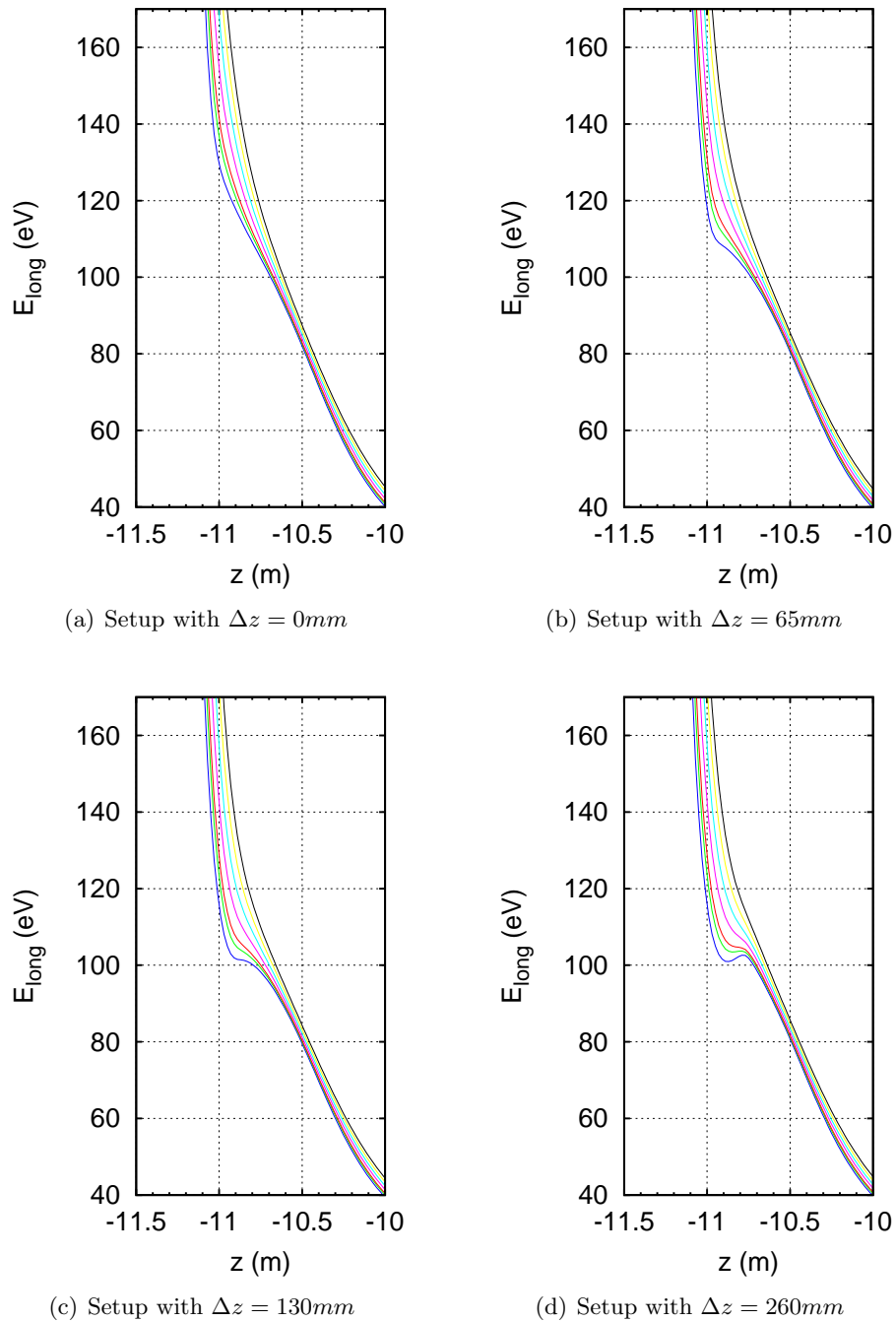


**Figure 6.17:** The transmission properties for different lengths of the shielding electrode for the source side ( $U_{02} = -18420\text{V}$ ). A longer shielding electrode worsens the transmission properties up to a point where a particle trap can develop.

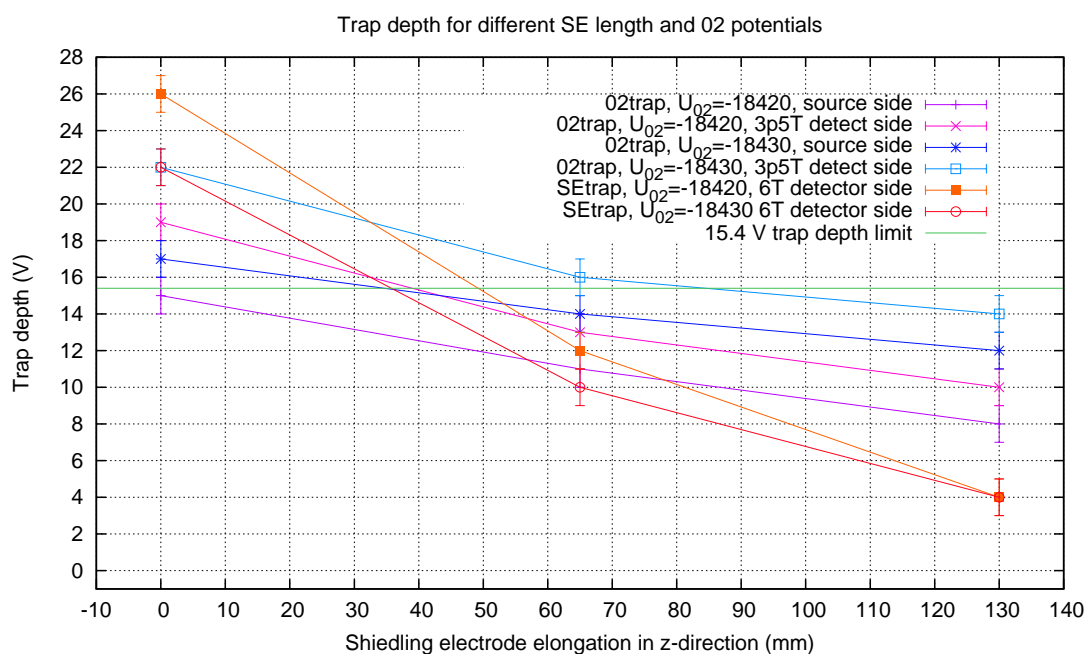


**Figure 6.18:** The trap depth at the shielding electrode (denoted as SEtrap) and at ring 02 (denoted as O2trap) for different setups. For a longer shielding electrode the depth of both traps decreases. Note that a more positive ring 02 potential leads to deeper traps at the shielding electrode, but more shallow traps at ring 02.

### 6.2.6 Module ring 02 and 03 comb potential

The potential of the ring 02 and 03 combs has to be optimised also to avoid additional traps.

As stated in section 5.2, the basic idea of a potential difference  $\Delta U_{\text{comb}}$  between the combs and the wires is to shield electrons emitted from the combs (which have a much bigger surface and mass) by the (thin, light) wire layer. Hence, a higher potential difference  $\Delta U_{\text{comb}}$  is desirable to improve the shielding.

The potential of the combs for the rings 02 and 03 can be optimised separated from the other parameters discussed in this chapter and also separately from each other<sup>14</sup>:

- The applied potential differences  $\Delta U_{\text{comb}}$  influence significantly only the potential in the near vicinity of the combs, so this is a local effect.
- At the joint of rings 02 and 03 the two combs are very close to each other spatially. As proposed in the last chapter the potential difference between the ring 02 and 03 electrode wires is about  $\Delta U(02,03) = 140\text{V}$ . Hence, although there is an influence of one comb on the other, the potential optimisation of the combs does not influence the potential along the course of the magnetic field lines in the region of the other comb in a significant way.

The optimisation process will be discussed for the detector side of the spectrometer with a magnetic field  $B_{\text{det}} = 6\text{T}$  at the detector magnet as this is the case with the most problematic course of the field lines and the deepest traps.

#### Module ring 02

In section 6.2.5 the Penning trap at the wires of module ring 02 was discussed. The potential difference  $\Delta U_{02\text{comb}}$  applied to the combs of ring 02 has no influence on this trap in a reasonable parameter range.

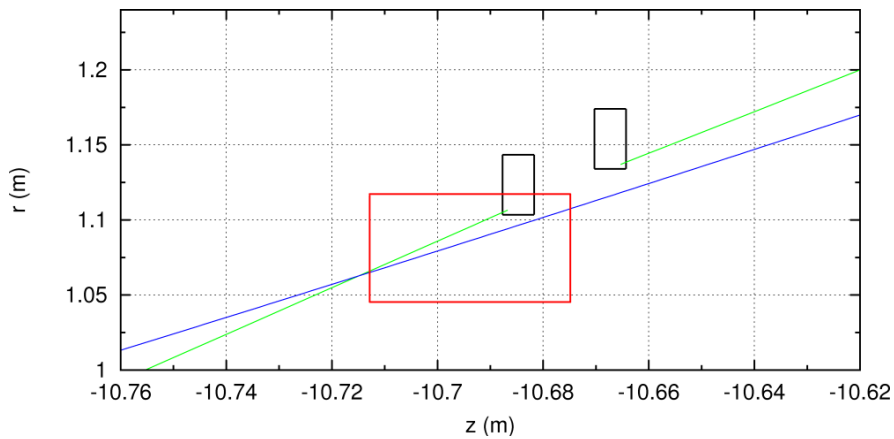
Another possible trap location is located very close to the inner comb of ring 02. Field lines which emerge from the electrode wires of ring 02 and proceed in the direction of ring 03 get very close to the comb on the side facing the spectrometer centre. This is shown in figure 6.19(a).

The more positive potential of the combs induces a spatially small ( $< 2\text{cm}$ ) trap close to the wires. This trap has a depth of  $\Delta U_{\text{trap}} \approx 4\text{V}$  for  $\Delta U_{02\text{comb}} = 0\text{V}$ . The trap depth increases to  $\Delta U_{\text{trap}} \approx 14\text{V}$  for  $\Delta U_{02\text{comb}} = 20\text{V}$  (see figure 6.19(b)). A higher potential difference  $\Delta U_{02\text{comb}}$  further deepens this trap. Therefore  $\Delta U_{02\text{comb}} = 20\text{V}$  constitutes a limit on the ring potential.

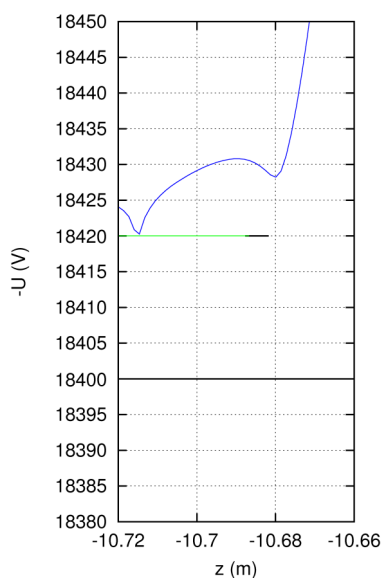
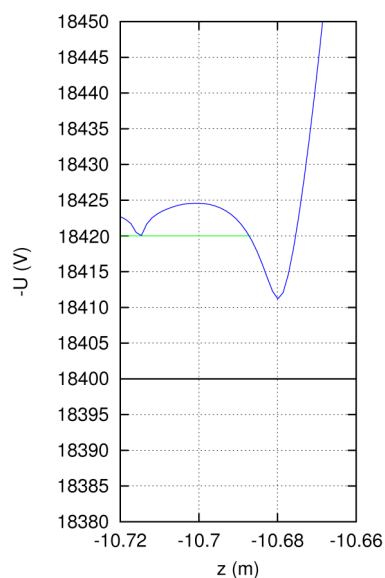
As it is not clear if a spatially as small trap will lead to an increased background, the comb potential should be tuned in test measurements in the final KATRIN setup.

---

<sup>14</sup>Both combs of one module have the same potential as they are connected by c-profiles.



(a) Magnetic field lines

(b) Setup with  $\Delta U_{02comb} = 0$  V(c) Setup with  $\Delta U_{02comb} = 20$  V

**Figure 6.19:** The magnetic field lines and the potential for two different comb potentials  $\Delta U_{02comb}$  (detector side,  $B_{det} = 6$  T). The problematic area is marked with a red rectangle, the trap described in section 6.2.6 can be seen at the innermost (blue) field line.

### Module ring 03

At module ring 03 Penning traps can develop at different positions and will be discussed separately. Figure 6.20 shows the magnetic field lines in the region of module ring 03. The electric potential along these field lines is shown in figure 6.21 for different module 03 comb potentials  $\Delta U_{03comb}$ .

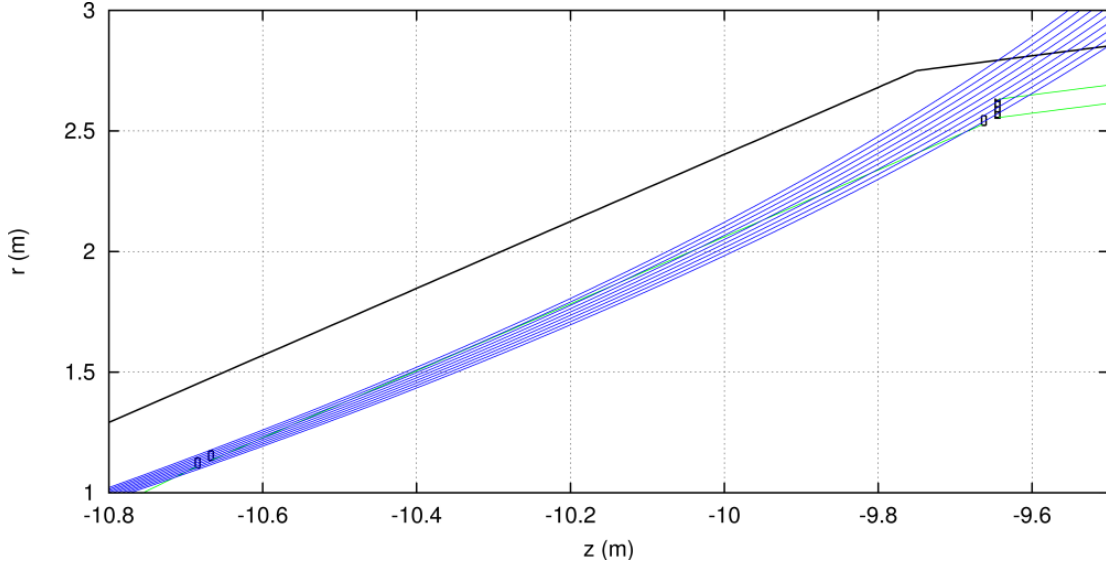


**Figure 6.20:** The magnetic field lines in the region of ring 03 at the detector side ( $B_{det} = 6 \text{ T}$ ).

**Main trap** There are field lines crossing the wires of the module ring 03 twice. The tank potential shines through the wire electrode, giving rise to a more positive potential on the inside of the wire electrode. This more positive potential then gives rise to a trap (marked A in figure 6.21). The trap depth is not depending on the parameter optimisations discussed in the previous sections.

The location of the maximum depth of this trap shifts depending on the comb potential. For  $\Delta U_{03comb} = 0 \text{ V}$ , the maximum depth of the trap  $\Delta U_{trap} \approx 14 \text{ V}$  is located at  $\approx 9.9 \text{ m}$ . The depth of the (same) trap at  $z \approx 10.6 \text{ m}$  is  $\Delta U_{trap} \approx 12 \text{ V}$ .

Rising the comb potential up to  $\Delta U_{03comb} = 60 \text{ V}$  shifts the maximum trap depth to a position at  $z \approx 10.6 \text{ m}$  with  $\Delta U_{trap} \approx 15 \text{ V}$  while the depth at  $z \approx 9.9 \text{ m}$  remains the same.

Applying even more positive potential to the combs leads to a deeper trap with its maximum depth now located near the outer comb at  $z \approx 10.6 \text{ m}$ .

**Traps in the comb regions** The second type of trap is provoked by field lines hitting the mounting ring and then run on the outer side (to the vessel hull) of the electrodes. The more positive tank potential gives rise to a trap of  $\Delta U_{trap} \approx 15 \text{ V}$  for  $\Delta U_{03comb} = 0 \text{ V}$  at the combs (marked B and C in figure 6.21). Raising the comb potential to  $\Delta U_{03comb} > 20 \text{ V}$  lowers the trap depth to values below  $10 \text{ V}$ .

As this trap is located on the outer side of the electrodes, it is shielded from the vessel hull by the wire electrode. Although, the trap should be avoided. Hence, the shielding potential of the rings is limited to  $20\text{ V} \lesssim \Delta U_{03comb} \lesssim 60\text{ V}$

Also for the comb potential  $\Delta U_{03comb}$  the exact value should be found out experimentally to find the best trade-off between the background reduction due to the shielding potential and the additional background possibly caused by Penning traps.

### 6.3 Conclusion and proposed setup

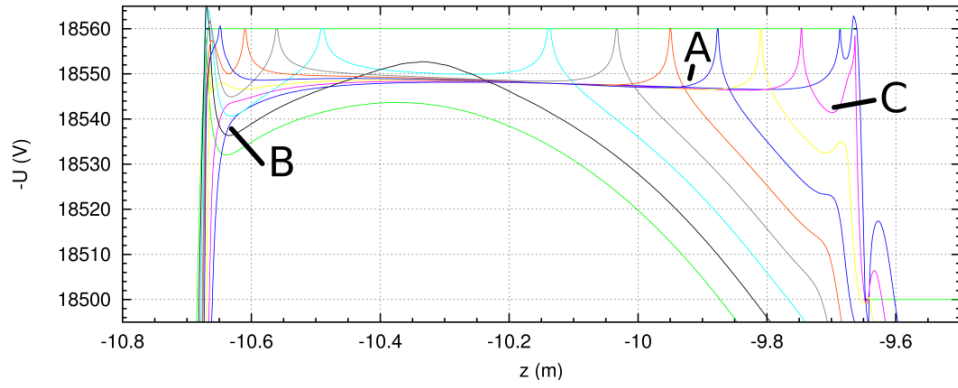
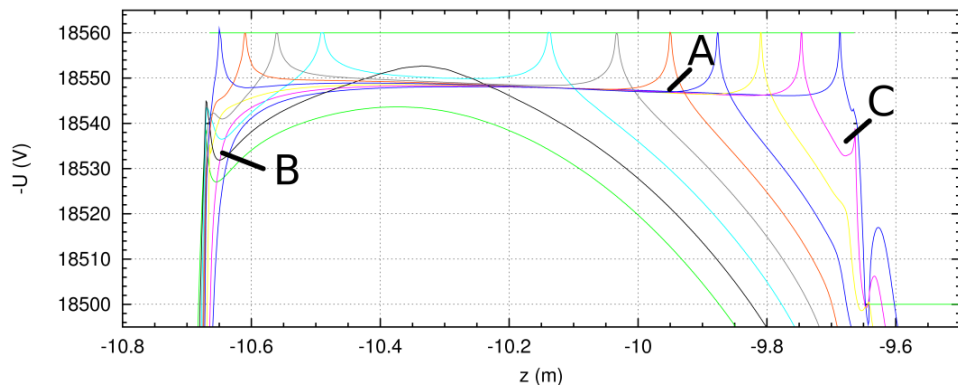
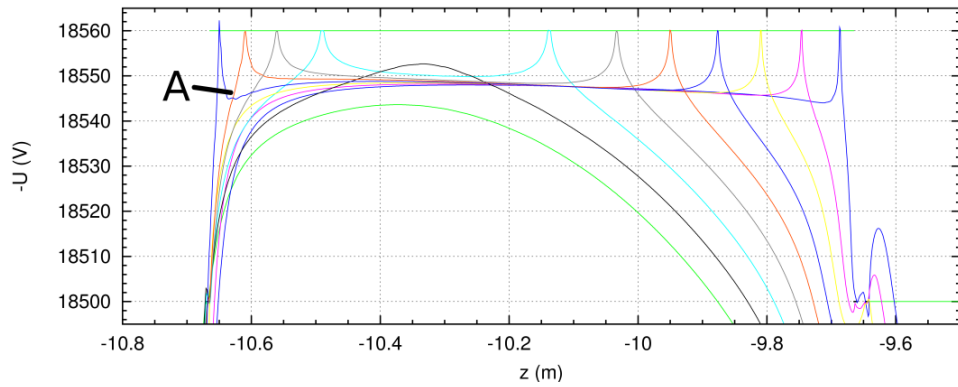
In this chapter several optimisation processes were discussed which have resulted in a mechanically demanding proposed setup. It was demonstrated that this setup is the result of many limits and effects which have to be considered carefully.

A solution was found to suppress the Penning trap at module ring 02 without changing the design of the already produced parts of the wire electrode modules.

The electrode wires of the steep cone modules were intended to have a diameter of 0.3 mm. The large angle and small radius of these modules result in a high strain on the ceramics holding the wires, leading to the risk of broken ceramics. To solve this problem, wires with a smaller diameter of 0.2 mm are used.

This change in the mechanical design has only a small impact on the results obtained in this chapter. The depth of the Penning trap at module rings 02 and the main trap at module ring 03 is increased by about 1.5 V. This is roughly in the region of the uncertainty of the simulated trap depth (see 6.2).

The proposed parameters for the design are given in table 6.1, important results for this proposed setup are summarised in table 6.2. A CAD drawing of the proposed steep cone design can be found in the figure A.1. The `xml` file of the proposed geometry for the *MainSpec* program can be found in the appendix B.

(a) Setup with  $\Delta U_{03comb} = 0$  V(b) Setup with  $\Delta U_{03comb} = 20$  V(c) Setup with  $\Delta U_{03comb} = 60$  V

**Figure 6.21:** The electric potentials along the magnetic field lines shown in figure 6.20 for different comb potentials. The behaviour of the three possible traps discussed in section 6.2.6 can be seen for the different ring potentials. The main trap is marked by an A, the comb traps are marked B and C.

**Table 6.1:** *The proposed set of parameters for the steep cone region.*

ground electrode kink	$z = 11700\text{mm}$ $r = 100\text{mm}$
ground electrode endpoint	$z = 11.46955\text{ m}$ $r = 0.17605\text{ m}$
ground electrode end bulge centre	$z = 11473\text{mm}$ $r = 186.5\text{mm}$
ground electrode end bulge circle radius	$R_{bulge,GE} = 11\text{mm}$
shielding electrode inner end bulge circle centre	$z = 10995\text{mm}$ $r = 448\text{mm}$
shielding electrode outer end bulge circle centre	$z = 11624\text{mm}$ $r = 178\text{mm}$
shielding electrode end bulge radii	$R_{bulge,SE} = 5\text{ mm}$
module ring 02 outer endpoint (wire kink position)	$z = 11103.3\text{mm}$ $r = 460\text{mm}$
module ring 02 potential	-18420 V
module ring 02 comb potential	-18400 V ( $\Delta U_{02comb} = 20\text{ V}$ )
module ring 03 potential	-18560 V
module ring 03 comb potential	-18500 V ( $\Delta U_{03comb} = 60\text{ V}$ )

**Table 6.2:** *Summary of important values resulting from the proposed setup.*

Maximum field strength at cathode (shielding electrode outer bulge)	$\approx 640\text{ kV/m}$
Maximum field strength at anode (ground electrode end bulge)	$\approx 1020\text{ kV/m}$
Penning trap depth at end of shielding electrode	$\Delta U \approx (12 \pm 1)\text{ V}$ (for $U_{02} = -18420\text{ V}$ ) $\Delta U \approx (10 \pm 1)\text{ V}$ (for $U_{02} = -18430\text{ V}$ )
Main Penning trap depth at ring 02	$\Delta U < (14 \pm 1)\text{ V}$ (for $U_{02} = -18420\text{ V}$ ) $\Delta U < (17 \pm 1)\text{ V}$ (for $U_{02} = -18430\text{ V}$ )
Main Penning trap depth at ring 03	$\Delta U < (15 \pm 1)\text{ V}$
Potential depression	1.04 V



# 7 Field emission at the KATRIN main spectrometer wire electrode

The KATRIN main spectrometer features an inner wire electrode for background suppression. The inner wire layer of this electrode is on a different electric potential than the mounting structure. At the wire mounting positions high electric field strength of several hundred kV/m occur between the wires and the mounting structures, possibly leading to field emission. The created electrons could reach the sensitive spectrometer area, thus disturbing the measurements. An experiment was conducted to further investigate the field emission process at the critical position.

The first section will present a more detailed motivation for the experiment, followed by a section describing the experimental setup. In section 7.3 the energy calibration will be discussed. The actual measurements will be discussed in section 7.4. The results will be analysed and an upper limit on the measured field emission rate will be derived in the section 7.5.2.

## 7.1 Motivation

As already discussed in section 5.2, the inner wire electrode of the main spectrometer is divided into electrode modules. Each electrode module consists of one or two wire layers and two combs which are connected by c-profiles for mechanical stability. The modules of the steep cone of the main spectrometer feature only one wire layer. Therefore, the holding structure can be reduced to a ring<sup>1</sup>.

In order to improve the shielding properties of the wire electrode, the wires are on a more negative potential than the combs (see section 4.6 for a detailed explanation). For the central and flat cone modules, the potential difference between the inner wire layer and the combs is  $\Delta U_{\text{wire}} = 100 \text{ V}$ . For the steep cone part, a potential difference of approximately  $\Delta U_{\text{wire}} = 20 \text{ V}$  (ring 02) and  $\Delta U_{\text{wire}} = 60 \text{ V}$  (ring 03) was suggested in chapter 6.

For electrical insulation the wires are mounted by using ceramic tubes which are inserted into drillings in the combs. The small distance between the wires and the edges of these drillings gives rise to a high electric field strength of several hundred kV/m at the surface of the wires.

Figure 7.1 shows the geometry for the three kinds of wire module types (cylinder modules, steep and flat cone modules):

- The wires of the cylinder modules are guided perpendicular to the comb (see figure 7.1(c)), leading to a distance of 0.8 mm between the wires and the edges of

---

<sup>1</sup>Nevertheless these rings are called combs to avoid ambiguity with the module rings (e.g. module ring 02).

the comb drillings.

- For the flat cone modules the geometry of the drillings is similar to the cylinder modules. But here the wire emerges not perpendicular to the comb, leading to a smaller distance of 0.63 mm between the wire and the edge of the drilling (see 7.1(b)).
- The geometry for the steep cone modules is different from the abovementioned modules. The angle between the wires and the combs is even steeper, but here the distance between wires and combs is higher because of an inserted notch, as can be seen in 7.1(a). A CAD drawing of this position can also be found in 5.7.

Thus, the highest field strengths are expected for the flat cone modules at critical positions where the wires emerge from the ceramics.

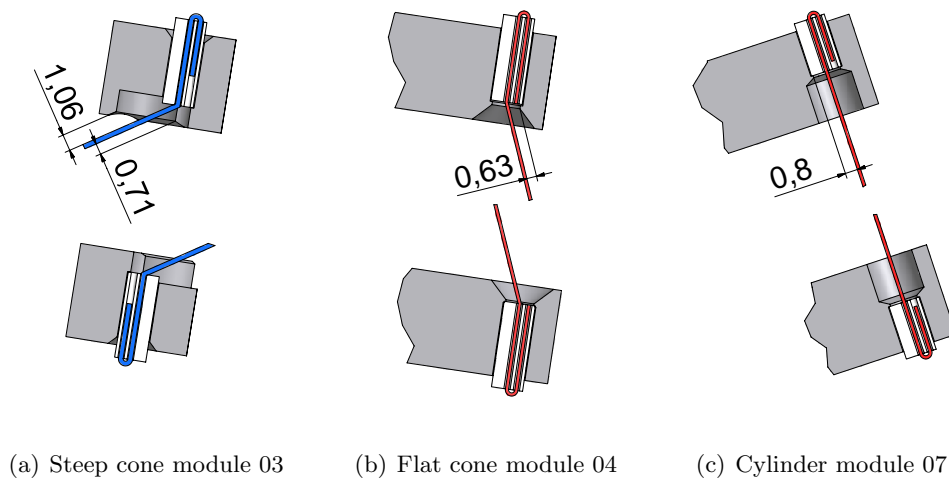


**Figure 7.1:** The teeth with the ceramic insulators (white) and the wires (red) for the different module types. The minimum distance from the wire to the edge of the tooth is given in mm.

To estimate the field strength at the wire, the simplified case of a wire in a cylindrical tube shall be discussed, neglecting the edges of the tooth and the angle of the wire. An inner cylinder with a radius  $R_1$  is surrounded by a cylinder with a radius  $R_2 > R_1$  with a common symmetry axis (see figure 7.2). The cylinders are assumed to be infinitely long so that boundary effects can be neglected. Because of the symmetry of the geometry it is sufficient to describe the electric field strength by the radius  $\rho$ . The field strength is given by [Nol04]

$$E(\rho) = \frac{U}{\rho \ln \frac{R_2}{R_1}}, \quad (7.1)$$

where  $U$  denotes the applied potential between the cylinders.

The inner cylinder can be identified as the wire, the outer cylinder corresponds to the tooth drilling. For the wire the real value of  $R_1 = 0.15$  mm is used while for the outer

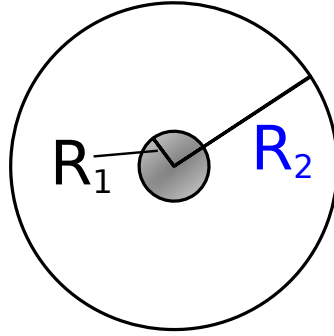


**Figure 7.2:** *Illustration to the field strength calculation (eq. 7.1).*

radius  $R_2$  the minimal distance between the wire and the drilling is assumed since the more complicated geometry cannot be resembled in this approximation. For the projected wire potential difference of  $\Delta U_{\text{wire}} = 100 \text{ V}$  a field strength of about  $500 \text{ kV/m}$  can be calculated using eq. 7.1, neglecting the influence of surface irregularities. This field strength does not exclude the field emission process, as discussed in section 3.2.

If field emission takes place at these positions, there would be no electric shielding by the wire electrode, only magnetic shielding as stated in section 4.6. Thus, the emitted electrons may enter the sensitive main spectrometer volume and reach the detector, thus increasing the background level. This calls for experimental evidence that no field emission occurs at these critical positions.

During module assembly tests are made to check the high voltage stability between the wires and the tooth at  $\Delta U \approx 1 \text{ kV}$ , searching for short circuits resulting from processing errors in the mounting procedure. These test show a typical resistance for a flat cone module of  $R_m \geq 1 \text{ G}\Omega$ . By applying Ohm's law one obtains a corresponding current of  $I_m \leq 10^{13} \text{ e}^-/\text{s}$ . Hence, the sensitivity of this measurement method is not good enough to give information on field emission.

To rule out field emission, a realistic test setup was built in a vacuum environment with the capability to detect the electrons emitted by field emission. The test setup mimics the situation of the most critical modules, the flat cone modules. In the case that no field emission can be found here, the other positions can be expected to be noncritical as well.

## 7.2 Setup

A schematic overview of the setup is given in figure 7.3. Pictures of the complete setup can be found in figure 7.7. More detailed CAD drawings are given in the appendix A.3. The type numbers of the devices used are given in appendix A.1.

**Wire/tooth setup** In order to provide a realistic test for field emission, a real tooth of a flat cone module is used within the setup. It has been detached from a comb and was placed on a plastic insulator made of PEEK (Polyetheretherketone), as can be seen in figure 7.4. The insulator has the purpose to guide the wire to the tooth and to allow the application of a potential difference  $\Delta U_{\text{wire}}$  between the wire and the tooth.

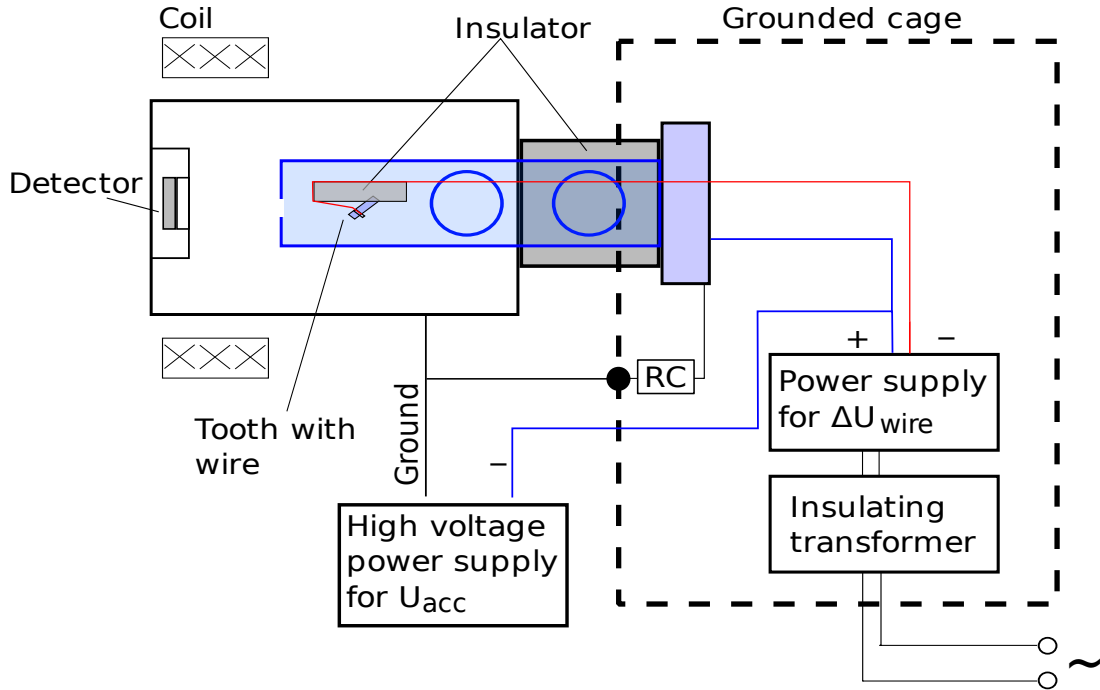


**Figure 7.3:** Overview of the field emission test setup: All high voltage parts are surrounded by a grounded safety cage.

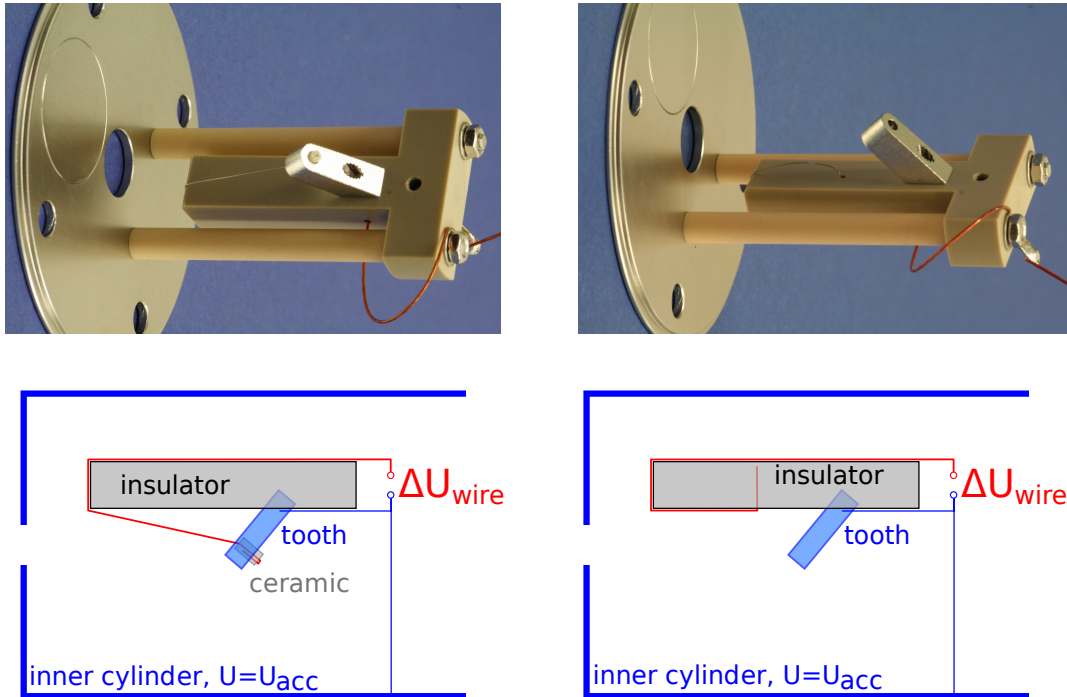
In the KATRIN experiment, the wire modules will be at a potential  $U_{mod} \approx -18.5$  kV relative to ground potential, but the critical field strength is caused by the potential difference  $\Delta U_{wire}$  between the wire and the comb. Hence the module potential  $U_{mod}$  is not needed in the test setup. Nevertheless an acceleration potential  $U_{acc}$  is needed to detect the electrons, as discussed below.

Two different versions of the wire/tooth setup were used during the measurements:

- The regular setup version is shown in figure 7.3 and figure 7.4(a). Here the insulator guides the wire to the ceramic in the tooth under the same angle as in a real module. With this setup two measurement periods were accomplished to search for field emission.
- The third measurement period featured a slightly different setup, as shown in figure 7.4(b). The wire is not guided into the tooth, but is fed back through the insulator instead. The setup remains unchanged except for the critical position. Thus, in this setup no field emission at the point critical point can take place. In the case field emission is found with the regular setup at a potential difference  $\Delta U_{wire}^{FE}$ , the same potential difference will be applied to this altered setup. If no field emission signal can be found with this setup, it is shown that the field emission measured originates from the assumed critical position at the wire.

Although in the KATRIN setup the proposed potential difference is  $\Delta U_{wire} = 100$  V, it is reasonable to use a power supply that can generate a higher potential difference to identify the threshold potential difference  $\Delta U_{FE}$  where field emission can be detected.

This is also a good way to check the validity of the results: If field emission can be observed at  $\Delta U > \Delta U_{FE}$ , it is shown that the setup is capable of detecting the emitted electrons.



(a) The regular setup used for the first two measurement periods: The wire is mounted into the tooth by a ceramic and the wire emerges from the tooth at the same angle as in the real flat cone modules.

(b) The altered setup used in the third measurement period: The wire is guided through a hole in the insulator and therefore not connected to the tooth.

**Figure 7.4:** Details of the two wire/tooth setup variants described in section 7.2: The tooth is mounted on an insulator. It is on the same potential  $U_{acc}$  as the inner cylinder used to shield the wire/tooth setup from the acceleration voltage (see text p.73). The wire is guided over the insulator, the potential difference  $\Delta U_{wire}$  is provided by the power supply in the safety cage.

**Detector and acceleration voltage** To detect the electrons a Si-PIN diode in front of the tooth was used together with a preamplifier. This signal was amplified further by a spectroscopy amplifier and then routed to a PC based data acquisition system.

The minimum energy of charged particles which can be detected with this system is limited by the background level of the system. For the given detector setup the minimal energy for electrons to be detected is about  $E_{min} \gtrsim 10$  keV (see calibration and measurements below). Hence, an acceleration voltage is needed with  $-eU_{acc} > E_{min}$  to accelerate the electrons to the detector. To provide this acceleration voltage, the wire/tooth system described above is put on  $U_{acc}$  (the wire is still put on  $\Delta U_{wire}$  relative to  $U_{acc}$ ) while the detector is grounded.

**Inner cylinder** The wire/tooth setup has to be shielded from the acceleration voltage because otherwise the field strength at the sharp edges of the wire/tooth setup would be very high. They would exceed the field strength caused by  $\Delta U_{\text{wire}}$  and impede the high voltage stability<sup>2</sup>. Therefore the wire/tooth setup is mounted into a metal cylinder which is also on the acceleration potential  $U_{\text{acc}}$ .

The cylinder has a small hole ( $r = 6 \text{ mm}$ ) in the head plate to allow the electrons to reach the detector (see figure 7.5). This hole is an electrical lens<sup>3</sup>, focusing the electrons from the inside.

Big holes in the lower part of the cylinder walls (near to the flange) improve the vacuum conditions<sup>4</sup>. The whole inner cylinder setup is mounted to a flange for mechanical stability. Hence, the mounting flange is also put on  $U_{\text{acc}}$ . The wire potential  $\Delta U_{\text{wire}}$  is fed to the inside of the vessel by a vacuum feed-through in this flange.

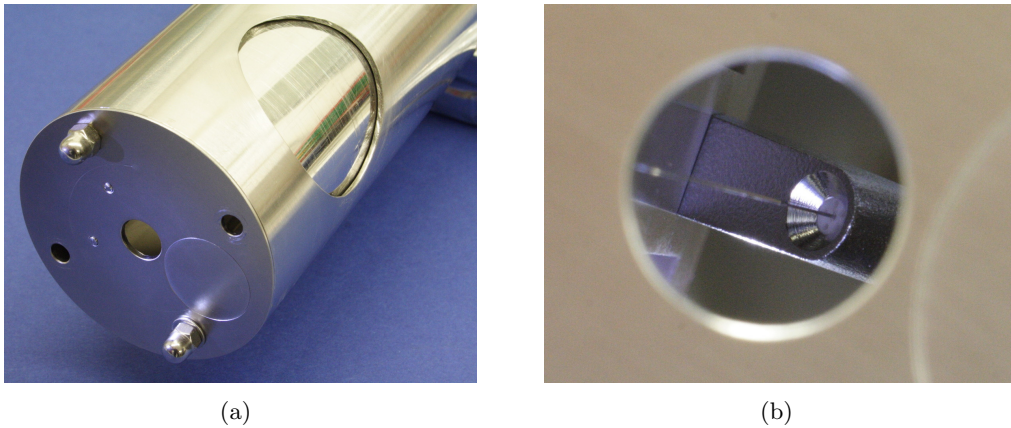


**Figure 7.5:** Pictures of the inner cylinder with the wire/tooth setup. (a) shows the inner cylinder: The big hole in the cylinder wall was intended to provide better vacuum properties, but had to be closed to shield the acceleration voltage from the inner setup. At the bottom of the cylinder (not shown) are four similar holes that remain open, as they are sufficiently far away from the wire/tooth setup and do not cause voltage breakdowns. In (b) the wire/tooth setup is shown viewed through the hole at the top of the inner cylinder shown in (a).

**Vacuum system** To mimic the vacuum conditions of the main spectrometer, the test setup is located in a vacuum vessel. Compared to the KATRIN main spectrometer, where the pressure shall reach  $p < 10^{-11} \text{ mbar}$ , in the test setup  $p \approx 10^{-7} \text{ mbar}$  was reached<sup>5</sup>. The vacuum vessel is grounded so that it is still accessible and there is no need for a large safety cage around the whole setup. To insulate the vessel from the mounting flange of the inner cylinder, it is connected via a ceramic tube.

<sup>2</sup>This was shown in an early stage of the experiment, where the inner setup was not shielded by the cylinder. Here, the voltage broke down at 10 – 15kV repeatedly.

<sup>3</sup>The impact of electrical lensing and/or magnetic guidance will be discussed again in section 7.4.

<sup>4</sup>There is a pair of holes at the top of the cylinder walls originating from earlier stages of the experiment. These holes were closed for a better shielding, as can be seen in figure 7.5.

<sup>5</sup>More details about the vacuum setup can be found in [Arl09], where an experimental setup is described which uses the very same vacuum vessel and detector setup.

**Safety cage** For safety reasons the mounting flange is surrounded by a grounded metal cage. This cage also hosts the power supply to generate the potential difference  $\Delta U_{\text{wire}}$  between the tooth and the wire. This power supply is decoupled from ground potential by an insulating transformer, using  $U_{\text{acc}}$  as ground potential. This transformer is also located in the safety cage.

**Magnetic field** To guide the electrons to the detector, a magnetic field symmetrical to the cylinder axis can be applied to the setup. It is provided by a water-cooled coil with 120 copper-windings which can take a current up to  $I_{\text{mag}} = 120 \text{ A}$ , resulting in a maximum field in the centre of the coil of about 0.1 T. This magnetic field is also relevant for a second reason: As the field emission takes place in the vicinity of the electrical more positive tooth, the emitted electrons might have to be guided in the direction of the cylinder hole (where they are accelerated to the detector by  $U_{\text{acc}}$ ) instead of hitting the tooth surface. In section 7.4 the effect of the magnetic field will be discussed again.

**Pulse generator** A pulse generator is connected to the detector system. With these pulses on the one hand an energy calibration can be done (see section 7.3) and on the other it allows to get informations on the background level, as the background level affects the width and shape of the peak in the spectrum which is generated by the pulse generator.

**Background reduction** The mounting flange with the inner setup was connected to ground potential by a RC circuitry of four capacitors and two resistors, as shown in figure 7.6. This was done to prevent the inner setup from potential oscillations. These would induce oscillations at the detector, thus producing a high background level which impedes continuous measurements.

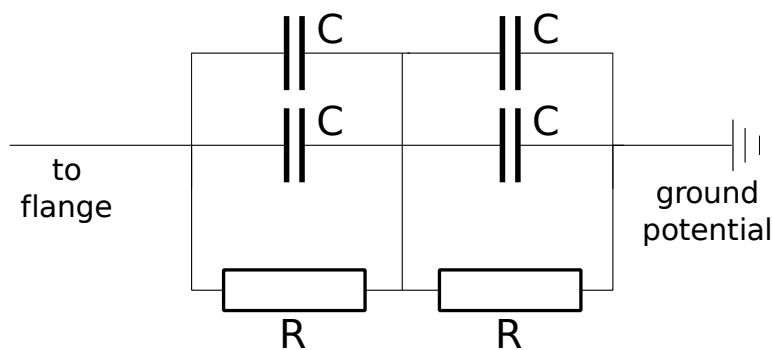


**Figure 7.6:** Diagram of the oscillation suppression circuit. The capacitors have a capacitance of  $50 \text{ nF}$ , the resistors have a resistance of  $63 \text{ M}\Omega$ .

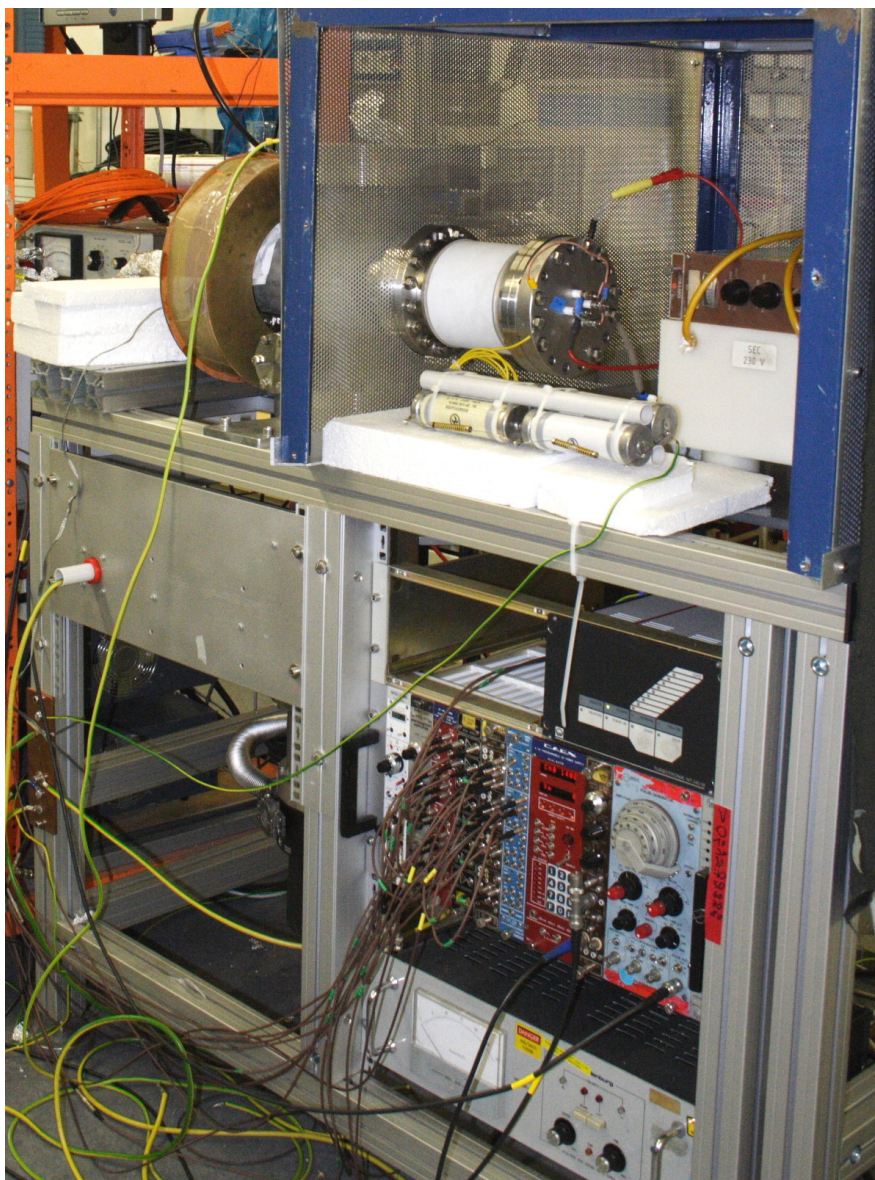


**Figure 7.7:** *The complete setup (without DAQ and power supplies for magnetic field). The safety cage (the front was removed for the photo) contains the insulating transformer (white box) and the power supply for  $\Delta U_{wire}$  on top of it. On the Styrofoam panel the RC circuit for oscillation suppression is located. The flange holding the inner cylinder depicted in figure 7.5 is mounted on an insulator. This insulator is connected to the rest of the vacuum setup which protrudes through the left wall of the cage. Left to the cage the magnetic field coil is located. The rack to the right hosts the high voltage power supply for  $U_{acc}$  (bottom), the frequency generator used for calibrations (see section 7.3), the main amplifier, the detector power supply and the turbo pump controls.*

### 7.3 Energy calibration

The energy calibration is done in several steps. First, instead of the flange with the inner cylinder setup, a plain flange was mounted and put on  $U_{\text{acc}} = 24\text{ kV}$ . In the conditioning process electrons are emitted which result in the calibration spectrum shown in figure 7.8. The major peak on the right is induced by the pulse generator. On the left side, smaller peaks resulting from the 24 kV electrons can be seen above the background edge on the left.

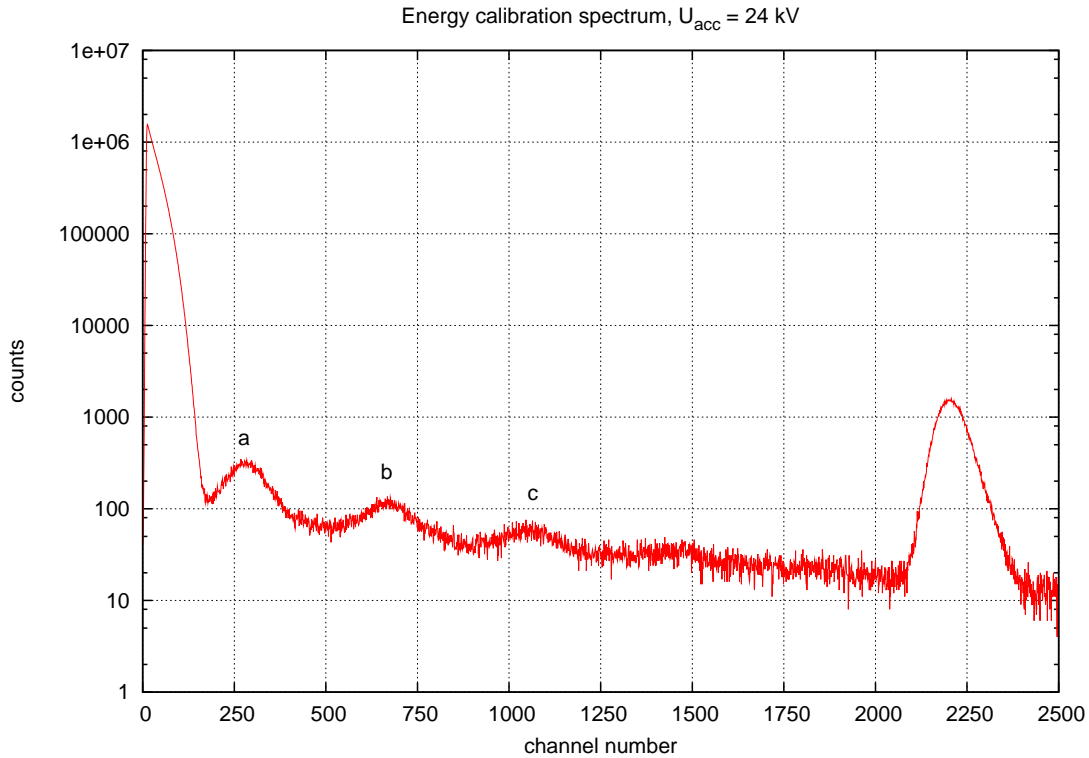


**Figure 7.8:** *The full calibration spectrum. The pulse generator peak is located at channel  $2200 \pm 10$ . Above the background edge on the left three peaks marked  $a, b, c$  are visible. They result from electrons emitted from the 24 kV flange. Events of a higher order vanish in the background.*

The fact that there are multiple peaks is the result of  $n$ -fold electron events: If  $n$  electrons hit the detector within a given time, they are no longer resolved as single events, but as one event with the total energy of these electrons. Therefore the three visible peaks marked  $a, b, c$  in figure 7.8 can be the 1-, 2- and 3-fold events or events of higher order, e.g. 2-, 3- and 4-fold events (which would imply that the single electron peak would vanish in the background to the left).

Now a technique is needed to assign these peaks to the order of the event. If that is done, the peaks can be assigned to the corresponding energies, thus making a calibration possible. For this peak identification, two different methods are used:

- The energy of the pulse generator peak can be calculated. This will be done in

the next section.

- The offset of the main amplifier/DAQ system was measured. The method and the results will be presented in section 7.3.2.

Using these results, the identification of the electron peaks and the resulting calibration will be done in section 7.3.3.

### 7.3.1 Calculation of the pulse generator peak energy

As already described in section 7.2 the pulse generator output is connected to the detector system. The energy of the peak induced by this calibration signal is approximated below.

In the normal operation of the detector, the number of electron pairs  $N_{pairs}$  created in the detector is given by

$$N_{pairs} = \frac{E_{dep}}{W_{Si}}, \quad (7.2)$$

where  $W_{Si}$  is the energy needed to create an electron/hole pair in silicon and  $E_{dep}$  the deposited energy.

Hence, the energy induced by the pulse generator can be expressed by the equivalent number of electrons:

$$E_{cal} = N_e W_{Si}. \quad (7.3)$$

This equivalent number of created electrons  $N_e$  can be calculated by the collected charge:

$$Q = N_e e \quad (7.4)$$

The charge sensitive amplifier connected to the detector diode, on which the charge is integrated, has a denoted capacitance of  $C_{det} = 0.5pF$ . Therefore with  $C = \frac{Q}{U}$  one obtains

$$E_{cal} = \frac{Q}{e} W_{Si} = \frac{CU}{e} W_{Si} \quad (7.5)$$

The voltage output of the frequency generator was measured to be  $U = (11.8 \pm 0.2)$  mV. The energy to create an electron/hole pair in silicon is  $W_{Si} = (3.65 \pm 0.01)$  eV at 300 K [Maz08]. With these values the calibration energy of the frequency generator is calculated to be  $E_{cal} = (134.4 \pm 2.6)$  keV.

### 7.3.2 Measurement of the offset of the main amplifier

The second method used for the peak identification is the measurement of the main amplifier offset. An offset has to be expected as the used main amplifier has an adjustable offset which was not calibrated to zero before the measurements.

To measure the offset, a pulse generator (not the one described above) with a spectroscopy amplifier was connected to the main amplifier. This results in two distinct peaks  $P_1$  and  $P_2$  in the energy spectrum due to the form of the signal. For a fixed pulse height (the absolute value does not matter here), the preamplifier gain was doubled, corresponding to a doubling of the pulse energy. This doubling is visible as a shift of the peak positions in the spectra. The offset of the system can be calculated without

information about the absolute height of the pulses. Offsets of  $O(P_1) = -84.0 \pm 1.2$  and  $O(P_2) = -113.0 \pm 1.2$  channels were calculated.

### 7.3.3 Calibration with 24kV electrons

The results found above are summarised in figure 7.9. Two different sets of possible peak identifications are shown:

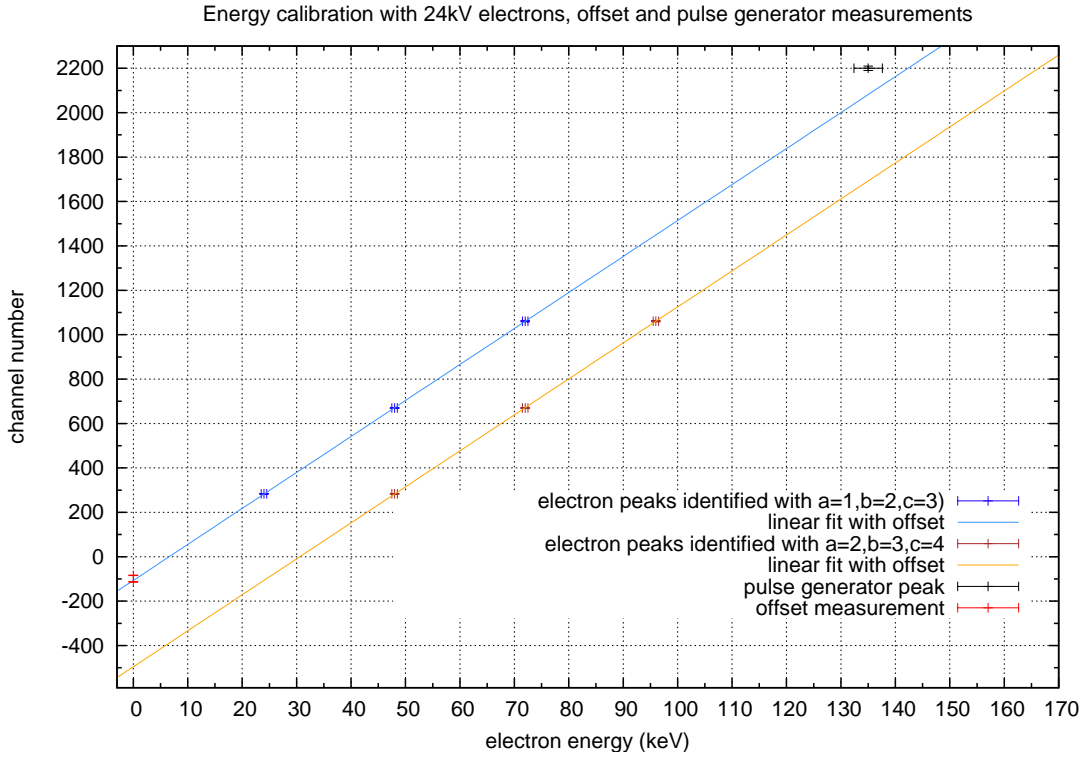


**Figure 7.9:** The results of the energy calibration as described in section 7.3.3. The  $a = 1$ ,  $b = 2$ ,  $c = 3$  case is supported by the offset and pulse generator measurements, while the  $a = 2$ ,  $b = 3$ ,  $c = 4$  case is ruled out.

- The blue set with  $a = 1$ ,  $b = 2$ ,  $c = 3$  denotes the case that peak  $a$  in the calibration spectrum is the single electron peak,  $b$  is the peak due to the 2-fold electron events and  $c$  corresponds to 3-fold events.
- The brown set named  $a = 2$ ,  $b = 3$ ,  $c = 4$  corresponds to the next possible identification that peak  $a$  is the 2-fold electron peak and so on.

Both sets have been fitted with a linear function with offset. Also shown are the results from the pulse generator and the offset measurements discussed above. Both support the  $a = 1$ ,  $b = 2$ ,  $c = 3$  case and rule out the  $a = 2$ ,  $b = 3$ ,  $c = 4$  case.

Hence, the energy calibration is done with a linear fit of the  $a = 1$ ,  $b = 2$ ,  $c = 3$  case. The resulting calibration shows that single electrons in the expected energy range of  $E_e = eU_{\text{acc}} \approx 15$  keV can be detected.

## 7.4 Measurements

As already described in section 7.2, three measurement periods were conducted.

The first two periods had the goal to find the threshold  $\Delta U_{\text{crit}}$  for the potential difference  $\Delta U_{\text{wire}}$  at which field emission starts. Therefore measurements with different  $\Delta U_{\text{wire}}$  were conducted with the regular wire/tooth setup depicted in figure 7.4(a).

For the second measurement period the wire from the first period (wire 1) was exchanged against a new one (wire 2) to exclude conditioning effects, as the first wire was also used for several test runs. This is the only difference concerning the setup. Nevertheless, as described below, the results show distinct differences.

The third measurement period featured the altered setup shown in figure 7.4(b). It serves to prove that the measured signal really originates from the subjected region at the wire: A potential difference  $\Delta U_{\text{wire}} > \Delta U_{\text{crit}}$  will be applied to this setup and since the critical point is removed in this setup, no signal should be observable.

For all measurements an acceleration voltage of  $U_{\text{acc}} = (15 \pm 0.5) \text{ kV}$  was applied. Hence, the electrons resulting from field emission between the wire and the tooth are expected to show up at  $E = e(U_{\text{acc}} + \Delta U_{\text{wire}})$  in the energy spectrum. As the expected rates for small  $\Delta U_{\text{wire}}$  are low, all measurements with  $\Delta U < 1200 \text{ V}$  were performed for several hours. The various 1200 V measurements (for different magnetic fields, see below) were performed for 10 minutes each, as the signal rate was sufficiently high and the signal showed strong conditioning effects.

### 7.4.1 First measurement period (wire 1)

In this measurement period, spectra were taken for potential differences  $\Delta U_{\text{wire}} = 0 \text{ V}, 100 \text{ V}, 200 \text{ V}, 500 \text{ V}$  and  $\Delta U_{\text{wire}} = 1200 \text{ V}$  (see figure 7.10). These measurements were all conducted with  $I_{\text{mag}} = 120 \text{ A}$  (the strongest magnetic field).

Only for  $\Delta U_{\text{wire}} = 1200 \text{ V}$  a peak in the expected energy region of 16.2 kV can be observed. Compared to the measurements with lower wire potential, the overall background for this wire potential is increased by a factor of 10 for low energies. For increasing energy, the background approximates the background for lower  $\Delta U_{\text{wire}}$  until the background levels converge at  $E \gtrsim 160 \text{ keV}$ .

For  $\Delta U_{\text{wire}} = 1200 \text{ V}$  the calibration peak shows a broadening to the right, possibly due to pile-up.

As the signal at  $\Delta U_{\text{wire}} = 1200 \text{ V}$  is strong (and therefore only 10 minutes measurement time were sufficient to see a clear signal), the magnetic field was changed a few times to test its influence on the signal. If the electrons were guided only magnetically to the detector, the signal should vanish when the magnetic field is switched off. On the other hand, if the electrical lense effect dominates, the signal should not vanish.

The results of these measurements are shown in figure 7.11. As one can see, the signal vanishes when switching off the magnetic field, while the background level drops by a factor of about 10. This is a sign for a dominating magnetic guidance of the electrons. Another effect that can be seen for the three different runs with  $I_{\text{mag}} = 120 \text{ A}$  and for the two runs with  $I_{\text{mag}} = 90 \text{ A}$  is the conditioning of the signal. There was a break of 30 minutes between runs 6 and 7, during which all potentials and the magnetic field remained the same. Conditioning effects can be seen clearly between these two runs.

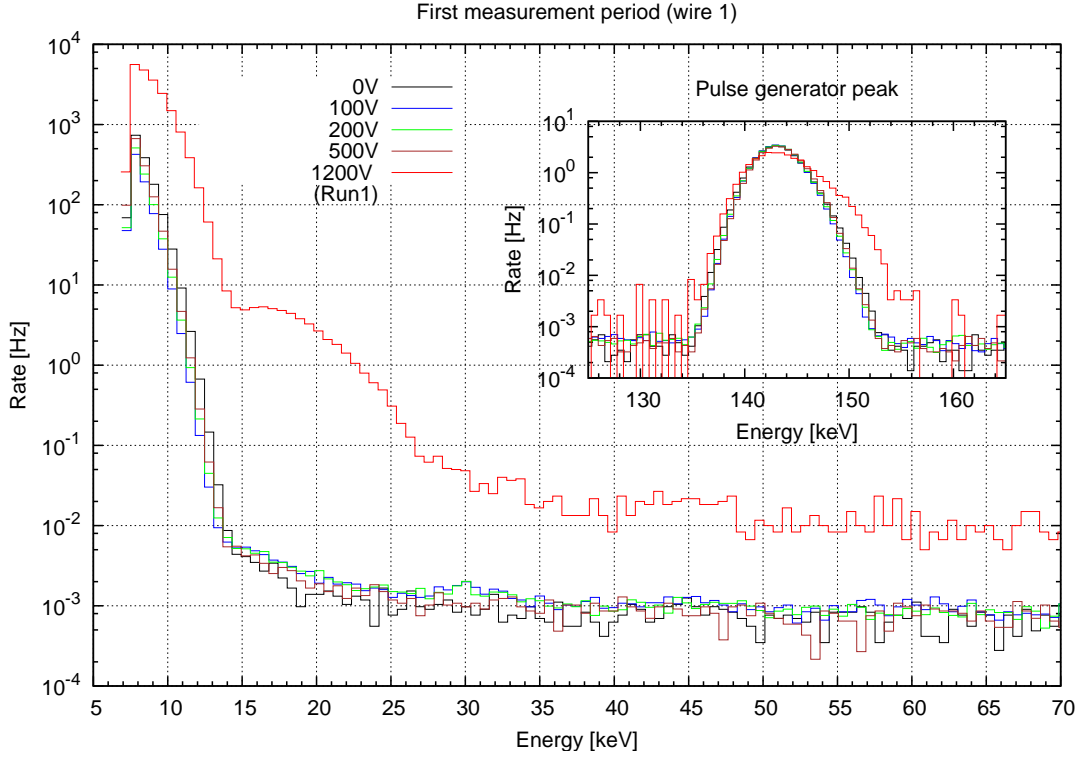


**Figure 7.10:** The spectra from the first measurement period for different  $\Delta U_{\text{wire}}$ . For all measurements the coil current was  $I_{\text{mag}} = 120$  A. Only for  $\Delta U_{\text{wire}} = 1200$  V a signal at the expected energy of  $E \approx 16.2$  keV can be seen.

## 7.4.2 Second measurement period (wire 2)

In order to confirm the results obtained in the first measurement period, the vacuum setup was opened, the wire was exchanged against a new one and the measurements were repeated. The results for different wire voltages  $\Delta U_{\text{wire}} = 0$  V, 200 V, 500 V and  $\Delta U_{\text{wire}} = 1200$  V are shown in figure 7.12.

For  $\Delta U_{\text{wire}} = 1200$  V a signal can be observed in the expected region. Smaller peaks are visible at  $E \approx 30$  keV and  $E \approx 45$  keV. As there is a strong single electron peak, these peaks can be explained by multiple electron events. For energies higher than  $E \approx 15$  keV the background level is increased for  $\Delta U_{\text{wire}} = 1200$  V and drops to the level of lower wire potentials measurements for higher energies. In contrast to the first measurement period, the background level at very low energies below  $E \approx 15$  keV remains the same, independent of  $\Delta U_{\text{wire}}$ .

An interesting effect is that also for  $\Delta U_{\text{wire}} = 0$  V small peaks can be observed at  $E \approx 30$  keV and  $E \approx 45$  keV. As no field emission at the suspected point can occur in this setup, it is assumed that this is a background effect.

The run for  $\Delta U_{\text{wire}} = 500$  V shows a bump at about 12 keV. There are three points which indicate that this is a noise effect:

- The position of this bump is significantly below  $E = 15.5$  keV, which would be

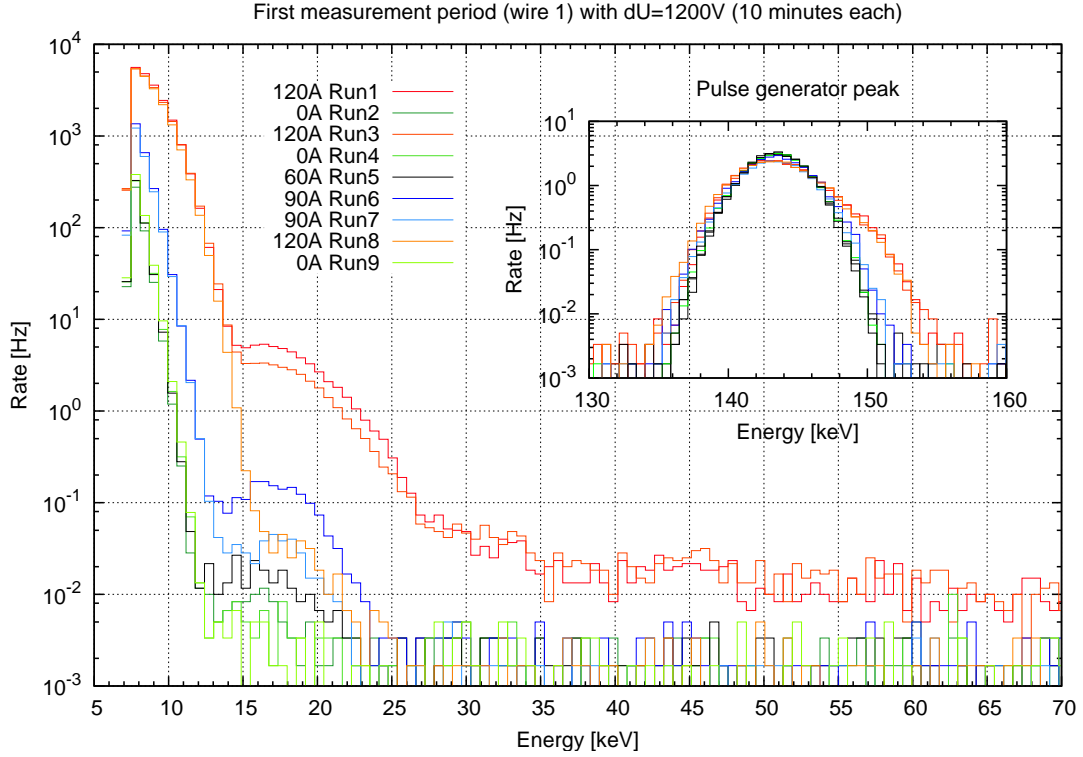


**Figure 7.11:** The spectra from the first measurement period for  $\Delta U_{\text{wire}} = 1200 \text{ V}$  and different magnetic fields. The runs are named chronologically.

the expected signal position for  $\Delta U_{\text{wire}} = 500 \text{ V}$ .

- The calibration peak shows a large broadening to both sides which is significantly larger than the broadening of the run with  $\Delta U_{\text{wire}} = 1200 \text{ V}$ .
- There is no conditioning of the signal to be found when analysing the time dependence of the spectrum as found in the clear signal runs with  $\Delta U_{\text{wire}} = 1200 \text{ V}$ <sup>6</sup>.
- The counting rate rate for very low energies  $E < 10 \text{ keV}$  (background region) is about a factor 10 above the level of the other runs, including the run for  $\Delta U_{\text{wire}} = 1200 \text{ V}$  which shows a clear signal without this characteristic.

As in the prior measurement period, different magnetic field configurations have been applied for  $\Delta U_{\text{wire}} = 1200 \text{ V}$  to check for the magnetic field dependency of this signal. The results are shown in figure 7.13. There are analogies, but also significant differences to the first measurement period.

As in the prior measurements, the signal vanishes over time due to the conditioning effects, as can be seen in the consecutive runs with  $I_{\text{mag}} = 120 \text{ A}$ .

<sup>6</sup>Actually, there is a time dependence of the whole spectrum, but it is very small (from the order of a few percent). As it affects the whole spectrum and no development of the bump can be observed, one can assume that this is no conditioning but a background effect. Similar effects are found also in other runs which did not show a signal.

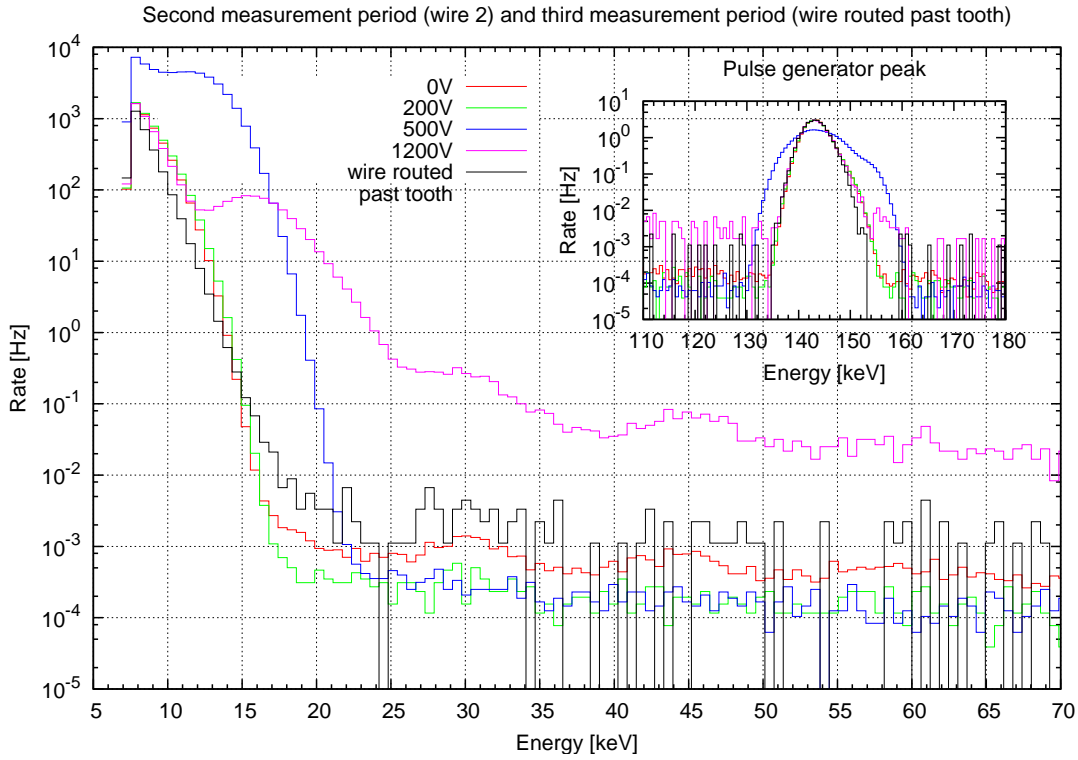


**Figure 7.12:** The spectra from the second measurement period for different  $\Delta U_{\text{wire}}$ . For all measurements the coil current was  $I_{\text{mag}} = 120$  A. The run with  $\Delta U_{\text{wire}} = 500$  V is too noisy to make any statement on field emission for this wire potential. As in the first measurement, only for  $\Delta U_{\text{wire}} = 1200$  V electrons with energies of 16.2 keV can be seen. Also shown is the result for the third measurement period (wire routed past tooth,  $\Delta U_{\text{wire}} = 1200$  V), where no signal can be observed.

There is a significant difference between the two measurement periods concerning the magnetic field dependence. While in the first period the signal drops significantly when the magnetic field is switched off, in the second period there is just a small diminishment of the signal. This can be seen best following the signal through the consecutive runs, e.g. between run 2 and 4, which are both with 120 A. The signal height of run 3 with  $I_{\text{mag}} = 0$  A should be between these signals (due to the conditioning) if there would be no magnetic field dependence. In fact the signal height is at the same level as in run 4, so it is diminished slightly relative to a scenario without any magnetic field dependency. Saying this, one also has to note that the background level of the runs with a lower magnetic field strength is significantly below the runs with  $I_{\text{mag}} = 129$  A, making the signal peaks appear much more clearly. A similar effect can be seen for the runs 5 to 6, where the rising magnetic field ( $I_{\text{mag}} = 60$  A to  $I_{\text{mag}} = 90$  A) is increasing the signal slightly despite the conditioning effect. Nevertheless, the dependence is completely different from that seen in the first measurement period, where the signal was depending crucially on the magnetic field. The results from the second measurement period support the effect of electrical lensing as the main transport

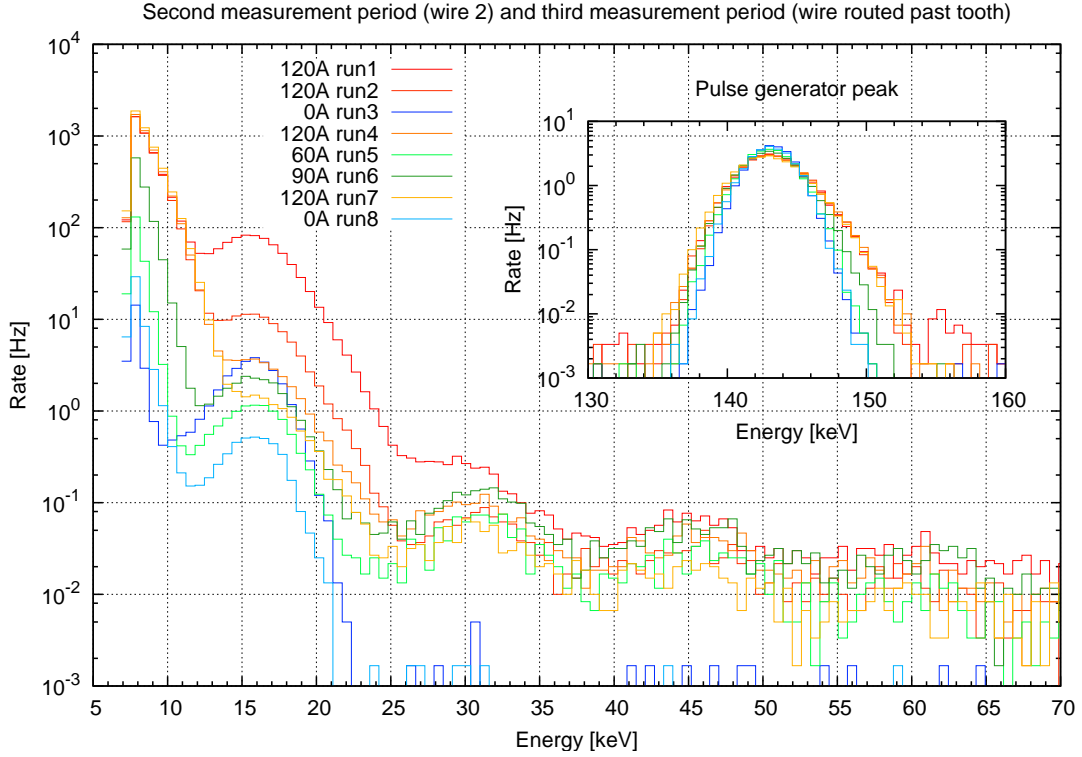


**Figure 7.13:** The spectra from the second measurement period for  $\Delta U_{\text{wire}} = 1200 \text{ V}$  and different magnetic fields. The runs are 10 minutes each and ordered chronologically. The signal at  $16.2 \text{ keV}$  can be seen clearly. It does not drop as significant as in the first measurement period when the magnetic field is turned down. Also shown is the result for the third measurement period (wire routed past tooth,  $\Delta U_{\text{wire}} = 1200 \text{ V}$ ). No signal can be seen there.

mechanism of the electrons to the detector instead of magnetic guidance as observed in the first measurement period.

### 7.4.3 Third measurement period (wire routed past tooth)

To affirm that the signals seen for  $\Delta U_{\text{wire}} = 1200 \text{ V}$  are really electrons emitted from the point where the wire is inserted into the tooth a third measurement period was performed with a wire which was not fixed at the tooth, but guided through the insulator (see figure 7.4). Hence, other sources of electrons which could possibly be generated at other points of the setup should reach the detector as before and a signal should be seen with  $\Delta U_{\text{wire}} = 1200 \text{ V}$  and  $I_{\text{mag}} = 120 \text{ A}$ . If there is no signal observed under these conditions it is shown that the signal really originates from the assumed point where the wire is mounted into the tooth. The result is also shown in figure 7.12. As one can see, there is no signal visible, the spectrum matches the ones with lower wire potentials. Hence it was shown the the observed signals really are electrons originating from the point where the wire is mounted into the tooth.

## 7.5 Analysis and results

In the measurements presented above it was shown that the setup is indeed capable of detecting single electrons with energies as expected for electrons resulting from field emission. A clear signal in the expected energy region was observable only for  $\Delta U_{\text{wire}} = 1200 \text{ V}$  in both measurement periods. It was shown that this signal originates from the expected point at the wire.

Using eq. 7.1 and the assumptions described in section 7.1, for  $\Delta U_{\text{wire}} = 1200 \text{ V}$  an electric field strength of about  $6000 \text{ kV/m}$  can be calculated. As stated in section 3.2, the occurrence of field emission at such field strengths is expected.

For the projected wire potential of  $\Delta U_{\text{wire}} = 100 \text{ V}$  a field strength of about  $500 \text{ kV/m}$  has been calculated using eq. 7.1. This calculation did not take into account surface irregularities and the edges in the tooth drilling. Hence, for this wire potential field emission may or may not occur according to the considerations taken in section 3.2.

As no clear signal was observed for  $\Delta U_{\text{wire}} = 100 \text{ V}$  in the measurements, the next sections will discuss the background properties in more detail and derive an upper limit on the signal rate which could be detected with the setup.

### 7.5.1 Discussion of the background properties

The expected signal energy is close to the edge of the low energy background. Hence, during all measurements the reduction of background effects to a sufficient level was challenging.

The first and second measurement period have shown significant differences that were already described in the last section. To further illustrate the background characteristics of the two measurement periods, the counting rate ratios

$$r_1(\alpha) = c(\Delta U_{\text{wire}} = \alpha)/c(\Delta U_{\text{wire}} = 0 \text{ V}) \quad (7.6)$$

with  $\alpha = 100 \text{ V}, 200 \text{ V}, 500 \text{ V}, 1200 \text{ V}$  for wire 1 and

$$r_2(\beta) = c(\Delta U_{\text{wire}} = \beta)/c(\Delta U_{\text{wire}} = 0 \text{ V}) \quad (7.7)$$

with  $\beta = 200 \text{ V}, 500 \text{ V}, 1200 \text{ V}$  for wire 2 are discussed now.

#### Measurement period 1 (wire 1)

The results for  $r_1(100 \text{ V})$  are shown in 7.14. For low energies with  $E < 13 \text{ keV}$ , the background level is high, leading to small relative uncertainties. The ratio in this region decreases continuously for higher energies until it rises abrupt at an energy of  $E \approx 14 \text{ keV}$ . This step is caused by the transition from the high background level to the region with lower counting rates.

For energies  $E > 15 \text{ keV}$  the ratio  $r_1(100 \text{ V})$  stays constant, forming a plateau with  $r_1(100 \text{ V}) \approx 1.3$ . Thus, the background level in this energy region rises is increased for  $\Delta U_{\text{wire}}$  relative to  $\Delta U_{\text{wire}}$ . This is consistent with the measurements for higher wire potentials of  $\Delta U_{\text{wire}} = 200 \text{ V}$  and  $\Delta U_{\text{wire}} = 500 \text{ V}$ , as can be seen in figure 7.15. For these wire potentials the characteristic of  $r_1$  is the same as for  $\Delta U_{\text{wire}} = 100 \text{ V}$ .

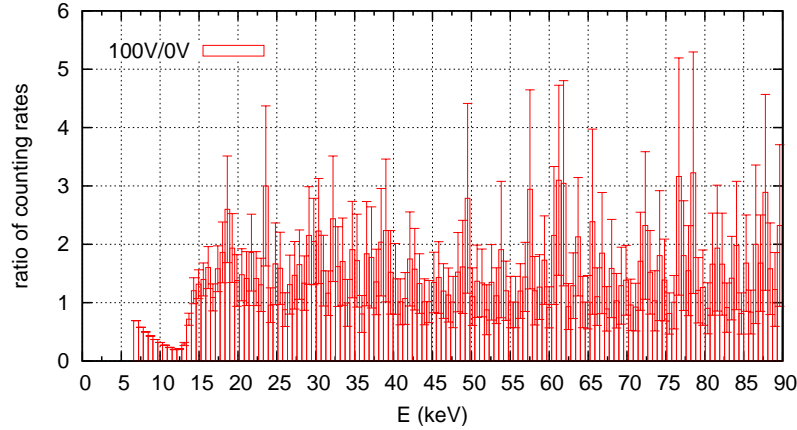


**Figure 7.14:** The ratio  $r_1 = \frac{c(100\text{V})}{c(0\text{V})}$  of the counting rates for the first measurement period (wire1).

As the expected mean value of a signal peak is  $E = 15\text{ keV} + e\Delta U_{\text{wire}}$ , at least the right half of a possible signal peak is located in the region of the plateau and therefore should be observable. For the potentials  $\Delta U_{\text{wire}} = 100\text{ V}$ ,  $\Delta U_{\text{wire}} = 200\text{ V}$  and  $\Delta U_{\text{wire}} = 500\text{ V}$  no signal can be observed. An upper limit for a possible signal will be derived in the section 7.5.2.

For  $\Delta U_{\text{wire}} = 1200\text{ V}$  a clear signal was visible in both measurement periods. Figure 7.16 shows the ratio  $c(\Delta U_{\text{wire}} = 1200\text{ V})/c(\Delta U_{\text{wire}} = 0\text{ V})$  for both measurement periods. The peak structure is clearly visible.

### Measurement period 2 (wire 2)

The characteristics of the ratio  $r_2$  for the second measurement period are completely different from the properties of measurement period 1 discussed above (see figure 7.17). In the region of the low energy background, the ratio rises up to about  $r_2 = 2$  for increasing energies. For energies above about 16 keV it drops abruptly to a plateau with a ratio of  $r_2 \approx 0.3$ . For  $\Delta U_{\text{wire}} = 500\text{ V}$  a similar ratio can be found for the plateau region. This implies that the counting rate dropped significantly for an increased wire potential  $\Delta U_{\text{wire}}$ . This is not expected and was not observed in the first measurement period.

The resulting step in  $r_2$  with a sharp edge at  $15\text{ keV} \leq E \leq 17\text{ keV}$  is an artifact of this background characteristic and not a signal peak. The structure of the step is distinct from the shape and width of the verified signal peaks for  $\Delta U_{\text{wire}} = 1200\text{ V}$  shown in figure 7.16.

The measurements of the second measurement period show a complicated characteristic which is not understood completely. The edge of the step resulting from the transition from the low energy background to the plateau region ranges up to the energy region of an expected signal peak. Thus, in contrast to the first measurement period, this step effect cannot be compensated by taking into account only the right half of the peak.

The further analysis of the results is conducted only with the data of the first measure-

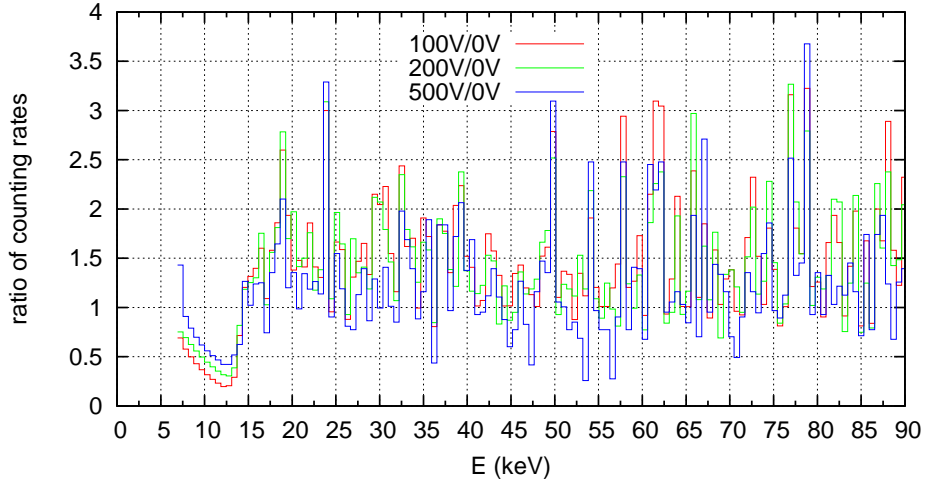


**Figure 7.15:** The ratios  $r_1(\alpha)$  for  $\alpha = 100\text{ V}, 200\text{ V}, 500\text{ V}$  where no signal can be observed (First measurement period).

ment period.

### 7.5.2 Derivation of upper limits

The spectrum can be divided into a signal window  $\Delta E_s$  where the electrons resulting from the field emission are expected (denoted by the index  $s$ ) and background regions  $\Delta E_b$  where no or a very weak signal is expected (denoted by the index  $b$ ).

The signal range  $\Delta E_s$  to measure the counting rate rate is determined as follows:

- The width of the energy window is given by the width  $\sigma = (1.77 \pm 0.11)\text{ keV}$  of the peak found for  $\Delta U_{\text{wire}} = 1200\text{ V}$ .
- The central value of the expected peak is  $E_{cv} = 15\text{ keV} + e\Delta U_{\text{wire}}$ .
- Only the right half of the peak is analysed as the left half is located in the edge of the low energy background already.

Thus, the energy window  $\Delta E_s$  has a range of  $E_{cv} < E < E_{cv} + \sigma$ . Hence, it covers  $1\sigma$  of the whole peak energy range.

The background region  $\Delta E_b$  where no signal is expected ranges from  $E = 40\text{ keV}$  (thus excluding the 2-fold electron peak at about  $30\text{ keV}$ ) up to  $E = 110\text{ keV}$  (below the region of the pulse generator peak).

The ratio of the counting rates  $c_b(0\text{ V})$  and  $c_b(100\text{ V})$  in the background region  $\Delta E_b$  is given by

$$R = \frac{c_b(100\text{ V})}{c_b(0\text{ V})} \quad (7.8)$$

This ratio is calculated for several intervals in the background region  $\Delta E_b$ . From that, the expected ratio and hence the expected counting rate  $c_{s,\text{exp}}(100\text{ V})$  can be calculated for the signal range  $\Delta E_b$  assuming that no signal is present. It is given by

$$c_{s,\text{exp}}(100\text{ V}) = R \cdot c_s(0\text{ V}). \quad (7.9)$$

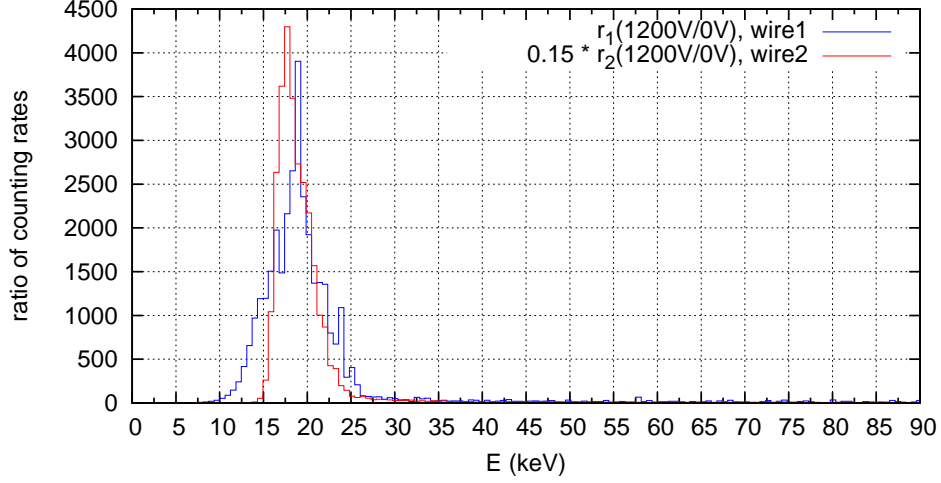


**Figure 7.16:** The counting rate ratio  $r_1(1200\text{ V})$  for the first and  $r_2(1200\text{ V})$  for the second measurement period. The ratio  $r_2$  has been scaled for better comparison.

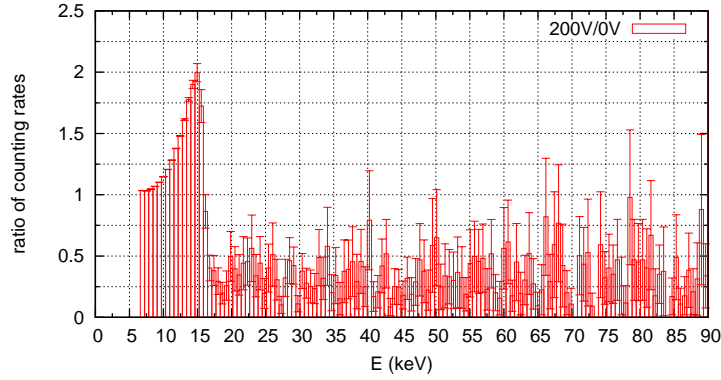


**Figure 7.17:** The ratio  $r_2 = \frac{c(200\text{ V})}{c(0\text{ V})}$  of the counting rates for the second measurement period (wire2).

This rate must be compared to the measured counting rate  $c_s(100\text{ V})$ . If they match within their error margins it can be assumed that no signal is present.

With a fitted ratio of  $R(100\text{ V}/0\text{ V}) = 1.33 \pm 0.08$  for  $\Delta E_s$ , the expected rate for  $\Delta U_{\text{wire}} = 100\text{ V}$  is calculated to  $c_{s,\text{exp}}(100\text{ V}) = 11.30 \pm 1.69\text{ mHz}$ . This agrees with the measured counting rate of  $c_s(100\text{ V}) = 12.65 \pm 0.48\text{ mHz}$  within  $0.8\sigma$ .

The upper limit  $c_u$  of a possible signal can be calculated by

$$c_u = k_\alpha \sigma_u. \quad (7.10)$$

Here  $k_\alpha$  denotes the quantile of the given confidence level  $\alpha$  and

$$\sigma_u = \sqrt{(\Delta c_{s,\text{exp}}(100\text{ V}))^2 + (\Delta c_s(100\text{ V}))^2} \quad (7.11)$$

takes into account the absolute uncertainties of the measured and expected counting rate in the whole expected signal range. As mentioned earlier, the values denoted above

have been calculated based on the counting rates for the fraction of  $1\sigma$  of the whole peak energy range. Thus, the measured uncertainties have to be scaled up by a factor of  $\frac{1}{\sigma} \approx \frac{1}{34.1\%}$ .

The quantile for 95% C.L. is  $k_{95\%} \approx 1.6449$ . This leads to an upper limit of  $c_u \leq 5.2$  mHz at 95% confidence level for a possible signal at  $\Delta U_{\text{wire}} = 100$  V.

In the same way as explained above limits for the higher potentials can be derived.

For  $\Delta U_{\text{wire}} = 200$  V the expected and measured counting rates agree within  $0.7\sigma$ . The upper limit on the signal rate is  $c_u \leq 5.8$  mHz with a C.L. of 95%.

For  $\Delta U_{\text{wire}} = 500$  V an agreement between the expected and measured counting rate of  $0.1\sigma$  is found. The upper limit on the signal rate is  $c_u \leq 6.4$  mHz at 95% C.L..

### 7.5.3 Implications for the KATRIN main spectrometer

From the results of the measurements the implications for the KATRIN experiment shall be approximated. This can be just a rough estimate as several factors of the calculation are not known.

The upper limit on the measured signal rate given above does not take into account the efficiency of the setup. This efficiency should be high due to the magnetic fields guiding the electrons to the detector. A detection efficiency of 10% will be assumed.

The wire electrode of the main spectrometer consists of 23440 wires and therefore twice as much wire mountings. The projected potential difference for most of the wire electrode modules is  $\Delta U_{\text{wire}} = 100$  V. To calculate the upper limit for the total rate of electrons emitted by field emission it will be assumed that the upper limit found for  $\Delta U_{\text{wire}} = 100$  V holds true for all wire mountings, although for the steep cone and cylinder part lower rates are expected because of the less critical geometry and (for the steep cone part) a lower wire potential  $\Delta U_{\text{wire}}$ . This leads to an upper limit on the total rate of emitted electrons of about 250 Hz.

The fraction of electrons reaching the detector is reduced significantly by the magnetic shielding properties of the main spectrometer (see section 4.6). Since the wire electrode is located relatively close to the vessel hull, a shielding of  $\varepsilon = 10^{-5}$  is assumed. This leads to an upper limit of about 3 mHz for the rate of electrons induced by field emission reaching the detector.

To reach the aimed sensitivity of the KATRIN experiment, the upper limit accepted for the total background rate is 10 mHz. Hence the approximated upper limit for the studied wire mounting is of the order of the required limit for the total background rate of the main spectrometer.



## 8 Summary and outlook

The KATRIN experiment aims to determine the absolute mass of the electron anti-neutrino by a precise measurement of the endpoint region of the tritium  $\beta$  spectrum. Reaching a sensitivity of  $0.2 \text{ eV}/c^2$  at 90% confidence level it will improve the sensitivity of direct neutrino mass measurements by one order of magnitude.

The spectrum is analysed using a MAC-E filter, a spectrometer which is based on magnetic collimation and the use of an electric retarding potential. The main spectrometer is currently the biggest of its kind. It features an inner electrode system for background suppression as well as to allow a better adjustment of the electromagnetic properties of the spectrometer. The electrode system consists of wire modules with one or two wire layers and, in the flange region, of full metal electrodes.

The design of the electrode system, especially in the steep cone and flange regions, has a big impact on the transmission and background properties. Since the space in these regions is limited, the design has to be a compromise between several demands like the avoidance of Penning traps, adequate transmission properties and not too high electric field strengths. Additionally, the design has to be mechanically feasible.

Several parameters of the electrode system in the steep cone and flange regions have been optimised with respect to the demands mentioned above. The resulting proposed setup avoids Penning traps with a critical depths, assures sufficient transmission properties and keeps the electric fieldstrength as low as possible.

Although the design of the steep cone region is largely finished, there are still topics which need attention.

The mechanical implementation of the design of the shielding electrode is challenging. A mockup is currently under construction to test the feasibility of the planned design. The ground electrode has been optimised retaining a safety margin to the fluxtube which includes tolerances for the mechanical setup. Limits for the displacement of the fluxtube due to tilted magnets have not been calculated up to now. These limits have to be taken into account to be sure that the whole projected fluxtube is transmitted.

To improve background suppression, there is a potential difference  $\Delta U_{\text{wire}}$  between the electrode wires of the inner wire layer and the supporting frame structure. The resulting high electric field strengths at the mounting positions give rise to the possibility of field emission at these critical points.

An experimental study was conducted to investigate the conditions under which field emission occurs at these critical points. It was shown that the setup is capable of detecting electrons with the expected energies, as for a potential difference of  $\Delta U_{\text{wire}} = 1200 \text{ V}$ , which is significantly larger than the intended potential difference of  $\Delta U_{\text{wire}} = 100 \text{ V}$ , a signal with the expected energy was found. It was also shown that the detected electrons are originating from the suspected critical point. No field emission could be detected for the intended wire potential difference of  $\Delta U_{\text{wire}} = 100 \text{ V}$ .

Another component of the wire electrode modules where field emission might constitute a problem are the high voltage connectors that distribute the high voltage to the adjacent modules and the inner wire layer. As the setup has shown the capability to study field emission, this setup can also be used to investigate possible field emission at this component.

## A Technical drawings and device type numbers

**Table A.1:** *Type numbers of devices used in the field emission test experiment.*

Si-Pin diode	<i>Hamamatsu S3590-06</i>
Detector power supply	<i>ISEG NHQ224M</i>
Preamplifier	<i>AMPTEC CoolFET A250CF</i>
Spectroscopy amplifier	<i>Ortec 576</i>
Power supplies for magnetic field coils	<i>DELTA ELECTRONICS SM15-200D</i>
Power supply for $\Delta U_{wire}$	<i>Ortec 456</i>
Power supply for $U_{acc}$	<i>Brandenburg alpha series</i>
Pulse generator used in the measurements	<i>BNC PB-4</i>
Pulse generator used for offset calibration	<i>Ortec 419</i>
Amplifier used for offset calibration	<i>Ortec 451</i>

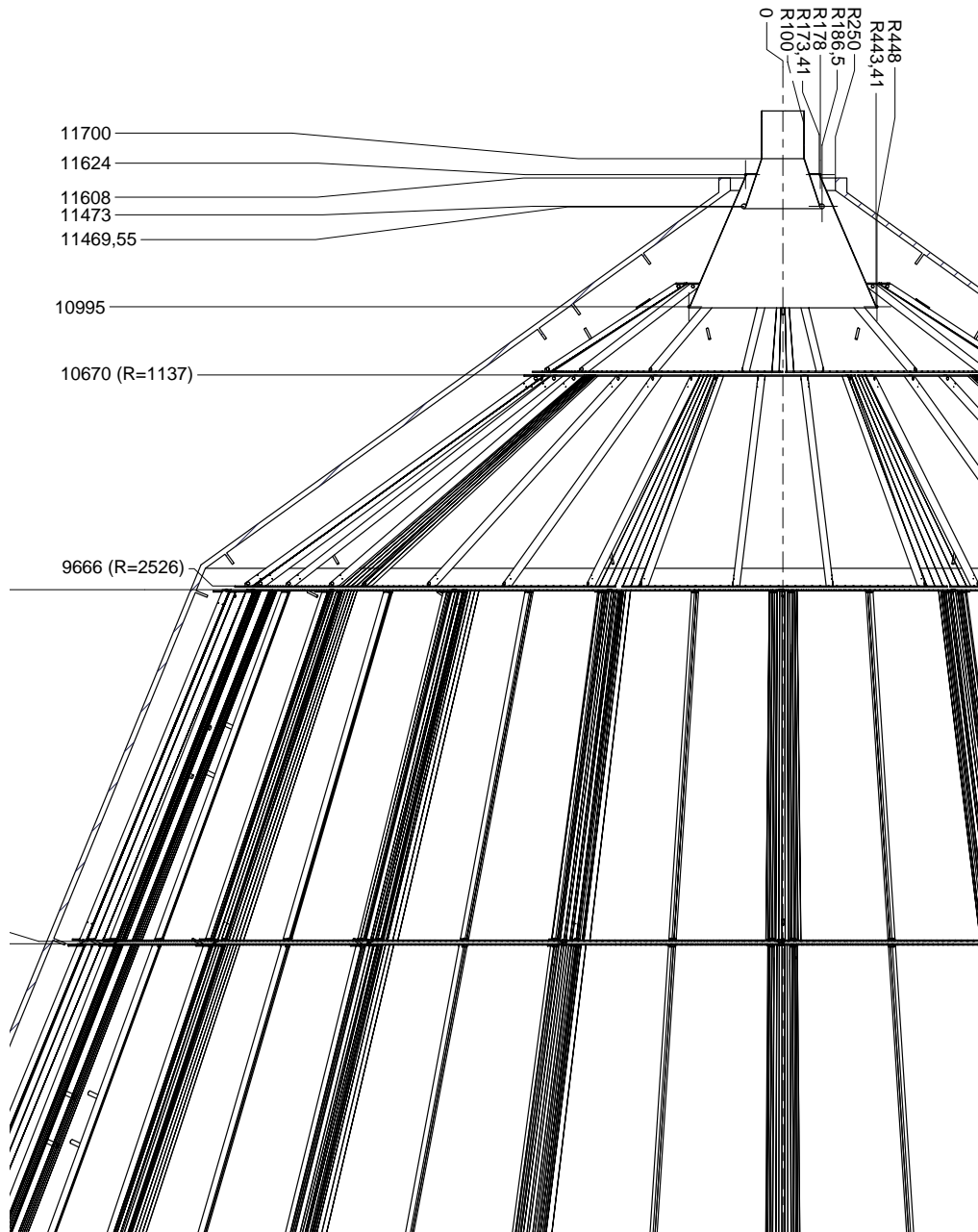
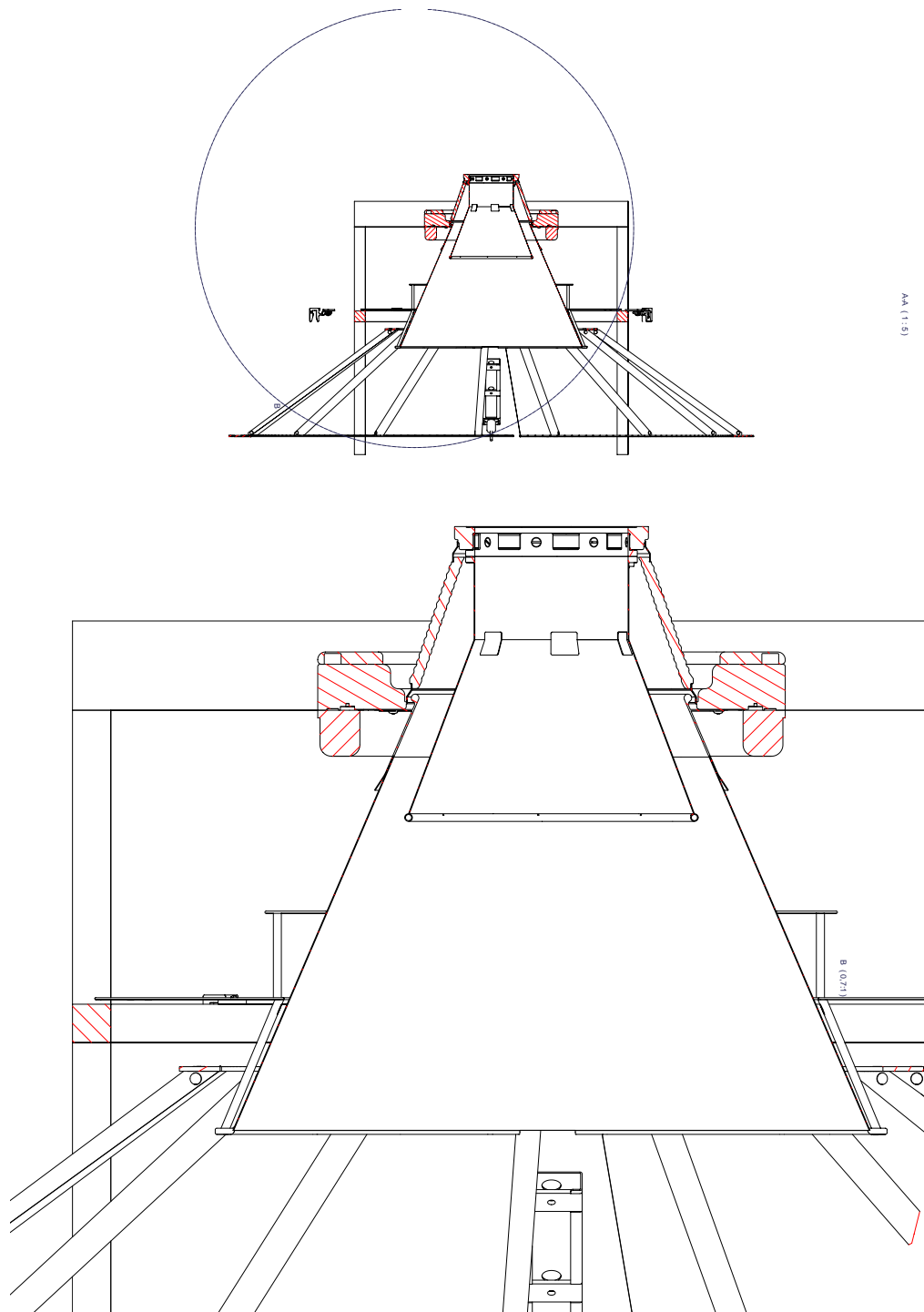
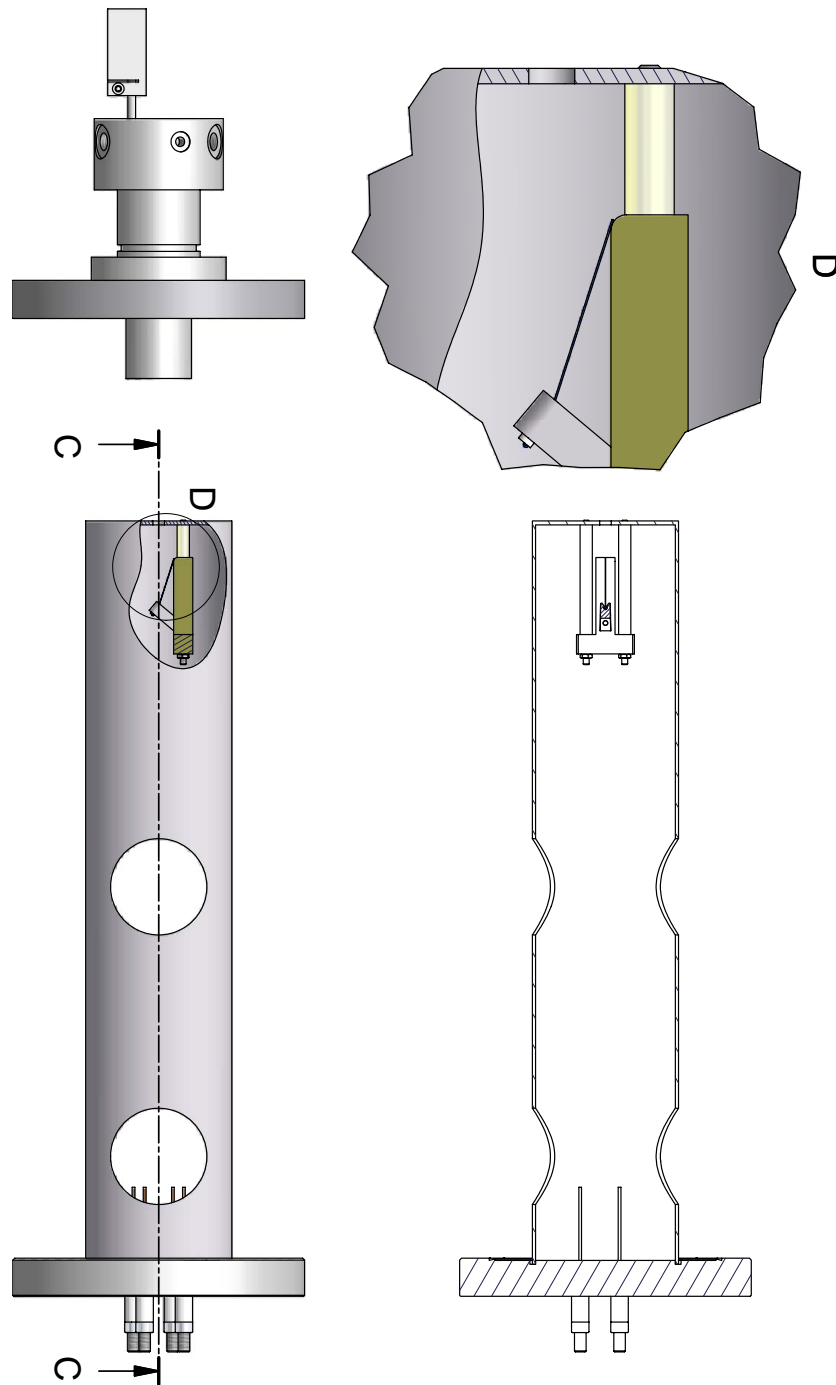


Figure A.1: CAD drawing of the steep cone setup proposed in chapter 6



**Figure A.2:** CAD drawing of a possible shielding electrode setup as described in section 6.2.1. The electrode will be divided to be mountable through the flange. Drawing from S. Lichter (FZ Karlsruhe)



**Figure A.3:** CAD drawing of the test setup build to rule out field emission as described in chapter 7. The surrounding vacuum setup is suppressed.

## B Proposed geometry file

```
<?xml version="1.0" ?>
<mainspec>
  <tank>
    <file>input_vessel_shielding_122007/inputvessel+30p0mm.dat</file>
    <fullconefile>fullcone.dat</fullconefile>
    <gap>0.150000</gap>
    <scale>1</scale>
    <power>2.000000</power>
    <nrot>1200</nrot>
  </tank>
  <tooth>
    <headfile>tooth_head.dat</headfile>
    <centerfile>tooth.dat</centerfile>
    <basefile>tooth_base.dat</basefile>
    <radius>4.680000</radius>
    <z>-0.889500</z>
    <nrot>1200</nrot>
  </tooth>
  <wires>
    <innerthickness>0.000200</innerthickness>
    <outerthickness>0.000300</outerthickness>
    <layerdelta>0.070000</layerdelta>
    <discretise>1</discretise>
    <scale>45</scale>
    <power>2.000000</power>
  </wires>
  <cylinder>
    <modules>20</modules>
    <wiresmodule>60</wiresmodule>
    <modulegap>0.012000</modulegap>
    <innerwirepotential>-18600.000000</innerwirepotential>
    <outerwirepotential>-18500.000000</outerwirepotential>
    <caps>1</caps>
    <capposition>0.008000</capposition>
    <capwidth>0.020000</capwidth>
    <capgap>0.000000</capgap>
    <capdiscretisationazimuthal>5</capdiscretisationazimuthal>
    <capdiscretisationaxial>4</capdiscretisationaxial>
    <cappotential>-18600.000000</cappotential>
  </cylinder>
```

```

<bigcone>
  <modules>20</modules>
  <wiresmodule1>52</wiresmodule1>
  <wiresmodule2>42</wiresmodule2>
  <wiresmodule3>34</wiresmodule3>
  <modulegap>0.018000</modulegap>
  <innerwirepotential1>-18600.000000</innerwirepotential1>
  <innerwirepotential2>-18600.000000</innerwirepotential2>
  <innerwirepotential3>-18600.000000</innerwirepotential3>
  <outerwirepotential1>-18500.000000</outerwirepotential1>
  <outerwirepotential2>-18500.000000</outerwirepotential2>
  <outerwirepotential3>-18500.000000</outerwirepotential3>
  <real_positions>1</real_positions>
  <capposition>0.008000</capposition>
  <capwidth>0.025000</capwidth>
  <capgap>0.015000</capgap>
  <capdiscretisationazimuthal>5</capdiscretisationazimuthal>
  <capdiscretisationaxial>1</capdiscretisationaxial>
  <cappotential>-18600.000000</cappotential>
</bigcone>
<steep_cone>
  <modules>10</modules>
  <wiresmodule>40</wiresmodule>
  <innerwirepotential>-18560.000000</innerwirepotential>
  <ringwidth>0.006000</ringwidth>
  <ringheight>0.040000</ringheight>
  <ringpotential>-18500.000000</ringpotential>
  <wirethickness>0.000200</wirethickness>
  <cone03_zpos>10.665300</cone03_zpos>
  <cone03_rpos>1.137000</cone03_rpos>
  <cone03_z1pos>9.664700</cone03_z1pos>
  <cone03_r1pos>2.526000</cone03_r1pos>
  <zgap_steepconeval>0.022000</zgap_steepconeval>
</steep_cone>
<fullcone>
  <wires>200</wires>
  <ringheight>0.040000</ringheight>
  <ringwidth>0.006000</ringwidth>
  <ringpotential>-18400.000000</ringpotential>
  <wirepotential>-18420.000000</wirepotential>
  <wirethickness>0.000200</wirethickness>
  <geometry02>0</geometry02>
  <cone02_zpos>11.103300</cone02_zpos>
  <cone02_rpos>0.460000</cone02_rpos>
  <cone02_z1pos>10.686700</cone02_z1pos>
  <cone02_r1pos>1.106500</cone02_r1pos>
</fullcone>

```

```
<ground>
  <sh_use_check>1</sh_use_check>
  <sh_r1_spin>0.448000</sh_r1_spin>
  <sh_r2_spin>0.178000</sh_r2_spin>
  <sh_z1_spin>10.995000</sh_z1_spin>
  <sh_z2_spin>11.624000</sh_z2_spin>
  <sh_rad1_spin>0.005000</sh_rad1_spin>
  <sh_rad2_spin>0.005000</sh_rad2_spin>
  <sh_gap_spin>0.050000</sh_gap_spin>
  <sh_scale_spin>100.000000</sh_scale_spin>
  <sh_power_spin>2.000000</sh_power_spin>
  <sh_cdis_spin>200.000000</sh_cdis_spin>
  <sh_potential_spin>-18400.000000</sh_potential_spin>
  <gr_use_check>1</gr_use_check>
  <gr_r1_spin>0.176050</gr_r1_spin>
  <gr_r2_spin>0.100000</gr_r2_spin>
  <gr_z1_spin>11.469550</gr_z1_spin>
  <gr_z2_spin>13.000000</gr_z2_spin>
  <gr_crad_spin>0.011000</gr_crad_spin>
  <gr_scale_spin_i>30.000000</gr_scale_spin_i>
  <gr_power_spin_i>2.000000</gr_power_spin_i>
  <gr_scale_spin_o>30.000000</gr_scale_spin_o>
  <gr_power_spin_o>2.000000</gr_power_spin_o>
  <gr_cdis_spin>200.000000</gr_cdis_spin>
  <gr_kink_spin>11.700000</gr_kink_spin>
  <global_ground_check>0</global_ground_check>
</ground>
<cprofiles>
  <profiles_check>0</profiles_check>
  <cylinder_z>3</cylinder_z>
  <cylinder_phi>3</cylinder_phi>
  <cylinder_power>2.000000</cylinder_power>
  <cylinder_potential>-18500.000000</cylinder_potential>
</cprofiles>
</mainspec>
```



# List of Figures

2.1	Transition probability for $\bar{\nu}_e \rightarrow \bar{\nu}_e$ . . . . .	6
2.2	Tritium beta decay spectrum for different neutrino masses . . . . .	8
3.1	Schematic view of Penning traps. . . . .	13
4.1	Schematic view of the KATRIN MAC-E filter . . . . .	16
4.2	Analytic transmission function . . . . .	19
4.3	Electric potential depression and magnetic field depression . . . . .	20
4.4	MC simulation of transmission function . . . . .	21
4.5	Possible traps indicated by $E_{\parallel}$ . . . . .	23
4.6	Background suppression with a wire electrode . . . . .	24
4.7	Dual layer wire electrode . . . . .	24
5.1	KATRINoverview . . . . .	25
5.2	KATRIN detector scheme . . . . .	28
5.3	Modular setup of the inner electrode for the main spectrometer . . . . .	29
5.4	Schematic view of the electrode geometry . . . . .	30
5.5	Wire mountings . . . . .	31
5.6	Drawing and picture of a dual wire layer electrode module . . . . .	32
5.7	Drawing of a steep cone electrode mounting ring . . . . .	32
5.8	Drawing of a the cylinder module caps . . . . .	33
6.1	Illustration to the Biot-Savart law . . . . .	36
6.2	Illustration to source points and convergence radius . . . . .	37
6.3	Example of electrode discretisation . . . . .	38
6.4	Scheme of simulation tools . . . . .	41
6.5	Overview of the steep cone of the main spectrometer . . . . .	43
6.6	Shielding electrode endbulge designs . . . . .	44
6.7	Fluxtube in the flange region . . . . .	46
6.8	El. field strength depending on ground electrode parameters . . . . .	47
6.9	Longitudinal energy for different ground electrode lengths . . . . .	48
6.10	Max. El. field strength depending on the ground electrode endbulge radius	50
6.11	Depth of the Penning trap at the end of the shielding electrode. . . . .	51
6.12	Relative positioning of ring 02 and shielding electrode . . . . .	52
6.13	Penning trap at shielding electrode due to a too steep angle . . . . .	54
6.14	Mounting position of the shielding electrode / ring 02 system . . . . .	56
6.15	Penning trap at ring 02 . . . . .	57
6.16	Penning trap depths depending on ring 02 potential . . . . .	58
6.17	Transmission properties for different length of the shielding electrode . .	60

6.18	Trap depth at shielding electrode and ring 02 for different setups . . . . .	61
6.19	Magnetic field lines depending on ring 02 comb potential . . . . .	63
6.20	Magnetic field lines at ring 03 . . . . .	64
6.21	Penning traps at ring 03 . . . . .	66
7.1	Wire mounting position . . . . .	70
7.2	Illustration to the field strength calculation . . . . .	71
7.3	Overview of field emission test setup . . . . .	72
7.4	Detailed setup . . . . .	73
7.5	Pictures of the inner cylinder setup . . . . .	74
7.6	Diagram of the oscillation suppression circuit . . . . .	75
7.7	Picture of the field emission test setup . . . . .	76
7.8	Calibration spectrum . . . . .	77
7.9	The 24kV electron calibration . . . . .	79
7.10	First measurement period spectra . . . . .	81
7.11	First measurement period spectra for 1200 V . . . . .	82
7.12	Second measurement period spectra . . . . .	83
7.13	Second measurement period spectra for 1200 V . . . . .	84
7.14	Signal ratios for 100 V for wire 1 . . . . .	86
7.15	Signal ratios for the first measurement period . . . . .	87
7.16	Signal ratios for 1200 V . . . . .	88
7.17	Signal ratios for the second measurement period . . . . .	88
A.1	CAD drawing of proposed steep cone setup . . . . .	94
A.2	CAD drawing of the shielding electrode . . . . .	95
A.3	CAD drawing of the field emission test setup . . . . .	96

# Bibliography

- [Aha05] B. Aharmim et al., Phys. Rev. C **72** (2005)
- [Ahn06] M. H. Ahn et al. (K2K Collaboration), Phys. Rev. D **74**, 072003 (2006),  
arXiv:hep-ex/0606032v3
- [Alt03] C. Weinheimer, Laboratory Limits on Neutrino Masses,  
in: G. Altarelli and K. Winter (Eds.), Neutrino Mass, Springer, 2003
- [Arl09] H. Arlinghaus, Diploma thesis (in preparation)  
Institut für Kernphysik, Westfälische Wilhelms-Universität Münster, 2009
- [Cha14] J. Chadwick, Verh. d. Deutsch. Phys. Ges. 16 (1914) 383
- [CPO] CPO - Charged Particle Optics Software, homepage [simion.com/cpo/](http://simion.com/cpo/)
- [Dun07] J. Dunmore, KATRIN internal document, 2007  
BSCW: Review of Detector Design SUMMER 07
- [Fer34] E. Fermi, Z. Phys. 88 (1934) 161 - 177
- [Fow28] R. H. Fowler, F. R. S. and Dr. L. Nordheim  
Proc. Roy. Soc. London. **119** (1928) 173 - 181
- [Fuk98] Y. Fukuda et al. (Super-Kamiokande Collaboration), Phys. Rev. Lett **81** (1998)  
1562, hep-ex/9807003
- [Geb07] A. Gebel, Diploma thesis  
Institut für Kernphysik, Westfälische Wilhelms-Universität Münster, 2007
- [Glu04] F. Glück, KATRIN internal document, 2004  
BSCW: EMD - Programs - electric fields
- [Glu05] F. Glück, KATRIN internal document, 2005  
BSCW: EMD - Background
- [Glu06a] F. Glück, KATRIN internal document, 2006  
BSCW: EMD - Programs - magnetic fields
- [Hug08] K. Hugenberg, Diploma thesis  
Institut für Kernphysik, Westfälische Wilhelms-Universität Münster, 2008
- [Hoc08] F. Hochschulz, Diploma thesis  
Institut für Kernphysik, Westfälische Wilhelms-Universität Münster, 2008

- [Kam05] The KamLAND collaboration, *Phys. Rev. Lett.* **94** 081801 (2005),  
hep-ex/0406035v3
- [KAT04] The KATRIN collaboration, KATRIN Design Report 2004  
FZKA Scientific Report 7090
- [KAT06] Komitee für Astroteilchenphysik (KAT), 2006  
Kosmische Spurensuche - Astroteilchenphysik in Deutschland
- [KRA05] Ch. Kraus, B. Bornschein, L. Bornschein, J. Bonn, B. Flatt, A. Kovalik, B.  
Ostrick, E.W. Otten, J.P. Schall, Th. Tümmler, Ch. Weinheimer, *Eur. Phys. J. C*  
40 (2005) 447
- [Les06] J. Lesgourgues and S. Pastor, *Massive neutrinos and cosmology*, *Phys. Rep.*  
429 (2006) 307
- [Lob03] V.M. Lobashev, *Nucl. Phys. A* **719** 153c - 163c
- [MAR06] MARE - Microcalorimeter Arrays for a Rhenium Experiment, proposal, 2006
- [Maz08] M.N. Mazziotta, *Nucl. Instr. Meth. A*584 (2008) 436
- [Nobel02] nobelprize.org, The Nobel Prize in Physics 2002
- [Nol04] W. Nolting, *Grundkurs Theoretische Physik 3*, Springer Verlag, 2004
- [Ott08] E.W. Otten, C. Weinheimer, *Rep. Prog. Phys* **71** (2008) 086201 (36pp) Reports  
on progress in physics: Neutrino mass limit from tritium  $\beta$  decay
- [Pau30] W. Pauli, *Collected Scientific Papers*  
Eds. Kronig & Weisskopf, Vol 2, 1316 - 1317
- [Pyt] Python programming language, homepage [www.python.org](http://www.python.org)
- [PyGTK] PyGTK (GTK+ for python), homepage [www.pygtk.org](http://www.pygtk.org)
- [Rei59] R. Reines and C. L. Cowan, *Phys. Rev.* 113 (1959) 273
- [ROOT] ROOT, homepage [root.cern.ch/](http://root.cern.ch/)
- [Sch97] N. Schmitz, *Neutrino Physik*, Teubner Verlag, 1997
- [SIMION] SIMION, homepage [simion.com](http://simion.com)
- [Sis04] M. Sisti et al., *Nucl. Instr. Meth. A* **20** (2004) 125 - 131
- [Ste07] M. Steidel, KATRIN internal document, 2006  
BSCW: Review of Detector Design SUMMER 07
- [Thu07] t: Thümmler, Dissertation  
Institut für Kernphysik, Westfälische Wilhelms-Universität Münster, 2007
- [Tow10] J. S. Townsend, *The Theory of ionization of gases by collision*  
published by Constable & Company LTD, 1910

- 
- [Val04] K. Valerius, Diploma thesis  
Helmholtz-Institut für Strahlen- und Kernphysik, Rheinische Friedrich-Wilhelms-Universität Bonn, 2004
- [Val09] K. Valerius, PhD thesis (in preparation)  
Institut für Kernphysik, Westfälische Wilhelms-Universität Münster, 2009
- [Voe08] S. Vöcking, Diploma thesis  
Institut für Kernphysik, Westfälische Wilhelms-Universität Münster, 2008
- [Wol08] I. Wolff, Diploma thesis  
Institut für Kernphysik, Westfälische Wilhelms-Universität Münster, 2008
- [Zub04] K. Zuber, Neutrino Physics  
Institute of Physics Publishing Bristol and Philadelphia, 2004



# Eigenständigkeitserklärung

Ich versichere, dass ich diese Arbeit selbständig verfasst, keine anderen als die angegebenen Quellen und Hilfsmittel benutzt und Zitate kenntlich gemacht habe.



# Danksagung

Ich möchte mich an dieser Stelle bei allen bedanken, die in vielerlei Weise zu dieser Diplomarbeit beigetragen haben.

Vor allen anderen muss ich meinen Eltern danken, von denen ich immer unterstützt wurde. Ich bin euch sehr dankbar.

Einen großen Dank richte ich an Prof. Weinheimer, der sich immer die Zeit für Gespräche und Hilfe nahm, auch wenn seine Zeit sehr knapp bemessen war. Herzlich bedanken möchte ich mich auch für die Möglichkeit, an so verschiedenen und interessanten Themen zu arbeiten und auch für die Chance, an so vielen Schulen, Konferenzen und Meetings teilzunehmen.

Prof. Wessels danke ich für die Übernahme der Zweitkorrektur dieser Arbeit.

Allen Bewohnern unseres Büros möchte ich für die tolle Atmosphäre danken. Karen, Kathrin, Irina, Sebastian, Alex and Sebastian, ihr habt mit der richtigen Mischung aus Spass und Ernst dafür gesorgt, dass ich mich immer wohlgeföhlt habe. Danke dafür.

Björn und der ganzen Reinraum-Crew danke ich für die unterhaltsame Zeit im Reinraum. Mit euch sind die vielen Stunden nie langweilig geworden.

Bei Karen möchte ich mich herzlich bedanken für die Einführung in das elektromagnetische Design, die immer freundliche und geduldige Hilfe und auch die gute Zusammenarbeit.

Ich möchte nicht versäumen Kathrin und Hans-Werner für ihre immer sehr freundliche und kompetente Unterstützung zu danken.

Dank richte ich auch an Markus und Henrik für ihre große Hilfe am Feldemissions-Aufbau.

Achim, Karen, Marcus, Sebastian und Volker danke ich sehr herzlich für das kompetente, gründliche und dennoch schnelle Korrekturlesen dieser Arbeit. Ohne euch wäre diese Arbeit nicht möglich gewesen.

Ich kann diese Danksagung nicht schließen ohne die Teilnehmer der täglichen, aber nicht all-täglichen Kaffeerrunde zu erwähnen. Svenja, Eva, Holländer, Junior und allen anderen möchte ich sagen: Sometimes it was strange, sometimes it was absurd, but it was always worth the time.

Mein größter Dank geht an meine Frau Hella, die mich durch alle Hochs und Tiefs begleitet hat. Sie hat mir Freiraum zum Arbeiten gelassen wenn ich ihn brauchte und mich zu Pausen gezwungen wenn ich sie nötig hatte. Danke das du da bist.

